Available online at www.sciencedirect.com

ScienceDirect

Advances in Space Research 72 (2023) 1304–1348

ADVANCES IN SPACE RESEARCH (a COSPAR publication)

www.elsevier.com/locate/asr

A reference architecture for orbiting solar reflectors to enhance terrestrial solar power plant output

Andrea Viale, Onur Çelik *, Temitayo Oderinwale, Litesh Sulbhewar, Colin R. McInnes

Space and Exploration Technology Group, James Watt School of Engineering, University of Glasgow, Glasgow G12 8QQ, Scotland, United Kingdom

Received 29 August 2022; received in revised form 25 April 2023; accepted 19 May 2023
Available online 26 May 2023

Abstract

Orbiting reflectors offer the possibility of illuminating large terrestrial solar power plants to enhance their output, particularly at dawn and dusk when their output is low but energy spot prices can be high. While the concept of orbiting solar reflectors has been considered in various forms in the past, there is now a timely overlap of rapidly growing global demand for clean energy services, falling launch costs through reusability and the emergence of in-orbit manufacturing technologies to enable the fabrication of large, ultra-lightweight space structures. This paper provides an end-to-end analysis of a possible minimum initial architecture to deliver such global clean energy services. The analysis will cover orbit selection, attitude control requirements, structural analysis and economical viability, followed by a discussion on regulatory issues, future improvements and further applications.

Keywords: Orbiting solar reflectors; Space-based solar energy; Solar energy; Space technology; Space mission analysis

1. Introduction

While wireless (and optical) power transmission has been considered for space-based solar power (Glaser, 1992; Laracy et al., 2007; Rawer, 1982; Venugopal et al., 2022; Chen et al., 2023), the key advantage of orbiting solar reflectors is that the space and ground segments are entirely decoupled. For wireless power transmission a large ground-based rectenna array is required to collect and convert microwave energy delivered from space-based solar power satellites to electrical energy delivered to the grid (Glaser, 1992). However, orbiting solar reflectors can illuminate conventional terrestrial solar power farms (SPFs) directly with sunlight. SPFs are expected to grow in both number and size in the coming years to service the rapidly growing global demand for clean energy (Haegel et al., 2017). Therefore, large terrestrial SPFs are likely to be built in any case, independent of the space sector, so significant capital will already have been invested on ground. There is then an opportunity to use light-weight orbiting solar reflectors to deliver additional energy to enhance their output, again particularly at dawn and dusk when output is low (Çelik et al., 2022). Compared to space-based solar power, this offers the possibility of a lower mass delivered to Earth orbit, with the ground segment infrastructure already installed and paid for. Relevant research on orbiting solar reflectors include the study by Ehricke (1979), who discussed the use of reflectors for a number of concepts with different applications, ranging from illumination of urban areas to delivery of solar energy at night. Then, a NASA study in the 1980s investigated the use of a 1 km deployable reflector in equatorial orbit with mass per unit area of $14 gm^{-2}$ and a pair of 40-meter diameter deployable

* Corresponding author.
E-mail addresses: andreaviale@protonmail.com (A. Viale), Onur.Celik@glasgow.ac.uk (O. Çelik), Temitayo.Oderinwale@glasgow.ac.uk (T. Oderinwale), Litesh.Sulbhewar@glasgow.ac.uk (L. Sulbhewar), Colin.McInnes@glasgow.ac.uk (C.R. McInnes).

https://doi.org/10.1016/j.asr.2023.05.037
0273-1177/

Nomenclature

Acronyms

AU	Astronomical Unit
ECCRF	Earth-centred co-rotating frame
ECIRF	Earth-centred inertial reference frame
CMG	Control moment gyro
ISS	International Space Station
LEO	Low Earth Orbit
RGT	Repeating ground track
SPF	Solar Power Farm
SSO	Sun synchronous orbit
SRP	Solar radiation pressure
THRF	Topocentric horizon reference frame
TRF	Target reference frame

Main symbols

a	Orbit semi-major axis [km]
A	Area [m^2]
c	Speed of the light [ms^{-1}]
C_N	Normal dynamic force coefficient
d	Slant range [m]
D	Orbit repetition frequency
$\mathcal{E}$	Energy [J]
e	Eccentricity
E	Young's modulus [GPa]
F	Force [N]
g_0	Acceleration due to gravity [ms^{-2}]
G	Shear modulus [GPa]
h	Orbit altitude [m]
H	Angular momentum [Nms]
J_2	Second degree zonal harmonic
$\mathbf{J}$	Inertia tensor [kg m^2]
i	Inclination [deg]
I	Moment of inertia [m^4]
I_0	Solar constant [W m^{-2}]
l	Side of hexagonal reflector [m]
L	Length of structural element [m]
m	Mass [kg]
M	Moment [Nm]
n	Mean motion [rad s^{-1}]
N	Number of orbits
P	Power [W]
$\mathbf{q}$	Quaternion
Q	Orbit repetition parameter
$\mathbf{r}$	Position vector [m]
R_E	Earth's equatorial radius [km]
S	Westward ground track shift [rad]
t	Time [s]
T	Orbit period [s]
$\mathbf{T}$	Torque [Nm]
$\hat{\mathbf{u}}_i$	Incident light unit vector
$\hat{\mathbf{u}}_r$	Reflected light unit vector
V	Velocity [ms^{-1}]
$\hat{\mathbf{x}}, \hat{\mathbf{y}}, \hat{\mathbf{z}}$	Unit vector along the x, y and z axis
α	Sun angle [rad]
β	Cone angle [rad]
γ	CMG skew angle [rad]
Δ	Deflection [m]
δ	CMG gimbal angle [rad]
ϵ	Elevation [rad]
θ	Argument of latitude [rad]
η	Reflectivity
Υ	Angle of attack [rad]
κ	Coefficient of thermal expansion [K^{-1}]
λ	Longitude [deg]
μ	Gravitational parameter [m^3 s^{-2}]
ν	Poisson's coefficient
ρ	Density [kg m^{-3}]
ς	Power density [W m^{-2}]
σ	Areal density [kg m^{-2}]
τ	Strength/ Stress [MPa]
ϕ	Latitude [deg]
χ	Atmospheric transmission efficiency
ψ	Angle between incoming and outgoing sunlight [rad]
Ω	Right ascension of the ascending node [deg]
$\boldsymbol{\omega}$	Angular velocity [rad s^{-1}]

Subscripts/Superscripts

$\square_{\text{atm}}$	Atmosphere
$\square_{cmg}$	Control moment gyro
$\square_g$	Ground target
$\square_{gg}$	Gravity gradient
$\square_{gt}$	From ground to target
$\square_E$	Earth
$\square_i$	Inertial
$\square_{im}$	Image of solar disk
$\square_o$	Orbit
$\square_{pass}$	Orbital pass
$\square_r$	Reflector
$\square_{reor}$	Reorientation
$\square_{\text{SPF}}$	Solar power farm
$\square_{\text{srp}}$	Solar radiation pressure
$\square_t$	Target
$\dot{\square}, \ddot{\square}$	First and second derivative with respect to time

control moment gyros for attitude control (Hedgepeth et al., 1981). More recently, Fraas (2019) studied a constellation of 18 reflectors in a 1000 km polar orbit. A technology demonstration roadmap for orbiting solar reflectors is proposed in Ref. (Viale et al., 2022). A recent paper also proposed a compound reflector system as an alternative

concept (Çelik and McInnes, 2022). A comprehensive literature review on orbiting solar reflector is available in Ref. (Çelik et al., 2022).

Nevertheless, there are inherent limitations associated with orbiting solar reflectors. First, a flat reflector will project an image of the solar disk onto the surface of the Earth. For a 1000 km orbit altitude the spot size has a diameter on the order of 10km, so large terrestrial SPFs are required in order to fully utilise the energy delivered. It should be noted, however, that the rectenna for space-based solar power can also be of the order of kilometres in diameter (Laracy et al., 2007). An arguably more serious limitation is the pass duration of the pass over a SPF when energy is delivered. This is typically on the order of 20 min, again for a 1000 km orbit altitude (Çelik et al., 2022). If a single reflector is only servicing a small number of terrestrial SPFs per day, the utilisation of the reflector will be low. This is in contrast to solar power satellites in geostationary orbit which will deliver energy continuously. Moreover, in addition to atmospheric losses there are geometric losses for orbiting solar reflectors, since the shape of the projected image of the solar disk is elongated at rise and set during a pass across of terrestrial SPF (Çelik and McInnes, 2022).

The niche opportunity for orbiting solar reflectors is to deliver useful energy services to enhance the operation of large terrestrial SPFs. Authors in Oderinwale and McInnes (2022) investigated and discussed using orbiting solar reflectors as an alternative to using energy storage for enhancing solar energy generation and usage. An analysis of the long-term economic feasibility of orbiting solar reflectors for utility-scale electricity generation is presented in Oderinwale and McInnes (2022). For reflectors in polar, or near polar orbit, energy services can be delivered globally to multiple customers. As noted above, terrestrial SPFs are growing in physical size and hence capacity. The largest solar polar plant currently under development is the Sun Cable venture in northern Australia which will deliver 17 GW [1] from a total area of 105 km^2. This will be considered as an exemplar power plant to consider later in the paper. Given the rapidly growing demand for clean energy we anticipate many more large SPFs to be installed globally in future (Laracy et al., 2007). As the number of SPFs grows, the potential utilisation of the orbiting solar reflectors increases, as does the revenue generated for the reflector operators. There are however constraints on the number of SPFs which can be serviced per orbit. After each pass of a SPF the reflector will need to slew and recover to the correct attitude required for the next pass.

The purpose of this paper is to present a single reference architecture for orbiting solar reflectors to enhance the output of terrestrial SPFs. A list of the current largest terrestrial SPFs will be used as the basis for the reference architecture. The key contribution of the paper is to provide a detailed analysis of the orbiting solar reflector concept spanning and integrating orbital dynamics, attitude control, structures and economic analysis. Indeed an economic analysis will be presented to define the breakeven conditions for such an architecture in terms of energy prices, launch costs and discount rate. In doing so, the paper provides a platform on which to build future analysis of the concept and to pursue the technologies required to develop and deploy such space-based energy infrastructure. The limitations of the paper include neglecting orbit perturbations other than Earth oblateness, assuming rigid body attitude dynamics, neglecting wrinkling of the reflective membrane, uncertain reflector procurement costs and assuming constant energy conversion efficiency. However, these issues can be addressed in future analyses. In conclusion, the reference architecture will illustrate the benefits and limitations of orbiting solar reflectors, the technological challenges presented and the economic trade-offs associated with their use. Based on these findings conclusions and recommendations on the future development of orbiting solar reflectors will then be made.

2. Reference architecture definition

The reference architecture is selected to illustrate the benefits and limitations of orbiting solar reflectors. Where possible, the architecture will be representative of current or near term developments in both the energy and space sectors. Firstly, in order to ground the reference architecture in the current terrestrial energy economy, the location of the top 12 SPFs (real or under development) are used as the basis for orbit selection. These are listed in Table 1. The Sun Cable SPF under development in northern Australia will be used to anchor the orbit for the first overhead pass. While current operational SPFs are in general smaller than the projected spot size delivered by the reflectors, they will be assumed to be scaled to match the spot size for the purpose of illustration, defined later to be 10 km.

A single dawn-dusk Sun-synchronous repeat ground track orbit will be defined. This will ensure that the reflectors are always illuminated and that energy services are delivered locally when demand, and hence spot prices, can be high. As noted above, the phasing of the orbit is selected to ensure an overhead pass at the Sun Cable SPF. The geometry of the passes over other SPFs are therefore dictated by their geographical location. However, the existence of a constellation of reflectors could influence the selection of the location of future large SPFs to be near the ground track of the reflectors.

The reflectors are assumed to be fabricated from triangular elements via in-orbit manufacturing such that the final assembly has a hexagonal shape. The use of triangular modules has the advantage that a structure of any arbitrary size can be constructed. Moreover, in the case of membrane tearing (e.g., due to orbital debris), only a single triangular module would be damaged, rather than the entire structure. Developments of the SpaceX Starship re-usable

[1] www.suncable.energy.

Table 1
Some of the largest solar parks with their capacity and land size.

#	Solar park [Country]	Capacity [GW]	Land size [km^2]	Coordinates [ϕ, λ] [deg, deg]
1	Sun Cable [AU]	17.000	105	−17.29, 133.5
2	Bhadla [IN]	2.245	57	27.5, 71.9
3	Pavagada [IN]	2.050	53	14.7, 77.2
4	Benban [EG]	1.650	37	24.7, 32.8
5	Tengger Desert [CN]	1.547	43	37.6, 105.0
6	Noor Abu Dhabi (Sweihan) [AE]	1.177	8	24.6, 55.4
7	Datong [CN]	1.070	N/A	40.7, 113.1
8	Kurnool Ultra Mega [IN]	1.000	24	16.15, 78.4
9	Longyangxia Dam [CN]	0.850	23	36.9, 100.5
10	Villanueva [MX]	0.828	27.5	26.3, −102.9
11	Solar Star I and II [US]	0.747	13	35.8, −118.2
12	Topaz [US]	0.550	19	34.4, −115.2

launch vehicle will be considered for the transportation of materials and components to space. The trade-off of launch costs, reflector costs and energy prices will be investigated to assess how many SPFs need to be serviced each day to achieve economic breakeven.

Based on prior trade-offs studies of actuators (Viale and McInnes, 2023), control moment gyros (CMG) are selected for attitude control. The dimension of the CMG rotors is selected based on the Starship fairing dimension and a material with a large strength to density ratio is chosen, to maximize the rotor nominal angular momentum. The choice of the CMG will then drive the sizing of the reflector to a hexagon with a side of 250 m. Multiple mirrors in formations will be considered to ensure that significant energy is delivered during each pass over a SPF, such that the total reflective area is equivalent (at least) to that of a 1 km diameter circular reflector. A summary of the key elements of this reference architecture is provided in Table 2 and an in-orbit rendering of the concept is represented in Fig. 1.

The remainder of the paper is organised as follows. First, the selection of the orbit and the SPFs to be tracked is discussed in Section 3. Orbit control via solar radiation pressure will be also addressed. Then, based on the selected elements for the orbit, the requirements for the reflector actuators are presented in Section 4, upon definition of four operational phases. The size of the reflector is then determined and a closed-loop simulation is performed for a 24 h cycle. A discussion on the reflector structure and economic aspects will then follow in Sections 5 and 6, respectively. Lastly, additional details about the location of new SPFs, upper limits on the energy delivered, illumination levels on ground, other applications and alternative actuators are provided in Section 7.

3. Reflector orbit selection

The reflectors in this study are assumed to be in a train-type orbital motion, following each other in a closely spaced configuration, as shown in Fig. 1. This reference orbit is designed in this section. It is noted that the effective reflector area created by five 250-m side length hexagonal reflectors is equal to the area of a single disk with a diameter of 1.016 km.

The reflector orbit should be selected such that multiple requirements can be satisfied. One of those requirements is the Sun-synchronous condition. The Sun-synchronous condition allows the ascending node to be fixed at a given local time with respect to the Sun. This condition means that the orbit plane is precessed at an angular rate equal to that of the Earth's angular velocity in a circular orbit around the Sun. The Sun-synchronous condition is achieved by using the perturbation arising from the Earth's oblateness, which constrains the inclination, i, of the orbit for a given semi-major axis, a, and eccentricity, e. The family of Sun-synchronous orbits (SSO) are also practically eclipse-free at appropriately chosen values of right ascension of the ascending node. They can then be placed close to the day/night terminator line to deliver solar energy at dawn or dusk hours. This delivery is ideally expected to be every day, approximately at the same local time. That means the selected orbit also needs to satisfy the constraint of a repeating ground track (RGT) orbit. The RGT condition is related to the orbit period, which constrains the altitude of the reference orbit. Moreover, if a particular SPF and a particular time of the day is selected for the pass, then the orbit will be further constrained in its right ascension of the ascending node and argument of perigee. Finally, and importantly, the quantity of solar energy delivered needs to be maximised. Orbiting solar reflectors project the image of the solar disk to the ground. As the solar flux, the effective area of the reflectors and the area of the solar farms are fixed, the density of solar power on ground is determined by the area of the projected image of the solar disk. This means that high-altitude orbits will deliver lower solar power density whereas low-altitude orbits mean high solar power density. The former will also mean longer pass durations while the latter will also experience increased perturbations due to atmospheric drag. Therefore, an optimal altitude will be selected to maximise the energy delivery.

The reflector orbit is selected from these competing requirements and the selection process is discussed in detail in the following subsections. First, however, the reference

Table 2
Overview of the proposed reference architecture.

Orbit	Altitude	884.59 km
	Inclination	98.97°
	Orbit type	circular Sun-synchronous with repeating ground track
	Passes/ cycle	14 orbits per 24-h cycle
	Serviced SPFs	8
	Number of reflectors	5
Attitude control	Actuator	4 × Control moment gyros in pyramid configuration, skew angle 53.13°
	Total actuator mass	4 × 245 kg (CMGs) + 80 kg (desaturation)
	Rotor angular momentum	227612 N m s
	Peak torque (total)	1704 Nm
	Rotor radius	6.5 m
	Rotor angular velocity	351.5 rad s^{-1}
	Rotor material	Carbon fiber
	Desaturation	Variable reflectivity panels (in-plane control) + rotating vanes (out-of-plane control)
	Type	Assembly of triangular reflectors in a hexagonal shape using truss support
	Number of triangular modules	150
	Size of triangular modules	50 m
Structure	Total mass (with actuator)	5 × 3051.5 kg
	Equivalent diameter of total reflective area (5 reflectors)	1016.7 m
	Size (hexagon side)	250 m
	Areal density	18.8 gm^{-2}
	Materials	Graphite-epoxy for the support structure and aluminized Kapton for the reflector film
Economics	Operational Life-time	20 years
	Procurement cost of reflector	375 $/kg
	Annual Maintenance cost of reflector	5.6 $/kg
	Target cost of electricity	70 $/MWh

frames and dynamical model will be introduced in the next subsections.

3.1. Reference frames

In order to describe the orbital position and attitude of the reflector, the following reference frames are defined.

- Earth-centred inertial frame (ECIRF). The x-axis ($\hat{\mathbf{x}}_i$) is directed towards the γ point (vernal equinox), the z-axis ($\hat{\mathbf{z}}_i$) is parallel to the Earth's spin axis and the y-axis ($\hat{\mathbf{y}}_i$) completes the triad.
- Earth-centred co-rotating frame (ECCRF). This frame is the same as the ECIRF initially but rotates about $\hat{\mathbf{z}}_i$ at a rate equal to the Earth's rotation rate.
- Topocentric horizon reference frame (THRF). The z-axis ($\hat{\mathbf{z}}_{th}$) is parallel to the Earth's radius and normal to the horizontal plane defined as the local horizon, the x-axis points east and is defined as $\hat{\mathbf{x}}_{th} = \frac{\hat{\mathbf{z}}_{th} \times \hat{\mathbf{z}}_i}{|\hat{\mathbf{z}}_{th} \times \hat{\mathbf{z}}_i|}$, the y-axis completes the triad, pointing north, and denoted as $\hat{\mathbf{y}}_{th}$.
- Reflector reference frame (RRF). This body-fixed frame is centred at the reflector centre-of-mass and has the axes aligned with the reflector principal axes of inertia, with the x ($\hat{\mathbf{x}}_r$) and y ($\hat{\mathbf{y}}_r$) axes being the in-plane axes and the z-axis ($\hat{\mathbf{z}}_r$) being the out-of-plane axis.
- Target reference frame (TRF). This frame defines the desired orientation of the RRF. The orientation of the TRF will be described in detail in Section 4.2. The unit vectors of the TRF are indicated with $\hat{\mathbf{x}}_t, \hat{\mathbf{y}}_t$ and $\hat{\mathbf{z}}_t$.

3.2. Dynamical model

SSOs can be achieved naturally by exploiting the Earth's oblateness perturbation to precess the reflector's orbit plane. The orbital motion of the reflectors is therefore modelled by the perturbed two-body problem dynamical model. The equations of motion can be expressed such that:

$$\begin{aligned} \ddot{x} &= -\tfrac{\mu}{r^3}x + p_x \\ \ddot{y} &= -\tfrac{\mu}{r^3}y + p_y \\ \ddot{z} &= -\tfrac{\mu}{r^3}z + p_z \end{aligned} \tag{1}$$

where x, y and z are cartesian position components in ECIRF, r is the distance from the centre of the Earth, $r = \sqrt{x^2 + y^2 + z^2}$, μ denotes the Earth's gravitational parameter equal to 398600 $km^3 s^{-2}$ and p_x, p_y and p_z are perturbing accelerations. In this paper, only the perturbing acceleration due to the Earth's oblateness up to second degree, i.e., J_2 is considered, whose value is equal to

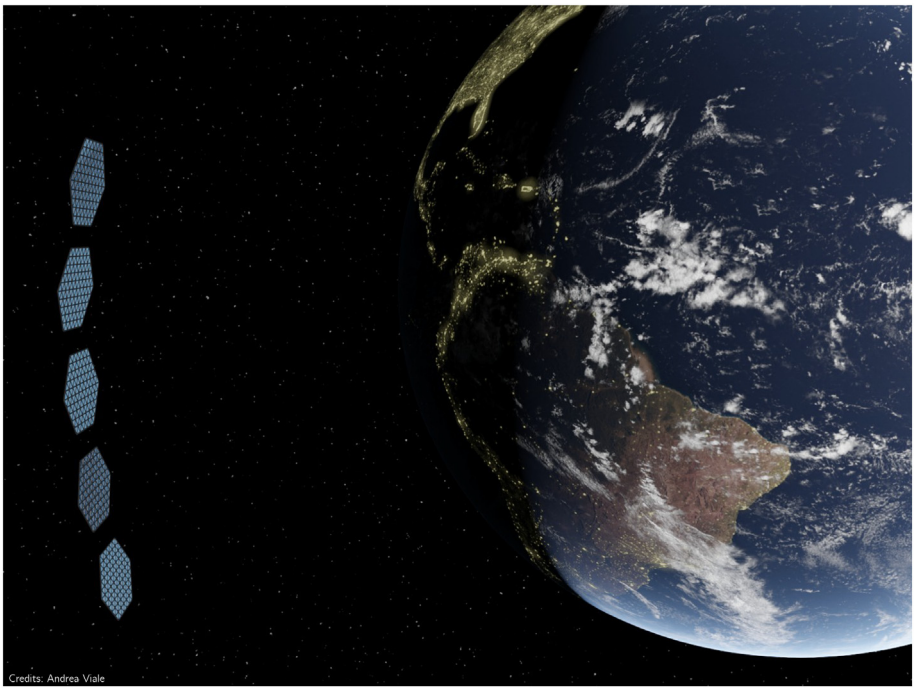

Fig. 1. Render of a train of reflectors, in-orbit view (not to scale). Credits: Andrea Viale (University of Glasgow), NASA (for Earth texture).

1.08263×10^{-3} (Schaub and Junkins, 2009). This perturbing acceleration in cartesian coordinates in ECIRF can be expressed as Schaub and Junkins (2009):

$$\mathbf{p} = \begin{bmatrix} p_x \\ p_y \\ p_z \end{bmatrix} = -\frac{3}{2} J_2 \frac{\mu}{r^2} \left(\frac{R_E}{r} \right)^2 \begin{bmatrix} \left(1 - 5\left(\frac{z}{r}\right)^2\right)\left(\frac{x}{r}\right) \\ \left(1 - 5\left(\frac{z}{r}\right)^2\right)\left(\frac{y}{r}\right) \\ \left(3 - 5\left(\frac{z}{r}\right)^2\right)\left(\frac{z}{r}\right) \end{bmatrix} \tag{2}$$

where R_E is the equatorial radius of the Earth, 6378.2 km. Note that $p_x = p_y = p_z = 0$ means non-perturbed orbital motion around a spherical Earth, which will also be used in the selection of the Keplerian orbital elements in the next subsections.

3.3. Selection of semi-major axis, eccentricity, inclination and the initial argument of latitude

Semi-major axis, eccentricity and inclination are considered together as they are coupled to enable the Sun-synchronous condition. As will be discussed later, perturbations due to the Earth's oblateness introduces a latitudinal component to the gravitational acceleration, which affects the RGT considerations through the argument of perigee, as well.

3.3.1. The Sun-synchronous condition

The Sun-synchronous condition for orbit around the Earth dictates that the orbital plane would precess at the same angular rate as the Earth moves around the Sun in a circular orbit. This angular rate can be calculated as 0.9856 deg/day or 1.992×10^{-7} rad s^{-1}. This precession rate can be achieved by using the Earth's oblateness at appropriately inclined orbits for a given semi-major axis and eccentricity. The oblateness causes the gravity vector to deviate from the Earth's centre and introduces a latitude dependence, called the zonal variation. As noted, for an appropriate set of a, e and i, the Earth's oblateness would allow the orbital plane to precess through the change of right ascension of the ascending node at the required rate, as given below (Chobotov, 2002):

$$\dot{\Omega} = -\left[\frac{3}{2} \frac{\sqrt{\mu} J_2 R_E^2}{a^{7/2}(1-e^2)^2} \right] \cos i \tag{3}$$

The ascending node is needed to progress eastward in accordance with the Earth's orbital motion around the Sun, therefore 90 deg $< i \leqslant$ 180 deg. For perfectly polar orbits (i.e., $i = 90$ deg), the ascending node stays stationary, hence there is no Sun-synchronicity. As for the eccentricity, circular orbits are considered in this paper, i.e., $e = 0$. Eq. (3) can then be rearranged to find the required inclination after substituting the constants in Eq. 3:

$$i = \arccos\left(-4.7736 \times 10^{-15} a^{7/2}\right) \tag{4}$$

where a is in the units of kilometers. For a given value of semi-major axis, the inclination that enables the Sun-synchronous condition can then be found. As the orbit is circular, selection of the semi-major axis length is equivalent of finding a suitable orbit altitude that satisfies the requirements for the reflector orbit. In addition to the Sun-synchronous condition, the orbit also needs to repeat its ground track daily to deliver the maximum possible

solar energy. Therefore, the RGT condition is investigated first.

3.3.2. The Repeating Groundtrack (RGT) altitudes for the spherical Earth

An orbit is stated to be a RGT orbit if it completes an integer number of orbits in a given duration (Chobotov, 2002). When a perfectly spherical Earth and a stationary target are considered, this can be expressed as Chobotov (2002):

$$Q = N/D \tag{5}$$

where Q is the repetition parameter, D is the repetition frequency in days and N is the number of orbits before coming back to the starting point. Daily repetition means $D = 1$. Moreover, Q can also be written in terms of ground track shift at the equator as:

$$Q = 2\pi/S \tag{6}$$

where S is the westward ground track shift at the equator due to the eastward rotation of the Earth and is given as:

$$S = T\omega_E \tag{7}$$

where T is the orbit period and is given as:

$$T = 2\pi\sqrt{\frac{(R_E + h)^3}{\mu}} \tag{8}$$

Substituting this expression in Eq. 5 and rearranging to find the orbit altitude yields

$$h = \left(\frac{\mu}{\omega_E N}\right)^{1/3} - R_E \tag{9}$$

In Eq. (9), h denotes altitude, i.e., $h = a - R_E$. From Eq. (9), it can be found that, for $N = 1$, the orbit altitude is the geostationary orbit altitude, $h = 35786$ km. Solving Eq. 9 for other integer values where $N > 1$ would result in lower altitude orbits.

At this stage, pass durations can also be calculated for given RGT orbit altitudes, again for stationary targets. The cone angle β is defined between two vectors extended from the centre of the Earth to the SPF and to the point where the plane of the SPF intersects the orbit, as shown in Fig. 2, and calculated as

$$\beta = \arccos\frac{R_E}{R_E + h} \tag{10}$$

The orbital pass would then be the duration for the reflector to cover and arc of 2β from rising to setting at the horizon as follows (Çelik and McInnes, 2022):

$$T_{\text{pass}} = \frac{2\beta T}{2\pi} = \frac{T}{\pi}\arccos\frac{R_E}{R_E + h} \tag{11}$$

A selection of RGT orbit altitudes is presented in Table 3 alongside their pass duration. There are a number of LEO altitudes that can be used for the reflectors. The lowest two of those complete 15 and 16 revolutions daily and are at altitudes where the Earth's atmospheric drag is more pronounced. It is then more reasonable to consider higher altitude orbits to avoid atmospheric effects. However, the highest altitudes mean lower solar power density on ground even though they also provide longer pass durations. Therefore, reflector altitudes are sought from those relatively less affected by atmospheric effects with maximised solar energy delivery. It is therefore of interest to determine what the optimal altitude for the maximum energy delivery is which will be discussed next.

3.3.3. The quantity of solar energy delivered

With the downselected RGT orbit altitudes at hand, one can now look at the properties of reflected solar energy delivery for a range of LEO altitudes. The power received by the SPF can be expressed as follows (Çelik and McInnes, 2022):

$$P_{\text{SPF}} = \eta\chi(t)\varsigma A_{\text{SPF}} = \eta\chi(t) I_0 \frac{A_r}{A_{im}(t)}\cos\left(\frac{\psi}{2}\right) A_{\text{SPF}} \tag{12}$$

where ς denotes the power density on ground, I_0 is the solar constant defined as the mean solar energy per unit area, assumed to decrease by an inverse-square law with the distance from the Sun and is equal to 1.37 GWkm^{-2} at 1 Astronomical Unit (AU). Furthermore, A_r, A_{im} and A_{SPF} denote the areas of the reflector, image of the solar disk and SPF, respectively. Then, ψ is the angle of incidence between the incoming and outgoing sunlight, χ is the atmospheric transmission efficiency (Hottel, 1976; Çelik and McInnes, 2022) and η is the reflectivity, assumed 0.92 in this paper following earlier studies (Canady and Allen, 1982). Eq. 12 describes the concept of orbiting solar reflectors, in which incoming solar energy is intercepted by the fixed reflector area A_r projected over an area of solar image A_{im} and collected by a fixed solar power farm area A_{SPF}. Both A_r and A_{SPF} are constant, therefore the delivered energy is primarily a function of time-dependent A_{im}. The geometry of A_{im} during an orbital pass, which is primarily a function of the slant range, d, and the elevation angle, ϵ, from the solar power farm and the subtense angle α (i.e., equal to 0.0093 rad or 0.532 deg at 1 AU from the Sun) is discussed in detail by Çelik and McInnes (2022), and omitted here for brevity. It is necessary to find an orbit altitude that optimises the solar energy delivered to the SPFs assumed here. The energy delivered to a SPF can be found by integrating the solar power delivered P_{SPF} over the pass duration as:

$$\mathcal{E} = \int_0^{T_{\text{pass}}} P_{\text{SPF}}\,\mathrm{d}t \tag{13}$$

where $\mathcal{E}$ is the quantity of solar energy delivered to the SPFs. It is assumed that all energy received is available for conversion to electrical energy throughout the duration of the pass with no cut-off at low illumination levels. The details of this integration process are again provided in Ref. (Çelik and McInnes, 2022). Çelik and McInnes (2022) consider a circular polar orbit and an overhead pass

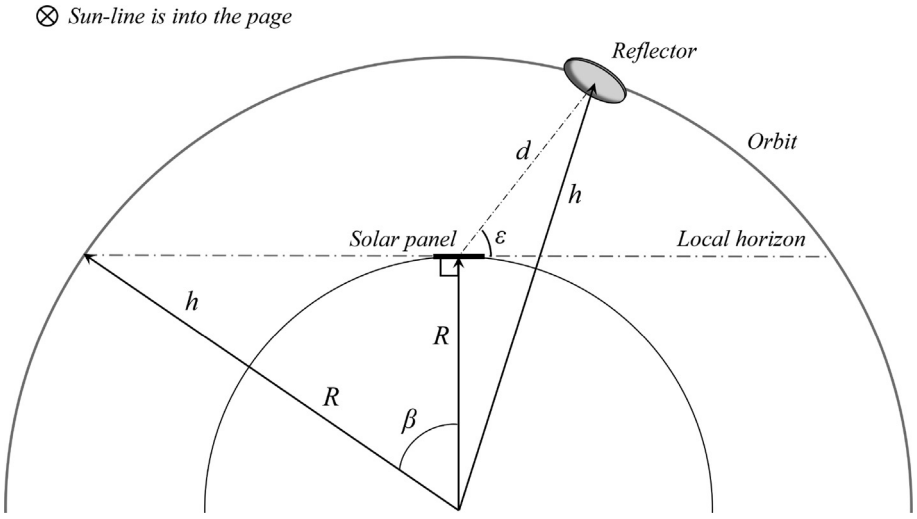

Fig. 2. Simplified orbital pass geometry to calculate the pass duration, T_{pass} (adapted from Çelik and McInnes, 2022).

Table 3
1-day Repeating Groundtrack orbit altitudes.

Number of orbits N	Altitude [km]	Orbit period [min]	Pass duration [min]
9	3384.62	160.00	43.74
10	2722.41	144.00	36.40
11	2162.14	130.91	30.31
12	1680.84	120.00	25.12
13	1262.07	110.77	20.55
14	893.77	102.86	16.40
15	566.87	96.00	12.43
16	274.40	90.00	8.26

of an ideal reflector over a stationary ground target, but also include atmospheric losses, solar panel tilt and time-dependent areal relationships between the solar image and the assumed circular SPF (Çelik and McInnes, 2022), which allows for an assessment of how efficiently the image of the solar disk, A_{im}, is used by a SPF in terms of the solar energy delivered. This paper considers inclined orbits, but the orbit is selected such that it is "anchored" to the Sun Cable solar farm as noted in Section 2, i.e., the overhead pass assumption remains valid. Therefore, with this assumption and a relatively low altitude orbit, the stationary target assumption in Ref. (Çelik and McInnes, 2022) is also appropriate. The solar energy delivered is then calculated for a range of LEO altitudes between 200 km to 3500 km (in accordance with the RGT altitudes in Table 3) to obtain an understanding of the optimal altitude for the maximum delivery of solar energy. The results are presented in Fig. 3. As shown in Fig. 3, for a given solar farm size, there is an optimum altitude where the quantity of energy is maximum. In this study, the solar farm diameter is assumed to be 10 km, as noted in Section 2 and as a result the optimum altitude is found to be approximately at 913 km. The quantity of energy delivered at this altitude is 33.9 MWh per orbital pass. It appears from Table 3 that the RGT orbit altitude of 893.77 km is very close to this optimum point. The energy delivered at this altitude is approximately 33.8 MWh from Fig. 3, which is almost optimal and satisfies both the daily-visit RGT as well as nearly maximising the solar energy delivered. An orbit altitude of 893.77 km is therefore selected at this stage as the reflector altitude without considering the Earth's oblateness effects. However, as noted earlier, the Earth's oblateness introduces latitudinal dependency to the direction of the gravity vector, therefore this altitude will need to be further refined, and the initial argument of latitude for the orbit will be selected. These aspects will be discussed next.

3.3.4. The initial argument of latitude and the modified RGT altitude

The orbit is "anchored" to the Sun Cable SPF in the northern Australia, such that the reflectors make the first orbit pass over this target. This is ensured by choosing an initial orbital position at which the orbit propagation begins. As the orbit is circular, neither the argument of perigee nor true anomaly are formally defined as orbital elements, and instead the initial argument of latitude (θ_o) can be used. By definition, θ_o is simply the angle between the right ascension of the ascending node (defined from the equator) and the reflector position.

Due to the inclusion of Earth's oblateness in the model and the dependency of the solar image geometry on the

orbital elements, this requires an additional analysis, which also changes the RGT orbit altitude, as will be shown. The argument of latitude is selected based on the latitude at which Sun Cable is located. Recall from Table 1 that the Sun Cable SPF is located at $[\phi, \lambda] = [-17.29, 133.5]$ deg. In order to choose θ_o, first, the orbit radius vector for a RGT altitude of 893.77 km is placed directly above this location. As an overhead orbital pass is required, i.e., the maximum elevation from the Sun Cable location must be close to 90 deg, the orbital pass must start at a latitude that is equal to the cone angle β before the latitude of Sun Cable and shifted westwardly in longitude to match the eastward rotation of the Earth and the orbit inclination. The value of β is equal to 28.61 deg for 893.77 km altitude. Initially, θ_o is therefore set to $\theta_o = -17.29 - 28.61 = -45.90$ deg and the orbit is propagated in the non-perturbed equations of motion in Eq. 1. This convention means that $\theta_o = 0$ deg at the equator. The right ascension of the ascending node is arbitrarily set to 90 deg (whose selection will be discussed more in detail in the next section) in this simulation. Then, the geometry of the pass is investigated by means of the maximum elevation angle at Sun Cable. The value is changed empirically until θ_o is found that allows an near overhead pass ($\max(\epsilon) \approx 90$ deg) over the Sun Cable SPF is found. The final value of θ_o is found to be -57.33 deg. At this value, the reflector comes into view a few seconds after the propagation starts and stays in view for approximately 971 s or 16.2 min. Recall from Table 3 that for the stationary Earth case, the calculated pass duration is approximately 16.4 min.

As discussed earlier, the inclusion of the J_2 effect will alter the orbit period. The latitudinal effect of the Earth's oblateness then needs to be taken into account to find a RGT orbit altitude. In this paper, a bisection algorithm is therefore developed to find a 1-day RGT orbit altitude that is suitable for the selected θ_o as a result of the Sun Cable farm location. In this algorithm, first, lower and upper boundaries of altitudes, h^- and h^+ are selected within $\pm 5\%$ of the non-perturbed RGT altitude, 893.77 km. At each iteration, the orbit has an altitude such that

$$h_j = \frac{h^- + h^+}{2} \tag{14}$$

where the subscript j denotes the iteration number. The orbit inclination was computed from Eq. 4 and the orbit was propagated in the perturbed equations of motion for 1 sidereal day (86164 s). At the end of each propagation, the orbit generated was transformed into an Earth-centered co-rotating reference frame (ECCRF) and the latitude of the end point of the orbit is calculated. If the orbit latitude φ is smaller than the Sun Cable latitude φ_0, then $h^- = h_j$ whereas if $\varphi > \varphi_0$, then $h^+ = h_j$. This procedure is continued until $\Delta\varphi = |\varphi - \varphi_0|$ is smaller than some selected tolerance value, which is 10^{-12} in this study. Moreover, at each step, it was also checked whether the longitude difference, $\Delta\lambda$, between the end point of the orbit and the Sun Cable longitude is equal to the orbit precession rate required for the Sun-synchronous condition, i.e., 0.9856 deg, again within the tolerance. This procedure was applied, and the 1-day RGT orbit altitude was found to be 884.59 km. From Eq. 4, the inclination for this orbit is calculated $i = 98.97$ deg.

Thus far, the semi-major axis, eccentricity, inclination and the argument of latitude of the orbit are determined. The remaining constant Keplerian orbital element, right ascension of the ascending node, will be discussed next.

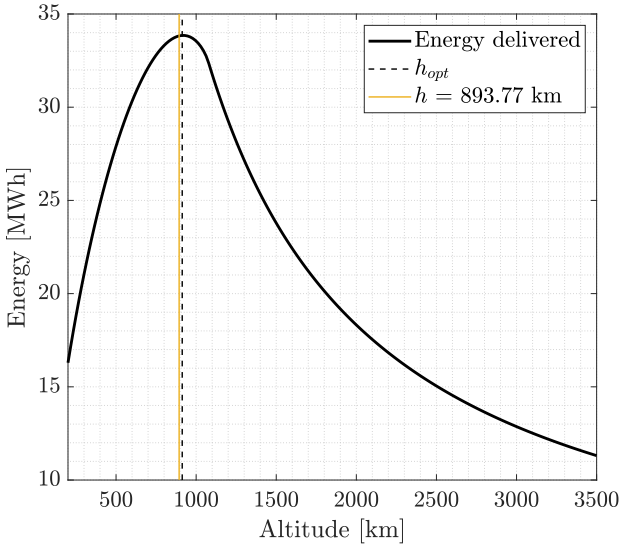

Fig. 3. Solar energy delivered to a 10-km across SPF from different orbits. Effective reflector diameter is 1.016 km, equivalent to five hexagonal reflectors with a side length of 250 m. The optimal altitude for energy delivery is denoted with the vertical dashed line, whereas the closest repeating ground track altitude is denoted with vertical yellow line.

3.4. Selection of right ascension of the ascending node

Right ascension of the ascending node, Ω, or the longitude of the orbit, is measured from the x axis of the ECIRF. As the Sun-synchronous condition states, Ω changes with the Earth's oblateness, at the angular rate which the Earth moves in its circular orbit around the Sun, i.e., 0.9856 deg/day. The selection of Ω for the reflectors will be carried out with two different criteria: (1) the orbits experience no eclipses in a day and (2) the maximum quantity of solar energy delivered is ensured. In general, SSO do experience eclipses throughout the year, albeit for a short duration, due to the inclination of Earth's rotation axis and its orbit around the Sun, but those are primarily around the polar regions. There is a small subset of orbit altitudes between 1399 km and 3301 km that do not experience eclipses throughout the year (Potter and Davis, 2009), but those are higher than the altitudes considered here. Here, the short duration of eclipses experienced in the yearly motion will be ignored, and daily motion will be considered. Fig. 4 then illustrates the geometric relationship to calculate the range of Ω that allows eclipse-free orbits. According to the illustration, in order to experience

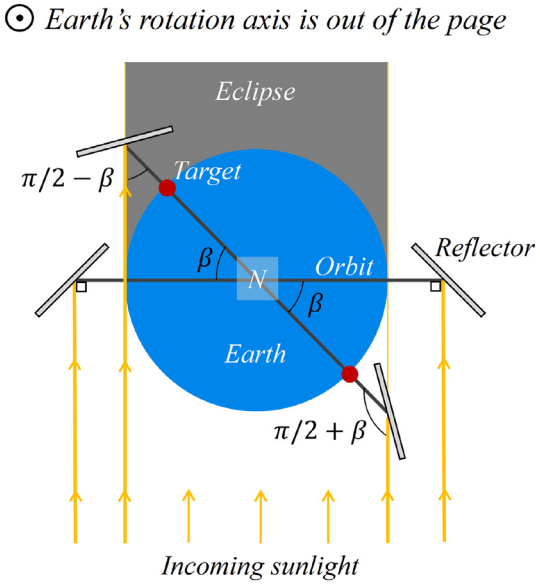

Fig. 4. Illustration of geometric relationships to calculate right ascension of the ascending node that allows eclipse-free orbits.

no eclipses, Ω must be in the range $[\pi/2-\beta, \pi/2+\beta]$. Here, β is the cone angle discussed earlier, and it is equal to 28.6 deg for the modified RGT altitude. Then, Ω must be between 61.4 deg and 118.6 deg. If the orbit with $\Omega =$ 90 deg orbit is placed such that the local time at the SPF is 6 pm, then these two longitudes correspond approximately to the local times between 4 pm and 8 pm. This gives a 4-h window around dawn/dusk where the orbit can be placed according to these considerations. It is important to note that, regardless of the value of Ω, the groundtrack will be fixed due to the fixed relative positions of the SPFs. The choice of Ω would only change the local time of visits at each target SPF.

However, there is another potential implication of Ω. If perfectly polar orbits are considered ($i = 90$ deg), then Ω would directly relate to the angle of incidence, ψ. For example, for a polar orbit placed at $\Omega = 90$ deg, the orbit would "ride" the terminator line, with $\psi = 90$ deg. If the orbit is placed on the night side, such that 90 deg $< \Omega < \Omega_{\max}$, then $\psi < 90$ deg. Considering the cosine term in Eq. (12), the energy delivered would be higher per orbital pass on the night side, vice versa on the day side of the Earth. But if there is a single SPF to be serviced, the hours after dusk or before dawn are more advantageous. However, when the orbit is inclined, the interpretation of the relationship between Ω and ψ is not as straightforward in terms of energy delivery. The value of ψ will be variable due to the orbit inclination; however, its impact on the total energy delivered cannot be estimated qualitatively, as it was done for polar orbits.

For that reason, the total energy delivered to potentially suitable SPFs during a day is computed. The suitability criterion is that the maximum elevation at a SPF is greater than 80 deg. First, the perturbed equations of motion are propagated with a time step of 1 s with the cartesian initial conditions transformed from the initial orbital elements a, e, i and θ_o with a range of Ω between 62 deg and 118 deg. The trajectory generated was projected onto the topocentric horizon reference frame (THRF) of each SPF. For the passes where a maximum elevation greater than 80 deg is achieved, Eq. 12 was applied to calculate the power delivered at each time step. The illuminated SPF area and the atmospheric losses are considered in the calculation of the power delivered. Then, the power calculated is summed over the duration of the orbital pass to find the total energy delivered. The result of this analysis is presented in Fig. 5. Fig. 5 shows an energy profile that maximises at approximately $\Omega = 88$ deg. The maximum quantity of reflected solar energy delivered in a day is 136.9 MWh. But it is important to note that the difference between the lower and upper boundary of Ω is very small. The quantity of energy delivered only varies by approximately 4 MWh between the lowest and highest values. Therefore, the orbit plane may be tilted to pass over the SPFs earlier or later in the day, if so desired economically. It was noted earlier that for perfectly polar orbits, shifting the orbit plane towards the night or day side means higher or lower energy delivery due to the constant angle of incidence (or reflector pitch angle). The small difference in energy delivery across the different Ω values in Fig. 5 is due to the variation of the angle of incidence throughout the orbit.

It appears that, from the perspective of energy delivery, Ω can be selected as 88 deg for the Sun-synchronous reflector orbit. In the next section, the properties of the selected orbit will be investigated.

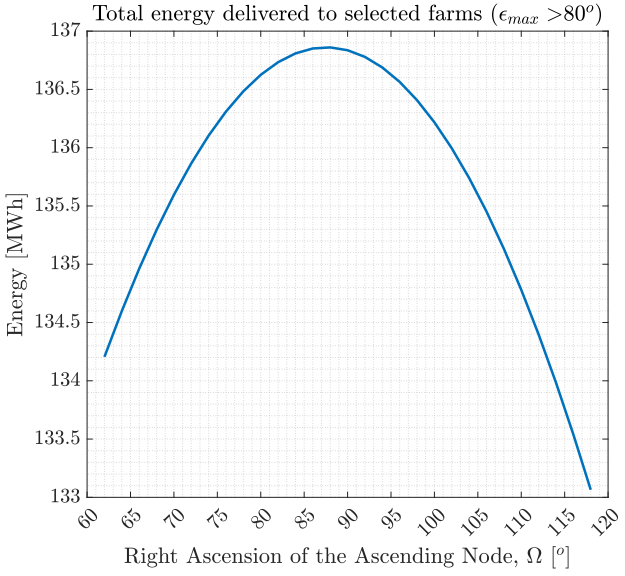

Fig. 5. The total energy delivered to selected SPF with maximum elevation greater than 80 deg at different right ascension of the ascending node values.

3.5. Selected orbit and its properties

In the previous section, the selection of the orbital elements was outlined. Recall once again that the argument of perigee and true anomaly are not formally defined for circular orbits. Instead, the initial argument of latitude, θ_o, is used. Then, the orbital elements of the selected SSO for the reflectors can be summarised below:

$$[a, e, i, \Omega, \theta_o] = [7262.79\ \text{km}, 0, 98.97\ \text{deg}, 88\ \text{deg}, -57.33\ \text{deg}]$$

The properties of the orbit from the perspective of orbiting solar reflectors can now be investigated. The orbital elements above are first converted into position and velocity vectors in cartesian coordinates, and these initial conditions are propagated numerically for 1 sidereal day by using Eqs. 1. Fig. 6 shows the orbit in the ECIRF. The groundtrack of this orbit can also be seen in Fig. 7. The groundtrack in Fig. 7 shows the passes over different SPFs qualitatively with their approximate time points in a day. The time shown in colour is not given as a specific hour of the day, but hours since the beginning of the orbit propagation. From the figure, it can be seen that there are 4 near-overhead passes in a day, but one of the SPF is visited twice in a day, approximately 12 h apart. Indeed, it is interesting to note that there are locations where two passes in a day can be achieved. These locations are an occurrence determined by the orbit altitude and inclination. For the altitude (and hence the inclination) considered for this paper, there are three SPF that are at approximately the same latitude as this intersection point in the ground track. If the requirement on visiting the Sun Cable solar farm can be relaxed, shifting the orbit plane slightly may allow more

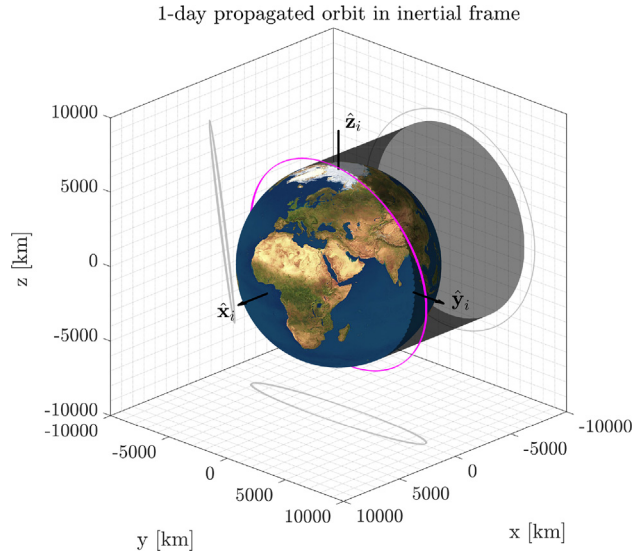

Fig. 6. 1-day propagated orbit in inertial reference frame. The projections of the orbit in the inertial x-y, x-z and y-z planes are also provided. The dark cylinder represents the eclipsed region or the nightside. The projection of the orbit in the y-z plane suggests that the Sun is visible throughout the day. The simulation is performed at the vernal equinox day, i.e., $\hat{\mathbf{x}}_i$ points towards the γ point.

passes over different SPF, but the exploration of these scenarios is left for future studies. A more quantitative analysis on the orbital passes can be seen in Fig. 8. Four overhead passes with a maximum elevation greater than 80 deg can be seen in Fig. 8. It is shown in Ref. (Çelik and McInnes, 2022) that due to the extremely stretched image of the solar disk, the quantity of energy delivered is very low at low elevations. Therefore, for more effective passes in terms of energy delivery, the $\epsilon_{\max} > 80$ deg criterion is adopted. It can be seen that $\epsilon_{\max} \approx 90$ deg is achieved for Sun Cable as the orbit is selected according to this farm. Of the remaining three passes, two occur from Bhadla SPF in India (SPF #2) and Longyangxia Dam Solar Park (SPF #9) in China. All three passes have $\epsilon_{\max} > 85$ deg, well above the 80 deg threshold. The first pass after Sun Cable occurs at Bhadla SPF at the 4th hour, i.e., within the third orbit. There is approximately a 10-h gap before the next pass which occurs at the Longyangxia Dam Solar Park. The final pass within 1 day is again at Bhadla SPF in the next orbit. The former two passes are then dusk passes, whereas the latter two are dawn passes. The other passes from these solar farms are also visible in Fig.7, all of which are with a maximum elevation below 65 deg. It is also worth noting from Fig. 7 that multiple SPF are often in view, including those that are not presented in Fig. 8. But only those with near-overhead passes are considered for the analysis here. The properties of reflector passes over these solar farms can then be summarised in Table 4.

Table 4 confirms the near overhead passes on all SPF from Fig. 3. In line with this result, pass durations over the solar farms are also close to the T_{pass} duration at 884.59 km altitude. The duty cycle of the reflectors is relatively low due to the selected orbit and relative scarcity of the large SPF across the Earth. The energy is delivered to all four visible SPF in approximately 65 min of a day. The energy delivered to each SPF can also be seen in Table 4. Bhadla SPF receives the most energy daily, due to the two passes. The daily total energy delivered will be used when the economic aspects are discussed later in Section 6.

In this subsection, the orbit selection and the properties of selected orbit are discussed in the context of near over head passes. However, more orbital passes and further opportunities for solar energy delivery can be found when this requirement is relaxed, which will be discussed next.

3.6. Other possible visits and a daily operational schedule

While only near-overhead passes are considered in the previous section, it is also possible to find other SPF in view, albeit with some longitudinal difference between the target and the reflector. Including those in the daily operations would increase the duty cycle of the reflectors each day and the idle hours can be used more effectively. Albeit lower than the overhead passes, considerable solar energy

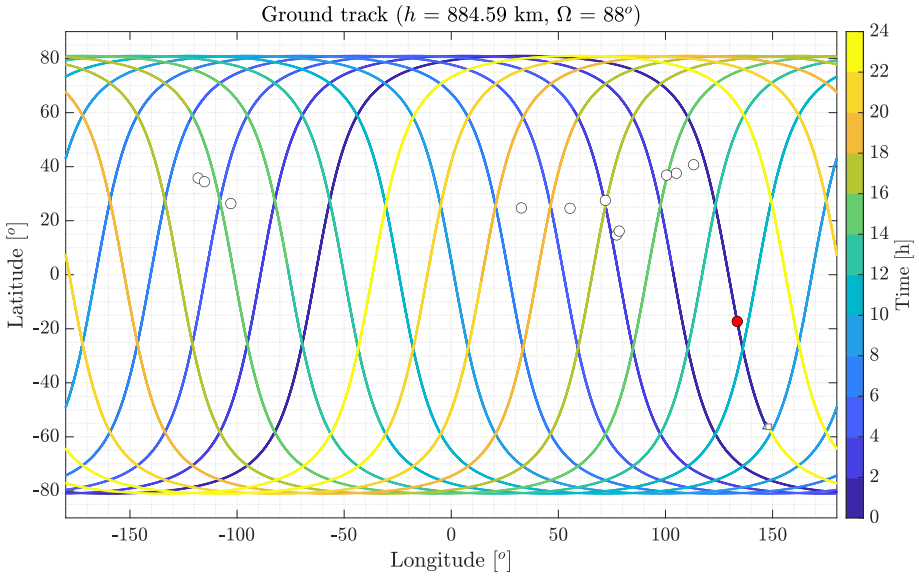

Fig. 7. 1-day groundtrack of the selected orbit. Circles denote the locations of the SPF. Red circle denotes the location of the Sun Cable SPF. Triangle and square points denote the beginning and the end of the simulation, respectively.

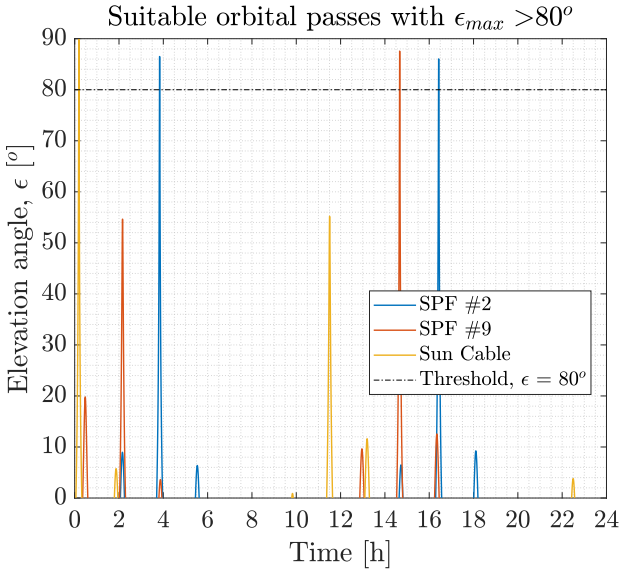

Fig. 8. Suitable solar power farm passes with maximum elevation angle greater than 80 deg.

may still be delivered in these so-called "offset passes," which would improve the conditions for economic breake-ven. Indeed, one can already see second passes for near Sun Cable and Longyangxia (SPF #9) approximately after 12 h from their first pass from Fig. 7. There are also a number of others and some close passes, as well, particularly in the North American region that can be seen in Fig. 7. All of these orbital passes have their highest elevation below 65 deg. Note that some of the SPFs in Table 1 cannot be included in an enhanced reflector operation. This is due to multiple different reasons. For example, Pavagada (SPF #3) and Kurnool (SPF #8) SPF are already in the path of the Bhadla (SPF #2) pass and the Bhadla pass allows for a better pass geometry, hence more solar energy delivery. They cannot be selected operationally due this issue and the attitude control requirements which will be discussed later. The Tengger solar power plant (SPF #5) is also very closely located to Longyangxia (SPF #9), where again the latter offers a better pass geometry. Among the SPF in North America, the orbit ground track in Fig. 7 shows that the ground track follows the path between Villanueva (SPF #10) and Topaz (SPF #12), therefore the energy delivered to these SPF will be higher than the Solar Star plant (SPF #11), which is located to the west of both. With the procedure applied in the previous subsection, the energy delivered is calculated during the identified offset passes.

Notably, the second passes over Sun Cable and Longyangxia (SPF #9) deliver approximately 22.6 MWh and 24.7 MWh, respectively, which is approximately 70% of the solar energy delivered in an overhead pass. Among the other opportunities, orbital passes over Villanueva can deliver 24.43 MWh and 26.94 MWh of solar energy at two different times each day, approximately 12 h apart. The Topaz plant would also be visible in those passes, where the delivered energy would be 27.6 MWh in the first pass and 14.31 MWh in the second. The fact that both targets are visible in the same pass means that an operational choice has to be made. That choice is made to maximise the energy delivered, such that solar energy would be delivered to the Topaz plant in the first visit, whereas it would be delivered to the Villanueva plant in the second. This would allow maximum energy delivery to these two targets with a total of 54.54 MWh. A potential challenge in visiting these plants is that the passes occur in the same orbit after the Bhadla pass. This means that the reflector needs to be reoriented and be ready for the subsequent pass within

Table 4
Summary of reflector passes over different solar power farms.

Solar power farm	Max elevation [deg]	Pass duration [min]	Energy delivered [MWh]
Sun Cable	89.95	16.18	33.06
Bhadla (SPF #2)	86.51	16.14	34.90
Longyangxian (SPF #9)	87.57	16.20	34.58
Bhadla (SPF #2)	86.04	16.20	34.14
	TOTAL	64.72	136.69

approximately 30 min. This will be shown to be possible later in Section 4.

The energy delivered in other orbital passes are relatively modest and less than 15 MWh. Nevertheless, these will be included to maximise the energy delivery to various other large SPF. A schedule can then be defined for the orbiting solar reflectors based on their pass times and delivered energy, as shown in Fig. 9. Fig. 9 shows an enhanced duty cycle for the reflectors. Note in the case of overhead passes only, the total operational time is limited to 65 min, which is less than 5% of a day. With the inclusion of offset passes, the duty cycle is extended to 3.55 h or approximately 15% of a day. More than two overhead pass over a SPF is not possible in a day due to the orbital dynamics constraints and only a few offset passes can deliver meaningful levels of solar energy. Considering the short duration orbital passes (approximately 17 min), the duty cycle may be expected to be relatively low in general, unless SPFs are favourably located on the ground track. Nevertheless, all listed large SPF (other than those operationally infeasible) are visited during a day. This implies an enhanced utility for the reflectors and SPF in various locations, which may also encourage international cooperation. In terms of the total energy delivered, this is now increased to 283.84 MWh as shown in Table 5. This is more than a twofold increase in the total energy delivered compared to overhead passes only. Recall that approximately 33 MWh of solar energy can be delivered in an overhead pass. If that value is considered as a measure of overhead-pass equivalent energy, then 8.6 overhead pass equivalent solar energy can be delivered in a day. This will improve the economic breakeven point.

The analysis here is performed based on the existing orbit and its ground track, but the orbit plane can be modified to further optimise the energy delivered, through passive means such as solar radiation pressure, which will be discussed next.

3.7. Orbit dynamics and control with solar radiation pressure

The effect of solar radiation pressure (SRP) on the selected SSO will be discussed in this section, both as a perturbation and as a means of orbit control. The SRP acceleration experienced by a solar reflector can be expressed as McInnes (2004):

$$a_{\text{srp}} = 2\eta\left(\frac{I_0}{c}\right)\left(\frac{1}{r_{\text{sun}}}\right)^2\left(\frac{1}{\sigma_r}\right)\cos^2\frac{\psi}{2} \tag{15}$$

where c denotes the speed of light whose value is 2.99×10^8 ms^{-1}, r_{sun} is the distance from the Sun in AU, σ_r is the mass-to-area ratio of the reflector, and $\psi/2$ is the angle between the reflector normal and the Sun direction. In this analysis, η is assumed 0.92 and r_{sun} is 1 AU. The SRP acceleration experienced at 1 AU can then be written as McInnes (2004)

$$a_{\text{srp}} = \frac{8.43 \times 10^{-3}}{\sigma_r}\cos^2\frac{\psi}{2} \tag{16}$$

where a_{srp} is in units of ms^{-2} if σ_r is in gm^{-2}. Using this expression, the daily available ΔV can also be estimated for the idealised case of reflector at a constant attitude, except during the passes over SPFs. In this case, the daily available ΔV can be estimated as

$$\Delta V \approx a_{\text{srp}}\Delta T \tag{17}$$

where ΔT is daily available time when SRP can be used for propulsion and is equal to approximately 18 h when the pass durations over SPFs are not included. Fig. 10 shows the SRP acceleration experienced and the daily ΔV available for a fixed density of $\sigma_r = 18.8\text{gm}^{-2}$ and a range of $\psi/2$ values.

In the analysis, $\psi/2$ values between 0 deg (facing the Sun) and 90 deg (edge on) are considered. For nearly face-on configurations (smaller $\psi/2$ values) the SRP acceleration is the highest, here the maximum is equal to 4.5×10^{-4} ms^{-2} but decreases rapidly as $\psi/2$ increases. In line with the SRP acceleration, the daily available ΔV due to SRP is approximately equal to 29ms^{-1} for face-on configurations and decreases accordingly for increasing pitch angles. This means that there is a considerable quantity of ΔV available for orbit modifications. However, it is likely that control laws will not allow a fixed attitude at all times, therefore the results in Fig. 10 only provide an upper bound in ΔV capability due to SRP, which is also subject to change for different reflectivity values.

The SRP acceleration would also act as a perturbing effect on the Sun-synchronous condition. In to order quantify this, the precession of the right ascension of the ascending node, Ω, due to SRP can be expressed as Battin (1999):

$$\Delta\Omega_{\text{srp}} = \frac{a_{\text{srp}}}{H_o \sin i}\int_{t_0}^{t_1} r_o \sin\theta_o \mathrm{d}t \tag{18}$$

where θ_o, H_o and r_o are orbit argument of latitude, angular momentum and radius, respectively, and given as

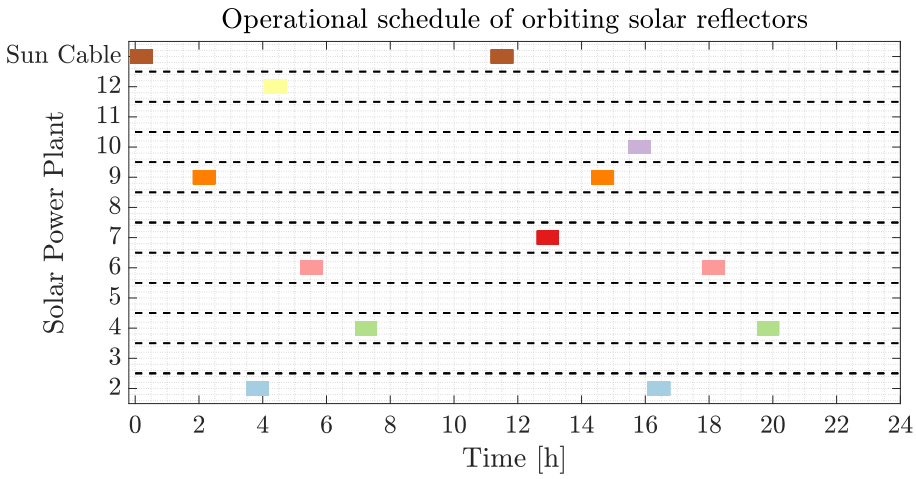

Fig. 9. An operational schedule for orbiting solar reflectors. Blocks of time are not to scaled with pass durations.

Table 5
Tabulated operational schedule and solar energy delivered.

Solar power plant	Time of passage [h]	Energy delivered [MWh]
Sun Cable	0.06–0.32	33.06
SPF #9	2.03–2.29	24.74
SPF #2	3.69–3.97	34.90
SPF #12	4.27–4.53	27.60
SPF #6	5.40–5.67	13.09
SPF #4	7.11–7.36	7.04
Sun Cable	11.37–11.64	22.58
SPF #7	12.82–13.07	6.49
SPF #9	14.53–14.80	34.58
SPF #10	15.69–15.96	26.94
SPF #2	16.29–16.56	34.14
SPF #6	18.01–18.27	11.97
SPF #4	19.72–19.99	6.70
TOTAL		283.84

$$H_o = \sqrt{\mu a(1-e^2)} \quad (19)$$

$$r_o = \frac{a(1-e^2)}{1+e\cos\theta_o} \quad (20)$$

Here, generic expressions are given which includes the orbit eccentricity. Recall that all orbits considered in this paper are circular, i.e., $e = 0$. The integration parameter $\mathrm{d}t$ can also be written in terms of argument of latitude:

$$\mathrm{d}t = \frac{r_o^2}{H_o}\mathrm{d}\theta_o = \frac{a^{3/2}}{\mu}\mathrm{d}\theta_o \quad (21)$$

where $r_o = a$, which would allow Eq. (18) to be rewritten for a circular orbit, as:

$$\Delta\Omega_{\mathrm{srp}} = \frac{a_{\mathrm{srp}} r_o^2}{\mu \sin i}\int_{\theta_1}^{\theta_2} \sin\theta_o \mathrm{d}\theta_o = -\frac{a_{\mathrm{srp}} r_o^2}{\mu \sin i}\cos\theta_o\Big|_{\theta_1}^{\theta_2} \quad (22)$$

Eq. 22 provides the change of Ω over an orbit. The precession rate due to SRP can then be found, dividing Eq. (22) by the orbit period T

$$\dot{\Omega}_{\mathrm{srp}} = \frac{\Delta\Omega_{\mathrm{srp}}}{T} \quad (23)$$

Now that the relevant expressions are derived, first, the perturbing effect of SRP during the passes over SPFs will be investigated, as during those times reflectors are only considered to deliver solar energy and not manoeuvred to alleviate the SRP perturbation. To calculate $\Delta\Omega_{\mathrm{srp}}$, only the pass over the Sun Cable solar farm was considered. The SRP acceleration a_{srp} is calculated based on the actual variation of the reflector normal during the pass through the ψ angle with a target σ_r value of 18.8 gm^{-2}. The numerical integration was carried out between θ_o values where the reflector is in view from the Sun Cable SPF, $\theta_o = -45.7$ deg to 10.6 deg. Note that the difference between the upper and lower bounds of the integral approximately equals twice the cone angle β, 56.3 deg, in accordance with the pass duration calculations in Eq. 10. The integration results in $\Delta\Omega_{\mathrm{srp}} = -8.06 \times 10^{-6}$ rad or -0.00046 deg. The minus sign means an eastward rotation of the orbit plane.

It is now of interest whether the SRP-induced rotation of the orbit plane during the pass can be compensated in the subsequent phase of the orbit. This analysis is more general and will assume a fixed angle of the reflector normal. In circular orbits, for the SRP force to induce a torque that rotates the orbit plane, SRP should be utilised only for one half of the orbit, such that the induced rotation is not cancelled in the other half (Leipold and Wagner, 1996), which can also be deduced from Eq. 22. That means there would be at least two manoeuvres necessary, first to configure the attitude for SRP utilisation and then to configure edgewise (Leipold and Wagner, 1996). In order to quantify the precession rate due to SRP, Eq. 22 is integrated from $\theta_o = 0$ to π at for different attitude angles for the reflector mass density, $\sigma_r = 18.8\ \mathrm{gm}^{-2}$. The results are shown in Fig. 11.

For the reference case of 18.8 gm^{-2} considered here, the maximum change in orbit plane is approximately 0.1 deg/-day, i.e., approximately 10% of the required shift of orbit plane for the Sun-synchronous condition, 0.9856 deg/day.

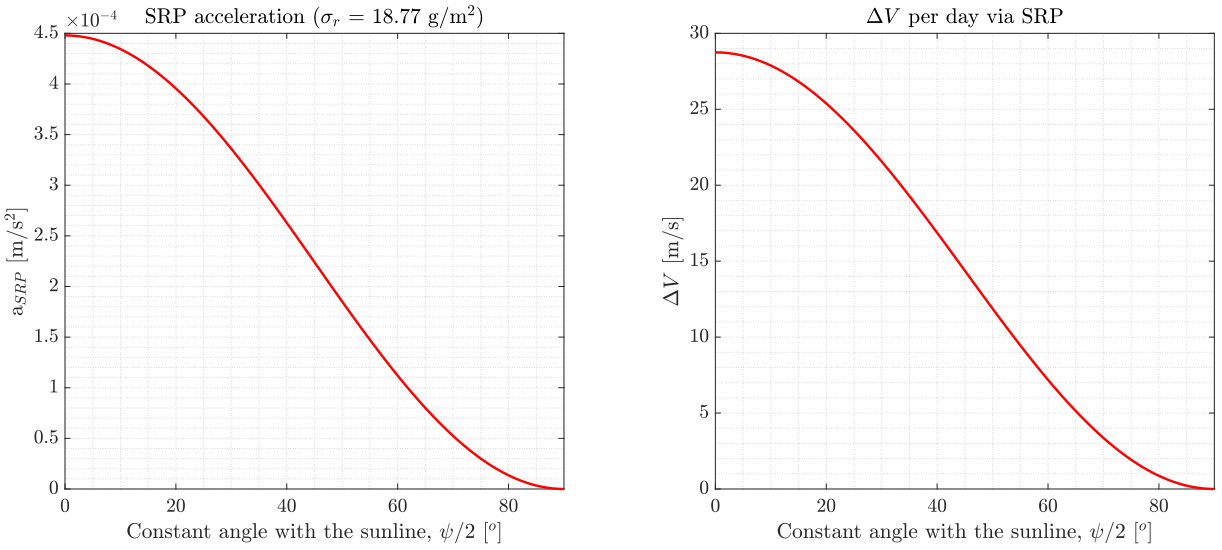

(a) SRP acceleration

(b) ΔV available

Fig. 10. SRP acceleration and ΔV available per day by leveraging solar radiation pressure. Pass durations over solar power farms are not considered in the ΔV analysis.

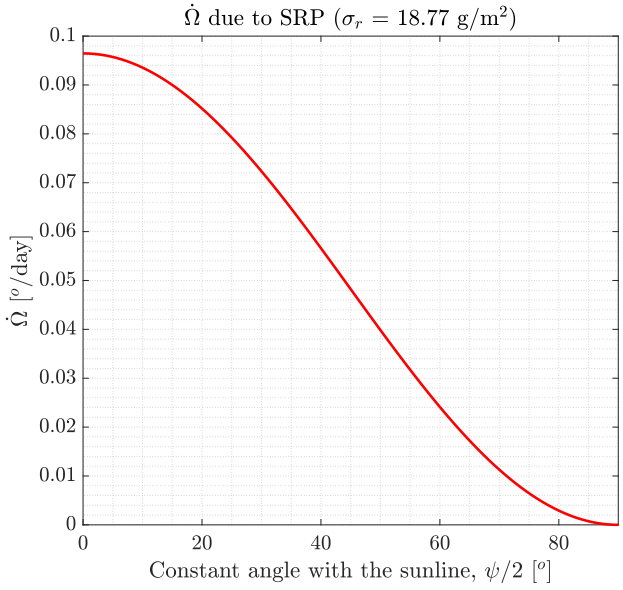

Fig. 11. Per-day equivalent change in orbit plane by SRP for the reflector in this paper ($\sigma_r = 18.8$ gm^{-2}).

The selected orbit completes 14 revolution per day, which means in each orbit, the orbit plane shifts approximately 6.88×10^{-3} deg. This is an order of magnitude higher than the orbit plane shift experienced during the Sun Cable pass. Therefore, it can be stated that the SRP perturbation during the orbital passes above SPFs can easily be compensated in the subsequent part of the orbit. Even though it is not analysed, it is also possible that the precession due to SRP during one pass is compensated in another, such that even less manoeuvring is required. This can even be generalised for the passes over all SPFs, as the pass geometry and duration are approximately the same.

The results have further implications, as well. The SRP can be used to shift the orbit plane for potentially more suitable ground tracks to reach more SPFs or to avoid unfavourable seasonal changes. The orbit here is chosen among virtually endless possible orbits and its choice was based on the Sun Cable SPF. If this requirement is relaxed, then Fig. 7 shows close passes over several SPF. Those can be made close to an overhead pass by a slight shift in the orbit in the eastward direction, which could enable two daily passes over two SPF, in addition to another one pass each over two targets. A 1-degree shift in orbit plane could be achieved in approximately 10 days by a 18.8 gm^{-2} reflector. Moreover, SRP could also enable Sun-synchronous condition to be satisfied for, for example, perfectly polar orbits (i.e., $i = 90$ deg). Perfectly polar orbits do not experience the Earth oblateness perturbation as implied in Eq. 3, therefore the orbit plane is not precessed as for orbits with $i \neq 90$ deg. Perfectly polar orbits can then be artificially precessed by SRP. Furthermore, more sophisticated use of SRP could allow for the Sun-synchronous condition to be achieved for inclinations other than the inclination imposed by a selected altitude and eccentricity, by compensating the deficit or cancelling the surplus of precession due to the Earth's oblateness. Further to this last point, SRP could also be used to minimise the effect of air drag when it is included in an operational scenario (Mengali and Quarta, 2005). The reflector attitude could in principle be configured to edge-on orientation with respect to the Sun as well, which would allow both a low-drag configuration and minimised stray light reflection. This will be investigated as the "idle mode" of reflector orientation alongside other attitude control aspects in the next section.

4. Reflector attitude dynamics

The reflector must be adequately steered in order to reflect sunlight to the selected SPF and perform reorientation manoeuvres. The attitude control actuators must therefore be sized based on the maximum control effort (to be expressed in terms of angular momentum and torque) during a 24 h cycle. To do so, a set of operational phases are first defined and the required angular velocities and angular accelerations are derived analytically for each phase. Then, an operational reorientation time schedule is defined, based on constraints to be discussed. The actuator requirements are then derived, which will eventually determine the size of the reflector.

4.1. Symbols and definitions

Given two quaternions $\mathbf{p} = [p_0, \mathbf{p}_v]$ and $\mathbf{q} = [q_0, \mathbf{q}_v]$ (where the first element is the scalar part and the second element is the vectorial part), the quaternion tensor product is indicated with the symbol $\otimes$ and is defined as:

$$\mathbf{p} \otimes \mathbf{q} = [p_0 q_0, -\mathbf{p}_v \cdot \mathbf{q}_v (p_0 \mathbf{q} + q_0 \mathbf{p} + \mathbf{p}_v \times \mathbf{q}_v)] \tag{24}$$

where the symbols $\cdot$ and $\times$ denote the internal and external product, respectively. An upper bar is used to indicate the adjoint quaternion operator, defined as:

$$\bar{\mathbf{q}} = [q_0, -\mathbf{q}_v] \tag{25}$$

4.2. Operation phases and target reference frame

The target reference frame TRF defines the desired orientation of the reflector reference frame RRF and it is defined based on the operational phase, where TRF and TTF are defined in Section 3.1:

- Ground tracking phase. In this phase the reflector is steered to redirect sunlight to a SPF for the entire duration of the pass.
- Idle phase. When the reflector is not tracking a SPF its attitude must be changed to avoid reflecting sunlight to unwanted ground locations.
- Reorientation phase. This phase represents the transition between the ground tracking phase and the idle phase.
- Angular momentum dumping phase. This is an actuator desaturation phase, in which the angular momentum accumulated during the manoeuvres is released, using solar radiation pressure to generate desaturation torques. This phase is scheduled between the end of the last pass and the beginning of a new cycle.

Fig. 12 shows the sequence of TRFs during a single sidereal day cycle. In the following sections the orientation of the TRF with respect to the ECIRF is defined for each operational phase. Moreover, the angular velocity and acceleration of the TRF are also derived; these parameters will be required for the definition of the attitude control actuator requirements and the control law, to be discussed later.

4.2.1. Ground tracking phase

In order to reflect sunlight to a given SPF, the direction of the reflected light $\hat{\mathbf{u}}_r$ must be parallel and opposite to the vector connecting the SPF to the reflector $\mathbf{r}_{gr} = \mathbf{r}_r - \mathbf{r}_g$ (see Fig. 13), i.e.,

$$\hat{\mathbf{u}}_r = -\frac{\mathbf{r}_{gr}}{|\mathbf{r}_{gr}|} \tag{26}$$

Then, let $\hat{\mathbf{u}}_i$ be the unit vector pointing in the direction of the incoming light. The direction of the reflector normal is found by imposing that the angle of incidence and reflection of the sunlight are equal and that the unit vectors $\hat{\mathbf{u}}_i, \hat{\mathbf{u}}_r$ and $\hat{\mathbf{z}}_t$ are coplanar:

$$\hat{\mathbf{z}}_t = \frac{\hat{\mathbf{u}}_r - \hat{\mathbf{u}}_i}{|\hat{\mathbf{u}}_r - \hat{\mathbf{u}}_i|} \tag{27}$$

Note that the definition of unit vectors $\hat{\mathbf{x}}_t$ and $\hat{\mathbf{y}}_t$ remains undefined, given that any rotation of the TRF about $\hat{\mathbf{z}}_t$ does not change the direction of the reflected light $\hat{\mathbf{u}}_r$. It is chosen here to constrain the unit vector $\hat{\mathbf{y}}_t$ to be perpendicular to the plane generated by $\hat{\mathbf{z}}_t$ and the orbit angular momentum vector $\hat{\mathbf{h}}_o$. Then, the orientation of the TRF during the tracking phase is fully defined by:

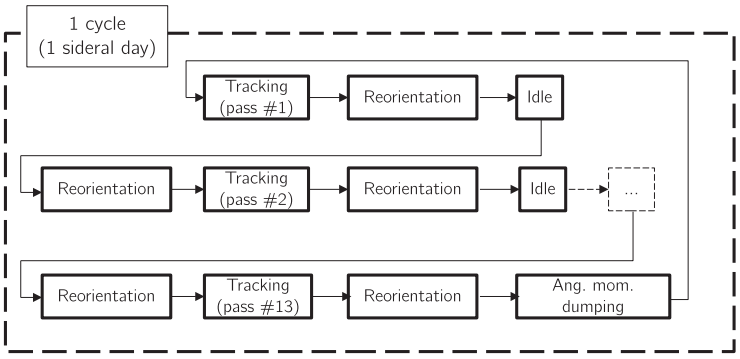

Fig. 12. Sequence of TRFs during one sidereal day cycle.

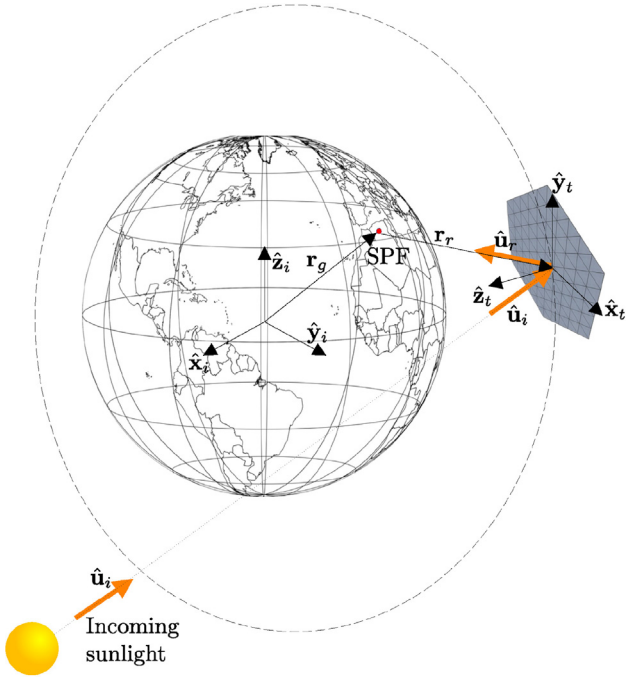

Fig. 13. Target reference frame during the ground tracking phase.

$$\hat{\mathbf{x}}_t = \hat{\mathbf{y}}_t \times \hat{\mathbf{z}}_t \tag{28a}$$

$$\hat{\mathbf{y}}_t = \frac{\hat{\mathbf{z}}_t \times \hat{\mathbf{h}}_o}{|\hat{\mathbf{z}}_t \times \hat{\mathbf{h}}_o|} \tag{28b}$$

$$\hat{\mathbf{z}}_t = \frac{\hat{\mathbf{u}}_r - \hat{\mathbf{u}}_i}{|\hat{\mathbf{u}}_r - \hat{\mathbf{u}}_i|} \tag{28c}$$

The rotation matrix from ECIRF to TRF is defined as:

$$R^{TRF}_{ECIRF} = [\hat{\mathbf{x}}_t, \hat{\mathbf{y}}_t, \hat{\mathbf{z}}_t] \tag{29}$$

where the unit vectors are written with respect to the ECIRF. The orientation of the TRF can then be expressed from Eq. 29 using unit quaternions. In the next section, the angular velocity and angular acceleration of the TRF during the ground tracking phase will be calculated.

4.2.2. Target angular velocity and angular acceleration

From the definition of the angular velocity vector, the derivatives of the TRF unit vectors (Eqs. (28)) are given by the external products:

$$\dot{\hat{\mathbf{y}}}_t = \boldsymbol{\omega}_t \times \hat{\mathbf{y}}_t \tag{30}$$

$$\dot{\hat{\mathbf{z}}}_t = \boldsymbol{\omega}_t \times \hat{\mathbf{z}}_t \tag{31}$$

By cross multiplying both sides of Eq. (31) by $\hat{\mathbf{z}}_t$:

$$\begin{aligned} \hat{\mathbf{z}}_t \times \dot{\hat{\mathbf{z}}}_t &= \hat{\mathbf{z}}_t \times (\boldsymbol{\omega}_t \times \hat{\mathbf{z}}_t) \\ &= \boldsymbol{\omega}_t - \hat{\mathbf{z}}_t(\hat{\mathbf{z}}_t \cdot \boldsymbol{\omega}_t) \end{aligned} \tag{32}$$

The required angular velocity can then be found by solving Eq. (32) for $\boldsymbol{\omega}_t$. To proceed, the dot product $\hat{\mathbf{z}}_t \cdot \boldsymbol{\omega}_t$ must be written as a function of the target unit vectors or their derivatives only. From the definition of $\hat{\mathbf{y}}_t$ (Eq. (28b)):

$$\begin{aligned} \dot{\hat{\mathbf{y}}}_t &= \boldsymbol{\omega}_t \times \frac{\hat{\mathbf{z}}_t \times \hat{\mathbf{h}}_o}{|\hat{\mathbf{z}}_t \times \hat{\mathbf{h}}_o|} \\ &= |\hat{\mathbf{z}}_t \times \hat{\mathbf{h}}_o|^{-1} \left[\hat{\mathbf{z}}_t(\boldsymbol{\omega}_t \cdot \hat{\mathbf{h}}_o) - \hat{\mathbf{h}}_o(\hat{\mathbf{z}}_t \cdot \boldsymbol{\omega}_t) \right] \end{aligned} \tag{33}$$

and therefore:

$$\hat{\mathbf{z}}_t \cdot \boldsymbol{\omega}_t = (\hat{\mathbf{z}}_t \cdot \hat{\mathbf{h}}_o)(\boldsymbol{\omega}_t \cdot \hat{\mathbf{h}}_o) - (\dot{\hat{\mathbf{y}}}_t \cdot \hat{\mathbf{h}}_o)|\hat{\mathbf{z}}_t \times \hat{\mathbf{h}}_o|$$

Moreover:

$$\begin{aligned} \hat{\mathbf{h}}_o \times \dot{\hat{\mathbf{y}}}_t &= \hat{\mathbf{h}}_o \times (\boldsymbol{\omega}_t \times \hat{\mathbf{y}}_t) \\ &= \boldsymbol{\omega}_t(\hat{\mathbf{h}}_o \cdot \hat{\mathbf{y}}_t) - \hat{\mathbf{y}}_t(\hat{\mathbf{h}}_o \cdot \boldsymbol{\omega}_t) \\ &= -\hat{\mathbf{y}}_t(\hat{\mathbf{h}}_o \cdot \boldsymbol{\omega}_t) \end{aligned} \tag{35}$$

where the last step follows from the fact that the orbit angular momentum vector is by definition perpendicular to $\hat{\mathbf{y}}_t$ (Eq. (28b)). Taking the dot product of both sides of Eq. (35) by $\hat{\mathbf{y}}_t$ and solving for $\hat{\mathbf{h}}_o \cdot \boldsymbol{\omega}_t$ yields:

$$\hat{\mathbf{h}}_o \cdot \boldsymbol{\omega}_t = -(\hat{\mathbf{h}}_o \times \dot{\hat{\mathbf{y}}}_t) \cdot \hat{\mathbf{y}}_t$$

Finally, substituting Eqs. (36) and (34) into Eq. (32) and solving for $\boldsymbol{\omega}_t$ yields:

$$\begin{aligned} \boldsymbol{\omega}_t &= \hat{\mathbf{z}}_t \times \dot{\hat{\mathbf{z}}}_t \\ &\quad - \hat{\mathbf{z}}_t \left[(\hat{\mathbf{z}}_t \cdot \hat{\mathbf{h}}_o)(\hat{\mathbf{h}}_o \times \dot{\hat{\mathbf{y}}}_t) \cdot \hat{\mathbf{y}}_t + (\dot{\hat{\mathbf{y}}}_t \cdot \hat{\mathbf{h}}_o)|\hat{\mathbf{z}}_t \times \hat{\mathbf{h}}_o| \right] \end{aligned} \tag{37}$$

where the derivatives of the unit vectors $\hat{\mathbf{y}}_t$ and $\hat{\mathbf{z}}_t$ can be written as:

$$\begin{aligned} \dot{\hat{\mathbf{y}}}_t &= -\frac{d}{dt}\frac{\mathbf{r}_{gr}}{|\mathbf{r}_{gr}|} \\ &= \frac{\mathbf{r}_{gr} \cdot \dot{\mathbf{r}}_{gr}}{|\mathbf{r}_{gr}|^3}\mathbf{r}_{gr} - \frac{\dot{\mathbf{r}}_{gr}}{|\mathbf{r}_{gr}|} \end{aligned} \tag{38}$$

$$\begin{aligned} \dot{\hat{\mathbf{z}}}_t &= \frac{d}{dt}\frac{\hat{\mathbf{z}}_t \times \hat{\mathbf{h}}_o}{|\hat{\mathbf{z}}_t \times \hat{\mathbf{h}}_o|} \\ &= -\frac{(\hat{\mathbf{z}}_t \times \hat{\mathbf{h}}_o) \cdot (\dot{\hat{\mathbf{z}}}_t \times \hat{\mathbf{h}}_o)}{|\hat{\mathbf{z}}_t \times \hat{\mathbf{h}}_o|^3}(\hat{\mathbf{z}}_t \times \hat{\mathbf{h}}_o) + \frac{\dot{\hat{\mathbf{z}}}_t \times \hat{\mathbf{h}}_o}{|\hat{\mathbf{z}}_t \times \hat{\mathbf{h}}_o|} \end{aligned} \tag{39}$$

Hence, given the position and velocity of the reflector and the SPF at a given time the vectors, $\hat{\mathbf{y}}_t, \hat{\mathbf{z}}_t, \dot{\hat{\mathbf{y}}}_t, \dot{\hat{\mathbf{z}}}_t$ are known and the angular velocity of the target reference frame $\boldsymbol{\omega}_t$ can therefore be calculated. Note that the instantaneous angular momentum unit vector $\hat{\mathbf{h}}_o$ is also known given the position and velocity of the reflector.

The target angular acceleration can then be obtained by differentiating Eq. (37):

$$\begin{aligned} \dot{\boldsymbol{\omega}}_t &= \frac{d}{dt}(\hat{\mathbf{z}}_t \times \dot{\hat{\mathbf{z}}}_t) - \dot{\hat{\mathbf{z}}}_t \left[(\hat{\mathbf{z}}_t \cdot \hat{\mathbf{h}}_o)(\hat{\mathbf{h}}_o \times \dot{\hat{\mathbf{y}}}_t) \cdot \hat{\mathbf{y}}_t + (\dot{\hat{\mathbf{y}}}_t \cdot \hat{\mathbf{h}}_o)|\hat{\mathbf{z}}_t \times \hat{\mathbf{h}}_o| \right] \\ &\quad - \hat{\mathbf{z}}_t \Bigg\{ \frac{d}{dt}(\hat{\mathbf{z}}_t \cdot \hat{\mathbf{h}}_o)(\hat{\mathbf{h}}_o \times \dot{\hat{\mathbf{y}}}_t) \cdot \hat{\mathbf{y}}_t \\ &\quad + (\hat{\mathbf{z}}_t \cdot \hat{\mathbf{h}}_o) \left[\frac{d}{dt}(\hat{\mathbf{h}}_o \times \dot{\hat{\mathbf{y}}}_t) \cdot \hat{\mathbf{y}}_t + (\hat{\mathbf{h}}_o \times \dot{\hat{\mathbf{y}}}_t) \cdot \dot{\hat{\mathbf{y}}}_t \right] \\ &\quad + \frac{d}{dt}(\dot{\hat{\mathbf{y}}}_t \cdot \hat{\mathbf{h}}_o)|\hat{\mathbf{z}}_t \times \hat{\mathbf{h}}_o| + (\dot{\hat{\mathbf{y}}}_t \cdot \hat{\mathbf{h}}_o)\frac{d}{dt}|\hat{\mathbf{z}}_t \times \hat{\mathbf{h}}_o| \Bigg\} \end{aligned} \tag{40}$$

The terms $\dot{\hat{\mathbf{h}}}_o$ and $\dot{\hat{\mathbf{u}}}_i$ have been neglected as their absolute value is three order of magnitudes smaller than the orbital

angular velocity and therefore reasonably negligible for the purpose of this paper. This assumption will also be used later.

The components of the target angular velocity and angular acceleration vector (expressed in the TRF) are shown in Fig. 14 for the Sun Cable overhead pass (pass #1) and the Sun Cable offset pass (pass #7). Also shown are the Euler angles of the TRF, assuming a $x \rightarrow y \rightarrow z$ axis rotation order. The angular velocity vector for the overhead pass mainly lies in the reflector xz plane, with x and z components being nearly equal. The y component of the angular velocity is approximately zero, as the reflector maintains a quasi-constant pitch angle of 45 deg (see Figs. 14e and 14f). The small variation of the y component of the angular velocity is due to the east–west relative motion between the reflector and the SPF associated to the Earth rotation. The ω_x and ω_z components are instead different for an offset pass, due to the more complex three-dimensional geometry of the pass in this case. The angular velocity peak is reached at the half pass time in both cases, when the reflector has reached its maximum elevation above the local horizon and the distance between the reflector and the SPF is minimum. The angular acceleration plots reveal that $|\boldsymbol{\omega}_t|$ has two local maxima, before and after the maximum elevation has been reached. Higher angular accelerations are clearly associated to larger control torques, as it will be discussed later.

The pass with the largest $|\boldsymbol{\omega}_t|$ and $|\dot{\boldsymbol{\omega}}_t|$ is the second pass over the Longyanxia SPF, with $\max|\boldsymbol{\omega}_t| = 9.38\times 10^{-3}$ rad s^{-1} and $\max|\dot{\boldsymbol{\omega}}_t| = 4.86 \times 10^{-5}$ rad s^{-2}. The components of the angular velocity and angular acceleration vector at peak magnitude are $\boldsymbol{\omega}_t = [7.89 \times 10^{-3}, 5.86\times 10^{-4}, 5.05 \times 10^{-3}]$ rad s^{-1} and $\dot{\boldsymbol{\omega}}_t = [4.11 \times 10^{-5}, 9.36\times 10^{-6}, 2.42 \times 10^{-5}]$ rad s^{-2}.

4.2.3. Idle phase

When the mirror is not reflecting sunlight to a SPF, its attitude should be adjusted to avoid reflecting sunlight to unwanted Earth locations. This can be achieved, for example, by either maximising or minimizing the effective reflector area facing the Sun. Here, the second option is chosen, to minimize the effects of solar radiation pressure during this phase, although use of SRP for orbital corrections may be considered in future studies, as discussed in Section 3.7. Given that the selected right ascension of the ascending node is nearly 90 deg, an approximate Sun edge-on condition can be obtained by pointing the reflector normal towards the centre of the ECIRF, i.e., by imposing $\hat{\mathbf{z}}_t = -\mathbf{r}_r/|\mathbf{r}_r|$. The x-axis is then arbitrarily aligned with the incoming Sunlight direction and the y-axis completes the right hand triad. Therefore:

$$\hat{\mathbf{x}}_t = -\hat{\mathbf{u}}_i \tag{41a}$$

$$\hat{\mathbf{y}}_t = \frac{\hat{\mathbf{z}}_t \times \hat{\mathbf{x}}_t}{|\hat{\mathbf{z}}_t \times \hat{\mathbf{x}}_t|} \tag{41b}$$

$$\hat{\mathbf{z}}_t = -\frac{\mathbf{r}_r}{|\mathbf{r}_r|} \tag{41c}$$

As done in the previous section, it can be shown that the angular velocity vector in this case is parallel to the $\hat{\mathbf{x}}_t$ axis and its magnitude is equal to the orbital angular velocity, i.e.,

$$\boldsymbol{\omega}_t = \omega_o \hat{\mathbf{x}}_t \tag{42}$$

The variation of the orbital angular velocity due to the J_2 effect can reasonably be neglected for the purpose of this analysis, such that $\dot{\boldsymbol{\omega}}_t \approx 0$

4.2.4. Reorientation phase

The reorientation phase is defined as the transition between the tracking and the idle phase and vice versa. Instead of changing the attitude reference via a step command, the reference attitude is changed continuously, to avoid unwanted oscillations, overshoots, or large angular velocities during the transition phases. Furthermore, this permits to study the effect of the reorientation phase on the required angular momentum and torque without the need to run the full closed-loop control simulation.

Consider, for example, a transition from the tracking phase to the idle phase (the case for the opposite transition is equivalent). Then, let $\mathbf{q}_0$ and $\mathbf{q}_f$ be the required attitude quaternions at end of the tracking phase and at the beginning of the idle phase, respectively (or, equivalently, at the beginning and at the end of the reorientation phase). Moreover, let $\mathbf{q}\prime_0$ and $\mathbf{q}\prime_f$ be their derivatives and let t_{reor} be the reorientation time (to be selected). The reference attitude quaternion during the reorientation phase is then defined as a cubic polynomial in the form:

$$q_i(t) = a_{i,0} + a_{i,1}t + a_{i,2}t^2 + a_{i,3}t^3, \quad i = 1, \ldots, 4 \tag{43}$$

The coefficients a_i are then found by imposing continuity of the quaternion polynomial and its derivative at the endpoints, i.e., by solving the boundary value problem:

$$\begin{bmatrix} 1 & t_0 & t_0^2 & t_0^3 \\ 1 & t_f & t_f^2 & t_f^3 \\ 0 & 1 & 2t_0 & 3t_0^2 \\ 0 & 1 & 2t_f & 3t_f^2 \end{bmatrix} \begin{bmatrix} a_0 \\ a_1 \\ a_2 \\ a_3 \end{bmatrix} = \begin{bmatrix} q_{0,i} \\ q_{f,i} \\ q\prime_{0,i} \\ q\prime_{f,i} \end{bmatrix}, \quad i = 1, \ldots, 4 \tag{44}$$

where $t_f = t_0 + t_{\text{reor}}$. Moreover, $q_{0,i}$ and $q_{f,i}$ represent the i-th component of the quaternions $\mathbf{q}_0$ and $\mathbf{q}_f$, respectively. Then, the attitude quaternion variation during the reorientation phase depends only on the reorientation time t_{reor}. The angular velocity and angular accelerations can then be found using basic quaternion algebra [2] (Schwab, 2002):

$$[0, \boldsymbol{\omega}_t] = 2\bar{\mathbf{q}} \otimes \dot{\mathbf{q}} \tag{45a}$$

$$[0, \dot{\boldsymbol{\omega}}_t] = 2\left(\dot{\bar{\mathbf{q}}} \otimes \dot{\mathbf{q}} + \bar{\mathbf{q}} \otimes \ddot{\mathbf{q}}\right) \tag{45b}$$

[2] Note that the left hand side of Eqs. (45) has the dimension of a quaternion with the first scalar component being 0 and the vectorial part being the angular velocity (Eq. (45a)) and the angular acceleration (Eq. (45b)).

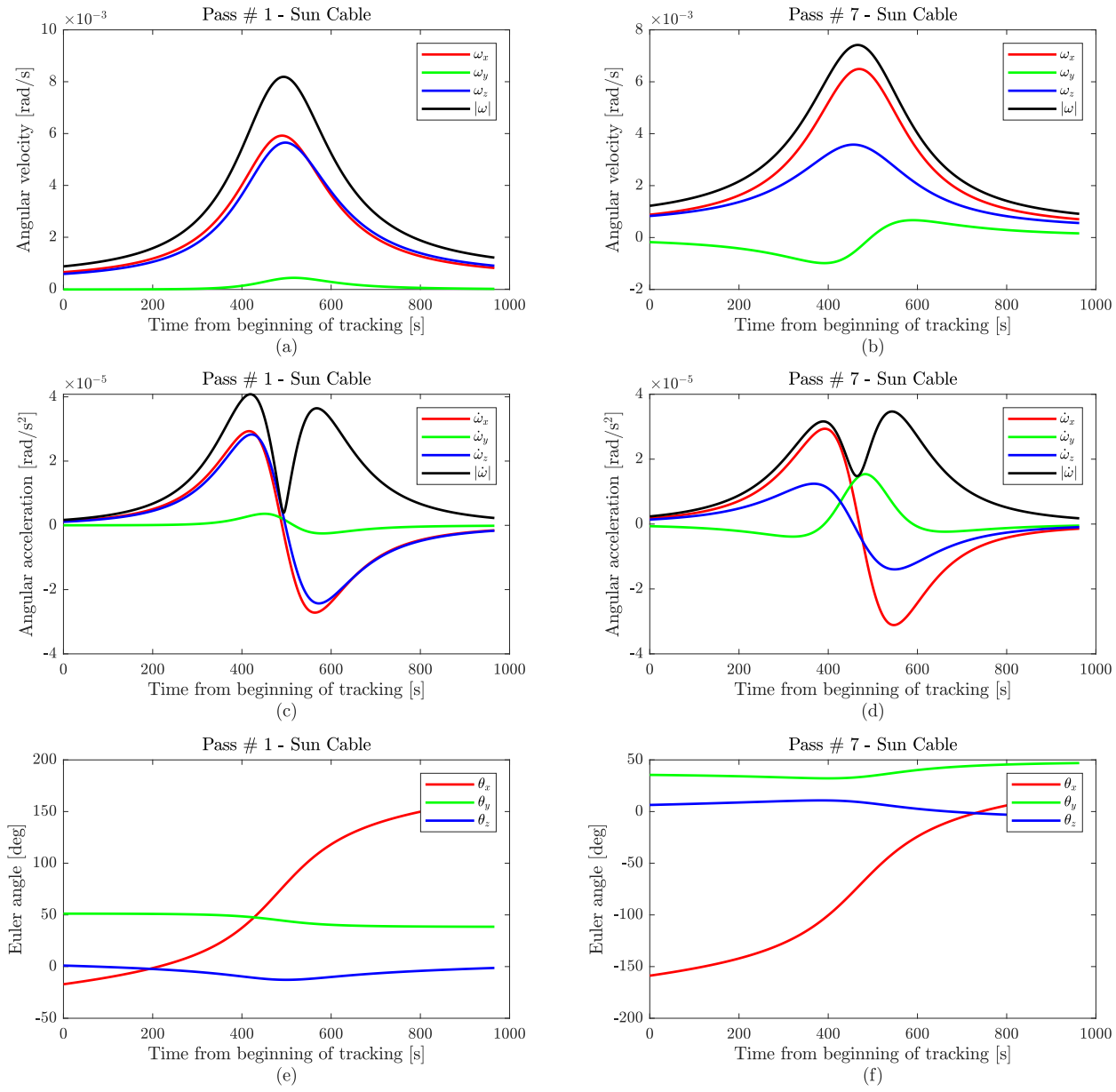

Fig. 14. Angular velocity, angular acceleration and Euler angles of the TRF associated with the ground tracking phase for passes 1 (Sun Cable overhead) and 7 (Sun Cable offset).

The reorientation time t_{reor} is then chosen based on constraints on the maximum angular momentum and torque during this phase, which will be discussed later.

4.2.5. Angular momentum dumping phase

During this phase, external torque provided by SRP is exploited to desaturate the actuators. To maximise the magnitude of the torque, the reflector must be reoriented face-on to the Sun, i.e., with its normal parallel to the sunlight direction, i.e., $\hat{\mathbf{z}}_t = -\hat{\mathbf{u}}_i$. The target reference frame during this phase is defined as follows:

$$\hat{\mathbf{z}}_t = -\hat{\mathbf{u}}_i \tag{46a}$$

$$\hat{\mathbf{x}}_t = \frac{\hat{\mathbf{z}}_i \times \hat{\mathbf{z}}_t}{|\hat{\mathbf{z}}_i \times \hat{\mathbf{z}}_t|} \tag{46b}$$

$$\hat{\mathbf{y}}_t = \frac{\hat{\mathbf{z}}_t \times \hat{\mathbf{x}}_t}{\hat{\mathbf{z}}_t \times \hat{\mathbf{x}}_t} \tag{46c}$$

During a full 24 h cycle the direction of the sunlight $\hat{\mathbf{u}}_i$ can be considered constant, such that $\boldsymbol{\omega}_t \approx \mathbf{0}$ and $\dot{\boldsymbol{\omega}}_t \approx \mathbf{0}$.

4.3. Angular momentum and torque requirements

The attitude dynamics of the reflector is governed by the Euler equation:

$$\dot{\mathbf{H}}_{\text{tot}} + \boldsymbol{\omega}_r \times \mathbf{H}_{\text{tot}} = \mathbf{T}_{\text{ext}} \tag{47}$$

where term $\mathbf{H}_{\text{tot}}$ is the total angular momentum of the reflector and $\boldsymbol{\omega}_r$ is its angular velocity. The reflector angular momentum is given by the sum

$$\mathbf{H}_{\text{tot}} = \mathbf{H}_r + \mathbf{H}_{\text{cmg}} \tag{48}$$

where the first term is the angular momentum of the reflector (excluding the contribution of the actuator) and the second term is the angular momentum generated by the actuator (to be discussed later). The term $\mathbf{T}_{\text{ext}}$ is the external perturbation torque acting on the reflector. The only external torque considered here is the gravity gradient torque, as other perturbations can be reasonably neglected at the selected orbit altitude (Çelik et al., 2022; Viale and McInnes, 2023). The gravity gradient torque can be expressed as Wertz (2012):

$$\mathbf{T}_{gg} = \frac{3\mu}{|\mathbf{r}_r|^3}\hat{\mathbf{r}}_r \times \mathbf{J}\hat{\mathbf{r}}_r \tag{49}$$

where $\hat{\mathbf{r}}_r = \mathbf{r}_r/|\mathbf{r}_r|$ and $\mathbf{J}$ is the reflector inertia tensor. As will be discussed later in Section 5, the reflector structure has a modular hexagonal shape. The inertia tensor can therefore be expressed as:

$$\mathbf{J} = \begin{bmatrix} J_{xx} & 0 & 0 \\ 0 & J_{yy} & 0 \\ 0 & 0 & J_{zz} \end{bmatrix} = \frac{5\sqrt{3}}{16} l^4 \sigma_{\text{str}} \begin{bmatrix} 1 & 0 & 0 \\ 0 & 1 & 0 \\ 0 & 1 & 2 \end{bmatrix} \tag{50}$$

where l and σ_{str} are the reflector size and the areal density of the structure (excluding the contribution of the actuator), respectively. As it will be discussed later, the additional inertia tensor due to the CMGs is negligible with respect to the reflector inertia and therefore the inertia tensor can be considered constant and such that $J_{xx} = J_{yy}$.

Substituting Eq. (48) into Eq. (47) the attitude dynamics equation can be rewritten as a function of the control torque:

$$\mathbf{J}\dot{\boldsymbol{\omega}}_r + \boldsymbol{\omega}_r \times \mathbf{J}\boldsymbol{\omega}_r = \mathbf{T}_c + \mathbf{T}_{gg} \tag{51}$$

where the term

$$\mathbf{T}_c = -\dot{\mathbf{H}}_r - \boldsymbol{\omega}_r \times \mathbf{H}_r \tag{52}$$

represents the control torque generated by the CMGs.

The reflector angular angular momentum $\mathbf{H}_r$ is, by definition:

$$\mathbf{H}_r = [J_{xx}\omega_x, J_{yy}\omega_y, J_{zz}\omega_z]^T \tag{53}$$

Given that $J_{xx} = J_{yy} = J_{zz}/2$, Eq. (53) can rearranged as:

$$\frac{\mathbf{H}_r}{J_{xx}} = [\omega_x, \omega_y, 2\omega_z]^T \tag{54}$$

The parameter $|\mathbf{H}_r|/J_{xx} = \sqrt{\omega_x^2 + \omega_y^2 + 4\omega_z^2}$ will be herein referred to as the specific angular momentum and it is independent of the reflector size. Effectively, it represents the angular momentum vector of the reflector scaled by a factor J_{xx}, which only depends on the reflector size and areal density. Clearly, a larger reflector angular momentum implies a larger actuator angular momentum. Equivalently, from Eq. (47), the specific control torque vector can be defined as:

$$\frac{\mathbf{T}_c}{J_{xx}} = \begin{bmatrix} \dot{\omega}_x + \omega_y\omega_z - 3\frac{\mu}{|\mathbf{r}_r|^3}\hat{r}_{ry}\hat{r}_{rz} \\ \dot{\omega}_y + \omega_x\omega_z - 3\frac{\mu}{|\mathbf{r}_r|^3}\hat{r}_{rx}\hat{r}_{rz} \\ 2\dot{\omega}_z \end{bmatrix} \tag{55}$$

where $\hat{r}_{rx}, \hat{r}_{ry}$ and $\hat{r}_{rz}$ are the components of the unit vector $\hat{\mathbf{r}}_r$ in the x, y and z direction, respectively. Then, the specific angular momentum and torque required during the tracking phase can be found by substituting the TRF angular velocity and angular acceleration (Eqs. (37) and (40)) into Eqs. (53) and (55). Fig. 15 shows the maximum specific angular momentum and torque for each scheduled pass (the results are normalised with respect to the first Sun Cable pass). It is apparent that the third pass, over the Bhadla SPF, requires the largest angular momentum and torque, with $\max|\mathbf{H}_r|/J_{xx} = 1.13 \times 10^{-2}\ \text{s}^{-1}$ and $\max|\mathbf{T}_c|/J_{xx} = 8.28 \times 10^{-5}\ \text{s}^{-2}$. These parameters are then selected as threshold values for the determination of the reorientation time, which will be discussed in the next section.

4.3.1. Selection of the reorientation time

The required angular momentum and torque during the reorientation phase depends on the allocated reorientation time. Clearly, a larger (smaller) angular momentum and torque must be provided by the actuators for smaller (larger) reorientation times. Here, it is chosen to select the reorientation time for each pass such that the peak angular momentum and torque during each reorientation phase do not exceed the maxima found in the previous section for the Bhadla pass. This constraint implies that a minimum reorientation time before and after each pass can be defined. On the other hand, an upper bound on the reorientation time is given by the time between consecutive passes.

Fig. 16 shows the variation of the specific angular momentum and torque as a function of the reorientation time for the first Sun Cable pass. In particular, the black and red line represent the variation of those parameters before and after the pass, respectively. Also shown with a dashed line are the threshold values $(\mathbf{H}_r/J_{xx})_{\max}$ and $(\mathbf{T}_c/J_{xx})_{\max}$, obtained in the previous section. The plots show that a larger reorientation time is required to satisfy the maximum torque constraint. In particular, the orientation time must be larger than 504 s and 381 s before and after the first Sun Cable pass, respectively. This analysis can be repeated for each scheduled pass to identify the minimum reorientation time for each pass. This is shown in Fig. 17, together with the maximum reorientation time. The sum of the selected reorientation times for consecutive passes is always smaller than the the maximum time available, confirming that the proposed tracking schedule is

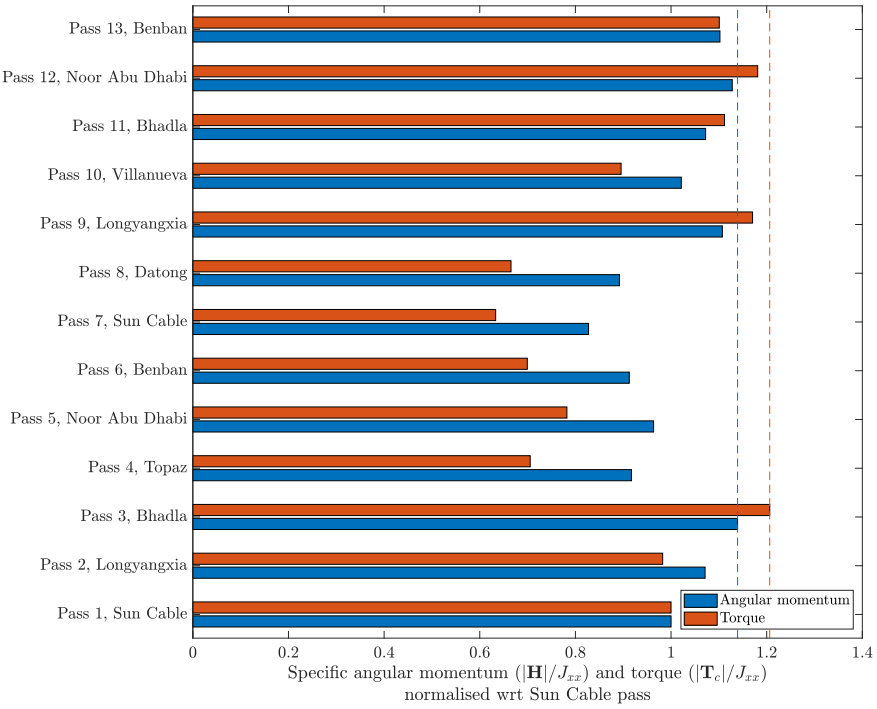

Fig. 15. Maximum specific angular momentum ($|\mathbf{H}|/J_{xx}$) and specific torque ($|\mathbf{T}|/J_{xx}$) for each scheduled pass, normalised with respect to the first Sun Cable pass.

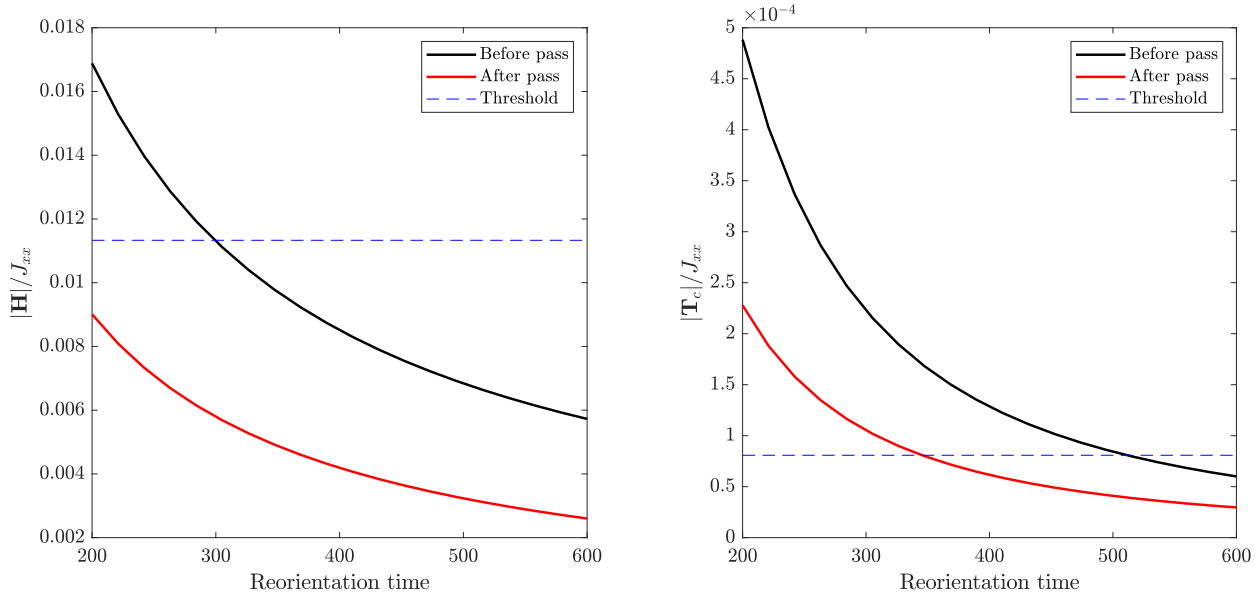

Fig. 16. Specific angular momentum and torque as a function of the reorientation time for the first Sun Cable pass.

attainable with the largest control effort being required during the third ground tracking phase over the Bhadla SPF. Table 6 shows the selected reorientation times for all the passes in one cycle. The reorientation time before the first pass (Sun Cable) and after the last pass (Benban) is slightly larger, due to the different reference frame targeted in these phases, i.e., the angular momentum dumping reference frame.

Note that during the the idle phase the angular momentum and torque requirements do not exceed the peak values for Bhadla, since the orbital mean motion is significantly lower than the angular velocity during a pass and the angular acceleration is approximately zero.

4.4. Actuator selection and reflector size

The attitude control system must provide the necessary angular momentum and torques to steer the mirror during each operational phase. The required angular momentum and torque scale with the inertia of the reflector, i.e., with

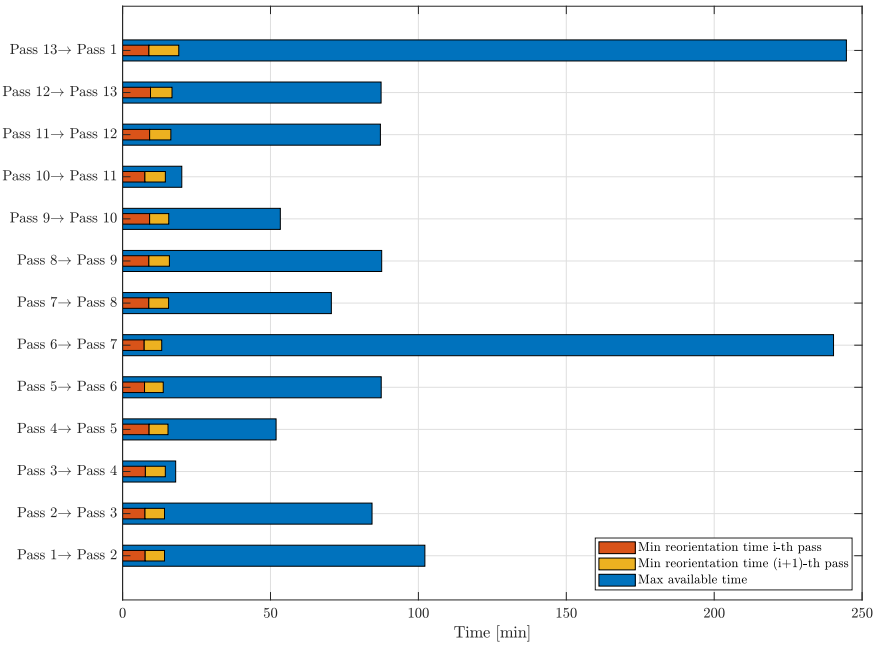

Fig. 17. Selected reorientation times (orange and yellow bars) compared with the maximum time between passes (blue bars) for each scheduled pass.

the fourth power of the reflector size, suggesting that the mass of the actuator will significantly increase for larger structures. In addition, high precision is required during the tracking phase, in order to minimize stray light. For these reasons, and based on a previous trade-off study of attitude control actuators for large planar structures (Viale and McInnes, 2023), CMGs are selected for this application. A CMG generates torque by gimballing a rotor rotating at high speed; since the gimbal rotation rate is usually several order of magnitude smaller than the flywheel angular velocity, a CMG can produce a large amount of torque with a relatively small amount of power. CMGs are classified based on the rotation rate of the flywheel (constant speed or variable speed) and on the degrees of freedoms of the gimbals (single-gimbal or double gimbal). For this this application, constant-speed, single gimbal CMGs are selected. To guarantee three-axis control, large momentum capability and redundancy, a cluster of 4 CMGs in a pyramid configuration mounted on the back of the reflector is selected, as represented in Fig. 18. Such a pyramid configuration has been proven effective in several applications, including control of the ISS.

Let $m_{\text{cmg}}, r_{\text{cmg}}$ and ω_{cmg} be the mass, radius and angular velocity of the rotor, respectively and let δ_i be the gimbal angle such that when $\delta_1 = \delta_2 = \delta_3 = \delta_4 = 0$ the net angular momentum generated by the CMGs is zero. Furthermore, let γ be the angle between the gimbal axis and the reflector normal. Following (Wie et al., 2002) a skew angle $\gamma = 53.13°$ is selected.

For a disk-shaped rotor, the angular momentum H_{cmg} produced by each CMG can be written as:

$$H_{\text{cmg}} = \frac{1}{2} m_{\text{cmg}} r_{\text{cmg}}^2 \omega_{\text{cmg}} \tag{56}$$

such that the total angular momentum vector produced by the CMGs with respect to the RRF is given by:

$$\mathbf{H}_{cmg,tot} = H_{\text{cmg}} \left(\begin{bmatrix} -\cos\gamma \sin\delta_1 \\ \cos\delta_1 \\ \sin\gamma \sin\delta_1 \end{bmatrix} + \begin{bmatrix} -\cos\delta_2 \\ -\cos\gamma \sin\delta_2 \\ \sin\gamma \sin\delta_2 \end{bmatrix} + \begin{bmatrix} \cos\gamma \sin\delta_3 \\ -\cos\delta_3 \\ \sin\gamma \sin\delta_3 \end{bmatrix} + \begin{bmatrix} \cos\delta_4 \\ \cos\gamma \sin\delta_4 \\ \sin\gamma \sin\delta_4 \end{bmatrix} \right) \tag{57}$$

In principle, large angular momenta can be produced by arbitrarily increasing the angular velocity of the rotor. In practice, the angular velocity of the rotor is limited by the stress induced by the centrifugal-induced forces. For a disk-shaped rotor, the maximum stress τ_{cmg} can be expressed as Long and Zhiping (2009):

$$\tau_{\text{cmg}} = \frac{3+\nu}{8} \rho_{\text{cmg}} \omega_{\text{cmg}}^2 r_{\text{cmg}}^2 \tag{58}$$

where ν and ρ_{cmg} are the Poisson coefficient and density of the rotor, respectively. By solving Eq. (58) for ω_{cmg} and substituting it into Eq. (56) the rotor angular momentum can then be written as a function of its radius, mass and material properties:

$$H_{\text{cmg}} = m_{\text{cmg}} r_{\text{cmg}} \sqrt{\frac{2}{3+\nu}} \sqrt{\frac{\tau_{\text{cmg}}}{\rho_{\text{cmg}}}} \tag{59}$$

Material with larger specific strength $\tau_{\text{cmg}}/\rho_{\text{cmg}}$ can therefore offer a larger angular momentum for a given rotor mass and radius. The mass of the rotor m_{cmg} can be found by constraining the CMG areal density, i.e., by defining the parameter:

Table 6
Scheduled pass timestamps with reorientation and idle duration (all times are in minutes) and $t = 0$ set at the beginning of the first Sun Cable tracking phase.

Pass	SPF	Reor. Δt	Tracking			Reor. Δt	Idle Δt
			t_{start}	Δt	t_{end}		
		[min]	[min]	[min]	[min]	[min]	[min]
1	Sun Cable	8.5	0.0	16.1	16.1	5.8	90.9
2	Longyangxia	5.5	118.3	16.0	134.3	5.8	73.0
3	Bhadla	5.6	218.6	16.2	234.8	5.9	6.4
4	Topaz	5.7	252.7	15.9	268.6	5.4	41.1
5	Noor Abu Dhabi	5.4	320.5	15.6	336.1	5.7	76.4
6	Benban	5.4	423.5	15.1	438.6	5.7	229.7
7	Sun Cable	5.0	678.9	16.0	695.0	5.3	59.6
8	Datong	5.7	765.5	15.4	780.9	5.3	76.4
9	Longyangxia	5.9	868.5	16.3	884.8	5.5	42.3
10	Villanueva	5.5	938.1	16.0	954.1	5.8	8.4
11	Bhadla	5.9	974.1	16.3	990.4	5.5	75.6
12	Noor Abu Dhabi	6.1	1077.5	15.5	1093.0	5.7	75.5
13	Benban	6.2	1180.4	14.9	1195.3	8.1	228.0

$$\sigma_{\text{cmg}} = \frac{4(m_{\text{cmg}} + m_g)}{A_r} \tag{60}$$

where the numerator is the sum of the rotor mass and gimbal mass (m_g) and the denominator is the area of the reflector $A_r = 3\sqrt{3}l^2/2$. As in Ref. (Hedgepeth et al., 1981), it is assumed here that the required gimbal is equal to the rotor mass. Thus, the CMG rotor mass can be written as:

$$m_{\text{cmg}} = \frac{3\sqrt{3}}{16}\sigma_{\text{cmg}} l^2 \tag{61}$$

The total angular momentum supplied by the CMG cluster must be equal, with an adequate safety margin, to the maximum angular momentum to be supplied during each cycle, which was found in Section 4.3. By conservatively assuming that the peak angular momentum must be supplied about the reflector z axis (i.e., taking $\delta_1 = \delta_2 = \delta_3 = \delta_4 = 0$), the required angular momentum per CMG can be therefore expressed as:

$$H_{\text{r,required}} = \frac{k_h}{4\sin\gamma}\left(\frac{H_r}{J_{xx}}\right)_{\max} J_{xx} \tag{62}$$

where a coefficient $k_h > 1$ has been included and, from Section 4.3, $(H_r/J_{xx})_{\max} = 1.13 \times 10^{-2}\text{s}^{-1}$. Then, substituting the rotor mass (Eq. (61))) into Eq. (59) and then equating Eqs. (59) and (62) and solving for the reflector side finally yields:

$$l = \sqrt{\frac{12}{5k_h}\sqrt{\frac{2}{3+\nu}}\frac{\sin\gamma}{(H/J_{xx})_{\max}}\frac{\sigma_{\text{cmg}}}{\sigma_{\text{str}}}\sqrt{\frac{\tau_{\text{cmg}}}{\rho_{\text{cmg}}}}r_{\text{cmg}}} \tag{63}$$

For a given CMG radius r_w Eqs. (63) and (61) can then be used to find the maximum reflector size and rotor mass, as a function of the rotor material. This is shown in Fig. 19 for a CMG mass density $\sigma_{\text{cmg}} = 6\ \text{gm}^{-2}$ and for a different set of rotor materials: steel ($\rho_{\text{cmg}} = 7800\ \text{kgm}^{-3}$, $\tau_{\text{cmg}} = 18000$ MPa), titanium ($\rho_{\text{cmg}} = 4500\ \text{kgm}^{-3}$, $\tau_{\text{cmg}} =$

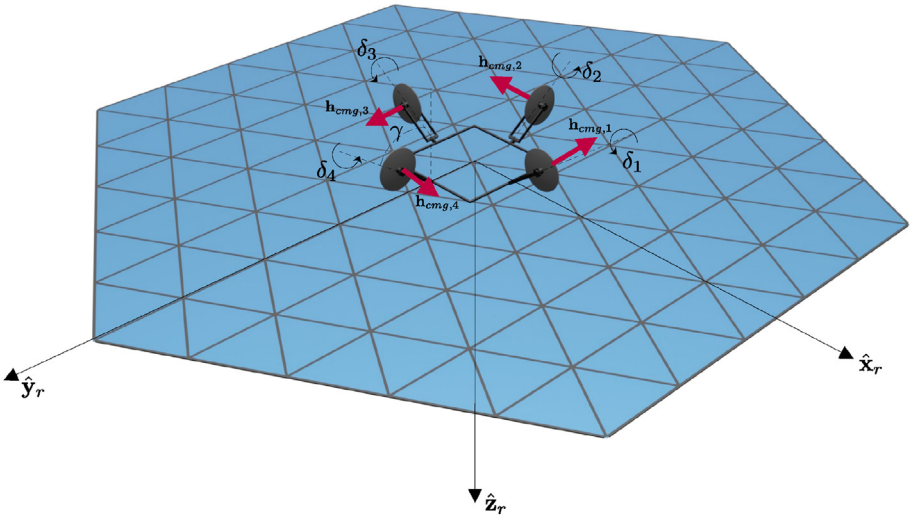

Fig. 18. Control moment gyros mounted on the back of the reflector (not to scale).

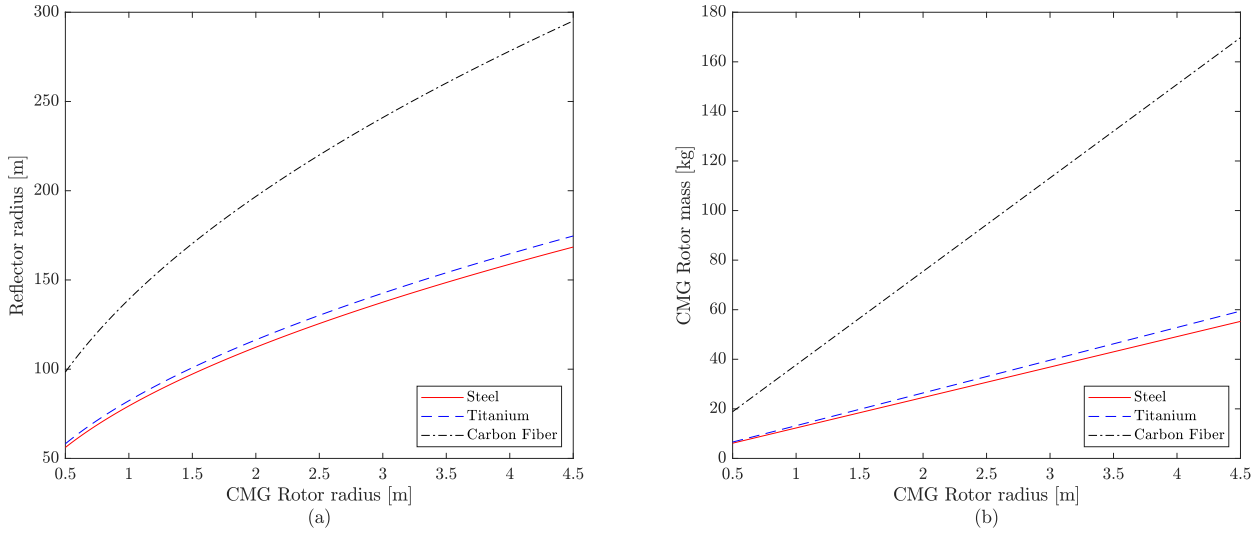

Fig. 19. Maximum reflector size (hexagon side) and rotor mass as a function of the rotor radius, for different rotor materials, assuming a CMG mass density $\sigma_{\text{cmg}} = 6\ \text{gm}^{-2}$.

600 MPa) and carbon fiber ($\rho_{\text{cmg}} = 1664\ \text{kgm}^{-3}$, $\tau_{\text{cmg}} = 3620$ MPa) (Long and Zhiping, 2009). Moreover, a safety factor of 4 on the yield stress is taken and $k_h = 3$. The value of k_h was selected after several attempts to ensure that the CMGs do not encounter singularities during a full 24 h cycle. As expected, a larger rotor radius or specific strength $\tau_{\text{cmg}}/\rho_{\text{cmg}}$ increases the CMG angular momentum (as dictated by Eq. (59)), thus allowing to control larger reflectors. Note however that a larger specific strength also implies a larger rotor mass.

Assuming that the CMGs are installed at distance $4r_{\text{cmg}}$ from the reflector centre-of-mass, their inertia with respect the reflector z-axis is two orders of magnitude smaller than J_{zz}, and analogous considerations can be made for the inertias with respect to the other two in-plane directions. Hence, as anticipated in Section 4.3, the contribution of the CMGs can be neglected in the reflector inertia tensor $\mathbf{J}$.

If the CMG cluster is launched from Earth, a major constraint in the rotor dimension is given by the size of the fairing. Then, a stack of carbon fiber CMGs with a diameter of 6.5 m would fit with sufficient margin inside a SpaceX Starship fairing, allowing to control a reflector with a side of 250 m, which is selected as the baseline reflector size for this preliminary design. The properties of the CMG cluster under these assumptions are listed in Table 2. Fig. 20 shows the variation of the reflector side for different CMG areal densities and reflector areal densities, keeping a constant 3.25 m rotor radius and adopting carbon fiber. In principle reflectors up to 350 m in side could be controlled if the areal density is reduced to 5 gm^{-2}.

Then, given the final selected reflector size, the minimum number of reflectors required to cover an equivalent reflective area of (at least) a 1 km disk can be calculated:

$$\left\lceil \frac{\pi(500\ \text{m})^2}{(3\sqrt{3}l^2)/2} \right\rceil = 5 \tag{64}$$

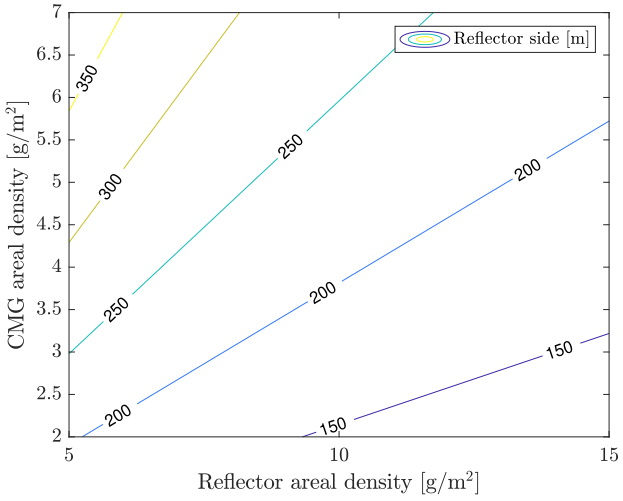

Fig. 20. Variation of the reflector side as a function of the CMG areal density σ_{cmg} and the structure areal density σ_{str}.

where $\lceil \cdot \rceil$ denotes the ceiling function. The effective equivalent radius of the assembly of 5 reflectors is approximately 508 m.

4.5. Control law

The control torque input signal is calculated here using a PD control logic with feedforward compensation, in the form (Jia and Xu, 2005)

$$\mathbf{T}_c = -\mathbf{K}_q\mathbf{e} - \mathbf{K}_\omega\boldsymbol{\omega}_e + \boldsymbol{\omega}_r \times J\boldsymbol{\omega}_r + J\dot{\boldsymbol{\omega}}_t \tag{65}$$

where $\mathbf{K}_q$ and $\mathbf{K}_\omega$ are the controller gains. The attitude error vector $\mathbf{e}$ is the vectorial part of the attitude quaternion error $\mathbf{q}_e$, defined as:

$$\mathbf{q}_e = \bar{\mathbf{q}}_t \otimes \mathbf{q}_r \tag{66}$$

such that $\mathbf{q}_e = (q_{e0}, \mathbf{e})$. The angular velocity error vector $\boldsymbol{\omega}_e$ is given by the difference between the current angular velocity vector of the reflector $\boldsymbol{\omega}_r$ and the target angular velocity vector $\boldsymbol{\omega}_t$, i.e.,:

$$\boldsymbol{\omega}_e = \boldsymbol{\omega}_r - \boldsymbol{\omega}_t \tag{67}$$

The last two terms appearing in Eq. (65) can be interpreted as the required torque to be applied to the reflector if the body frame coincides with the target frame. These terms guarantee asymptotic stability of the closed-loop system (Jia and Xu, 2005). The target angular velocity $\boldsymbol{\omega}_t$ and angular acceleration $\dot{\boldsymbol{\omega}}_t$ are calculated based on the current reflector operational phase, as discussed in Section 4.2.

Following Ref. (Wie et al., 2002), the control gains $\mathbf{K}_q$ and $\mathbf{K}_\omega$ are selected as $\mathbf{K}_q = 2k\mathbf{J}$ and $\mathbf{K}_\omega = c\mathbf{J}$ where k and c are positive constants that can be determined based on the desired bandwidth ω_n and damping ratio ξ of the control system, i.e., $k = \omega_n^2$ and $c = 2\xi\omega_n$. Following Ref. (Wie et al., 2002), these parameter are here set as $\xi = 0.707$ and 3 rad s^{-1}.

Given the control torque input $\mathbf{T}_c$ the required CMG angular momentum rate is, from Eq. (52):

$$\dot{\mathbf{H}}_{\text{cmg}} = -\mathbf{T}_c - \boldsymbol{\omega}_r \times \mathbf{H}_{\text{cmg}} \tag{68}$$

Following (Wie et al., 2002), a relationship between the angular momentum rate $\dot{\mathbf{H}}_{\text{cmg}}$ and the gimbal rates $\dot{\boldsymbol{\delta}}$ can then be found by differentiating Eq. (57):

$$\dot{\mathbf{H}}_{\text{cmg}} = H_{\text{cmg}} A \dot{\boldsymbol{\delta}} \tag{69}$$

where the matrix A is given by:

$$A = \begin{bmatrix} \cos\gamma\cos\delta_1 & \sin\delta_2 & \cos\gamma\cos\delta_3 & -\sin\delta_4 \\ -\sin\delta_1 & -\cos\gamma\cos\delta_2 & \sin\delta_3 & \cos\gamma\cos\delta_4 \\ \sin\gamma\cos\delta_1 & \sin\gamma\cos\delta_2 & \sin\gamma\cos\delta_3 & \sin\gamma\cos\delta_4 \end{bmatrix} \tag{70}$$

with $\dot{\boldsymbol{\delta}} = [\dot{\delta}_1, \dot{\delta}_2, \dot{\delta}_3, \dot{\delta}_4]$. Then, the required gimbal rates can be found by inverting Eq. (69) using the pseudoinverse matrix (Wie et al., 2002), which returns the minimum-norm solution:

$$\dot{\boldsymbol{\delta}} = \frac{1}{H_{\text{cmg}}} A^* \mathbf{H}_{\text{cmg}} \tag{71}$$

where the pseudoinverse matrix A^* is given by Wie et al. (2002)

$$A^* = A^T (A A^T)^{-1} \tag{72}$$

Usually, a variant of the pseudoinverse is used to ensure that $\det(AA_T) \neq 0$ for any value of the gimabal angle vector $\boldsymbol{\delta}$ (Wie et al., 2002). In this case, however, a singularity encounter during the tracking phase should be avoided as it would lead to a loss of tracking precision. For this reason, the CMGs were sized with a pre-multiplication factor k_h large enough to guarantee that the gimbal angles remain small and no singularity is encountered during a sidereal day cycle. Clearly, this design is not optimal, however, it is sufficient to provide preliminary attitude control insights for this analysis.

4.6. Closed-loop feedback results

Figs. 21 and 22 show the commanded gimbal rates, gimbal angles, control torque and velocity of the light track on the ground for the first pass Sun Cable pass and the Bhadhla pass. Required gimbal rates are on the order of 0.1 deg/s with a peak of approximately 0.4 deg/s which is, for reference, approximately one order of magnitude smaller then the peak gimbal rates on the CMGs mounted on the ISS. As expected, the peak gimbal rates are associated with larger torques. Note that, during the reorientation phase, the peak torque is equal to the threshold torque calculated for the Bhadla pass, corresponding to $T = 1704$ Nm (this is represented with a red dashed line in Fig. 21(c): this torque value is also reached at the first maximum during the Bhadla tracking phase. The components of the torque vector when the torque magnitude is maximum during the Bhadla tracking are: $T_x = 736.6$ Nm, $T_y = -512.8$ Nm, $T_z = 1448.8$ Nm. The highest component of the torque vector is therefore in the out-of-plane direction $\hat{\mathbf{z}}_r$.

Figs. 21 and 22 show the trajectory of the light track on the ground during the reorientation phases for the first and third passes (these are derived using the method described in Appendix A). More precisely, this is the velocity of the centre of the elliptical light image as it moves on the ground. Clearly, the shape of this trajectory depends on the allocated reorientation time and the definition of the TRF during the reorientation phase. Note that such trajectories span over several countries (although illuminated areas are mostly on water for the Sun Cable case) before reaching the SPF target and after leaving it. In any case, the velocity of the light track is on the order of kilometres per second before reaching the target, as shown in Figs. 21(d) and 22(d). Hence such stray light will only last a few seconds (depending on the current size of the ellipse on the ground) across the interested regions that are on the night side when the light is crossing.

In principle, such a light track could be minimized or even totally removed by adequately changing the reflector attitude during the reorientation phases such that no sunlight is reflected onto the Earth during the reorientation manoeuvre. However, should future SPF be added to the scheduled passes, rapid retargeting may be required, such that the reflector is steered between two SPF without reaching the idle phase, thus inevitably redirecting sunlight to unwanted locations. It is expected that the velocity of the light track will be on the order of kilometers per second in this case as well. Figs. 21(f) and 22(f) show the displacement between the centre of the light cone and the centre of the SPF during the tracking phase. It is apparent that the error is below 10 m for most of the tracking phase,

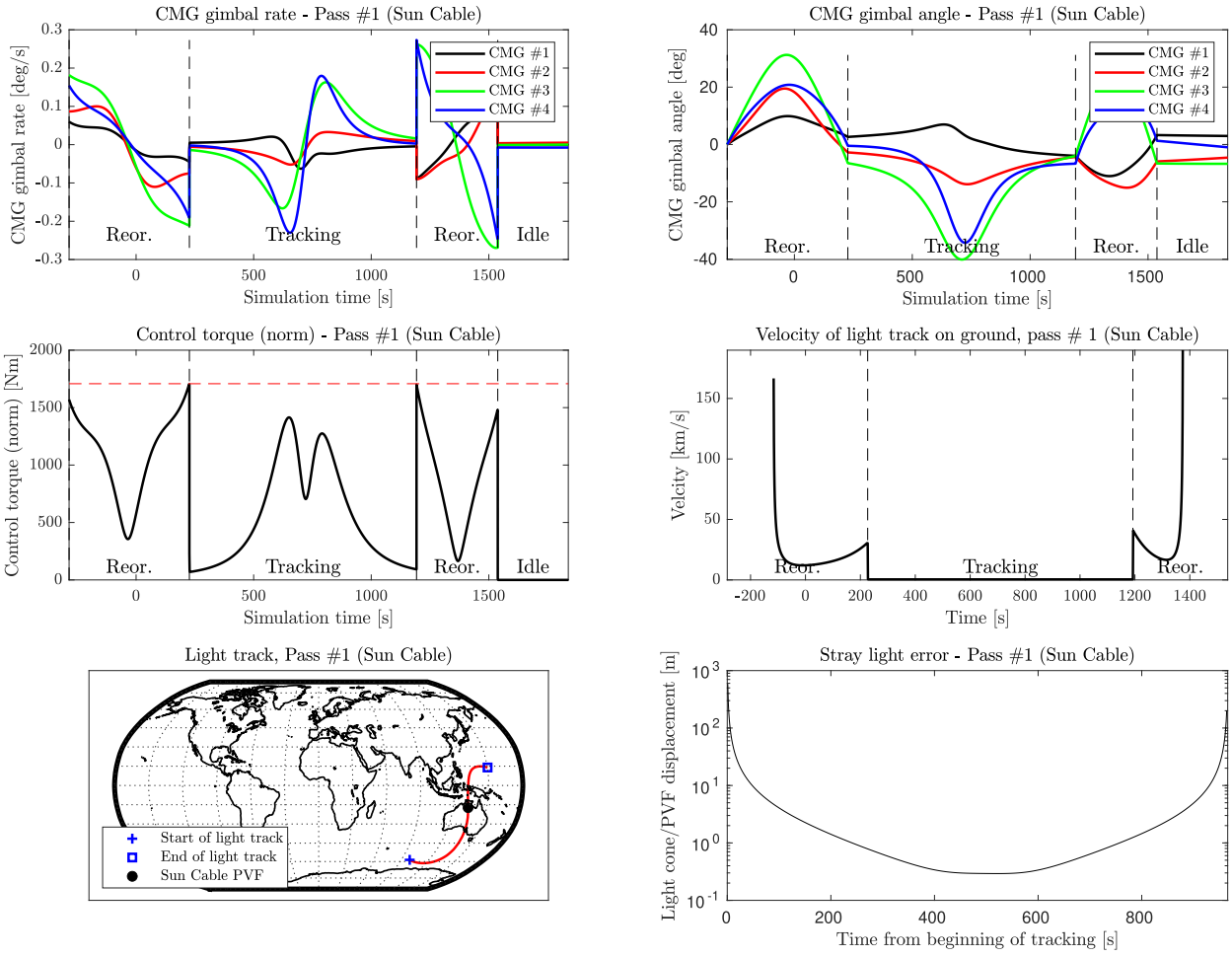

Fig. 21. Gimbal rates, gimbal angles, control torque, velocity of the light track on the ground, light track and displacement between reflected light cone and SPF centre for the first pass (Sun Cable SPF).

although this parameter may change with higher fidelity models.

Fig. 23 shows the power required by the torque motors to drive the gimbals. The peak power is below 10 W and this can be easily supplied by a small solar array mounted on the reflector. However, during the idle phase and reorientation phases, the reflector's effective area facing the Sun is small, thus reducing the available power. Hence battery power is required to ensure operation of the CMGs during each phase. A conservative estimate of the required battery capacity can be made by multiplying the peak power by the maximum time spent by the reflector in idle mode. This leads to approximately 38 Wh of battery capacity.

4.7. Angular momentum dumping

If the manoeuvre was ideally symmetric (i.e., the angular velocity of the reflector is the same at the beginning and at the end of the tracking phase) and no external perturbations were considered, there would be no net change in the CMG angles between the beginning and the end of each tracking manoeuvre. Furthermore, the net angular momentum produced by the CMG cluster will increase over time to counteract the gravity gradient torque. Fig. 24 shows the residual CMG angular momentum at the end of each tracking phase. At the end of pass 13, approximately 1×10^5 N m s are stored within the CMG assembly, which is the same order of magnitude as the angular momentum capacity of each individual CMG. If this residual angular momentum is not removed, it is expected that the CMGs will encounter internal singularities at subsequent cycles, possibly reducing the tracking precision and therefore the energy delivered to the SPF in case the singularity is encountered during a ground tracking phase. To avoid this, an angular momentum dumping phase is included in the 24 h cycle. The idea is to exploit the 230 min between the end of the last pass and the beginning of a new cycle (see Table 6) to perform an actuator desaturation manoeuvre and thus reduce the gimbal angles to zero. It is proposed to exploit solar radiation pressure to generate the required torques to keep the reflector face-on to the Sun. In particular the SRP torque must counteract the torque produced by the CMGs as their gimbal angles are reduced to zero and also counteract the external torques.

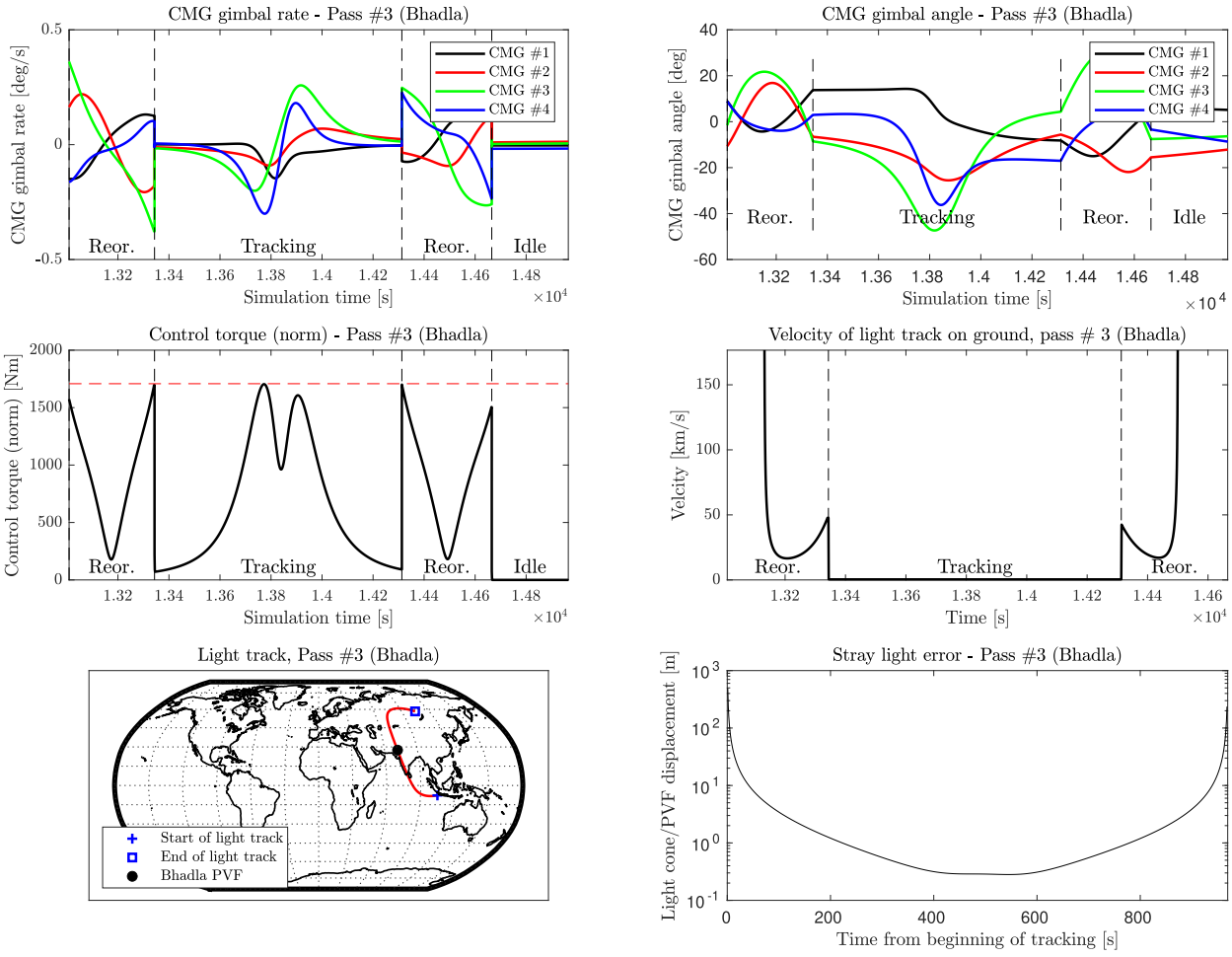

Fig. 22. Gimbal rates, gimbal angles, control torque, velocity of the light track on the ground, light track and displacement between reflected light cone and SPF centre for the third pass (Bhadla SPF).

4.7.1. Required desaturation torques

The torques produced by the CMG during the desaturation phase are calculated assuming that the rotors are gimballed with constant angular velocity, such that the gimbal angles are reduced to zero by the end of the angular momentum dumping phase. Assuming the total time available for the manoeuvre is 90% of the time between the end of pass 13 and the beginning pass 1, then the required gimbal rates for the CMGs are: $\dot{\delta}_1 = -2.6\times\ 10^{-3}$ deg /s, $\dot{\delta}_2 = 7.7\times 10^{-4}$ deg /s, $\dot{\delta}_3 = 1.5\times 10^{-3}$ deg /s, $\dot{\delta}_4 = 4.3\times 10^{-4}$ deg /s. Fig. 25 shows the overall torque produced by the CMGs summed to the gravity gradient torque. The SRP desaturation actuators must therefore be sized based on the peak torques required during this phase. Multiplying those by a factor 1.2, the required torques during desaturation are 11.7 Nm, 10.6 Nm and 1.3 Nm about the x, y and z axis respectively.

4.7.2. Variable reflectivity coatings

In order to generate variable torques via SRP about the reflector in-plane axes, variable reflectivity surfaces can be used. The idea is to use electro-active materials on a number of triangular tiles that can change their reflectivity when a potential is applied (Borggrafe et al., 2014). By modulating the electric signal, the SRP force acting on the triangular tile can therefore be changed. The number of triangular tiles covered by variable reflectivity coating can then be calculated based on the peak torque required about each axis.

Consider, for example, a triangular module with center-of-mass located at a distance d_x with respect to the reflector x-axis. Then the total torque generated by that triangle with respect to the x axis is Borggrafe et al. (2014):

$$T_x = p_{srp}(1+\eta)\cos\left(\frac{\psi}{2}\right)^2 A_{\text{triang}} d_x \tag{73}$$

where A_{triang} is the area of each triangular element, η is the reflectivity coefficient and $\psi/2$ is the angle between the element normal and the Sun light direction. Since the reflector is facing the Sun $\psi/2 = 0$ deg. Similarly, the torque about the y-axis can be expressed as

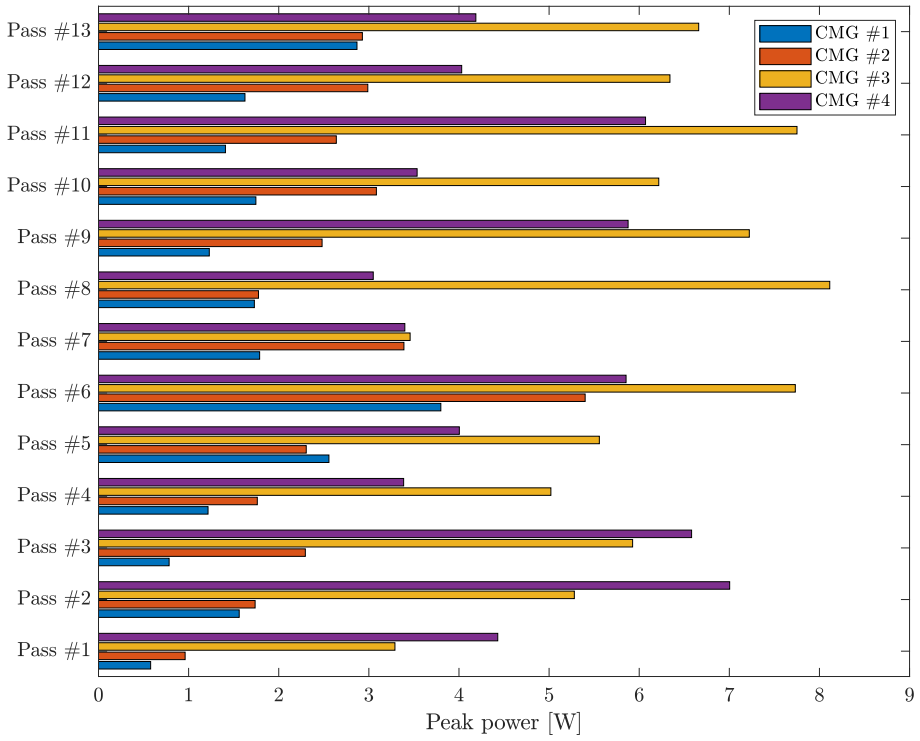

Fig. 23. Peak gimbal power per pass.

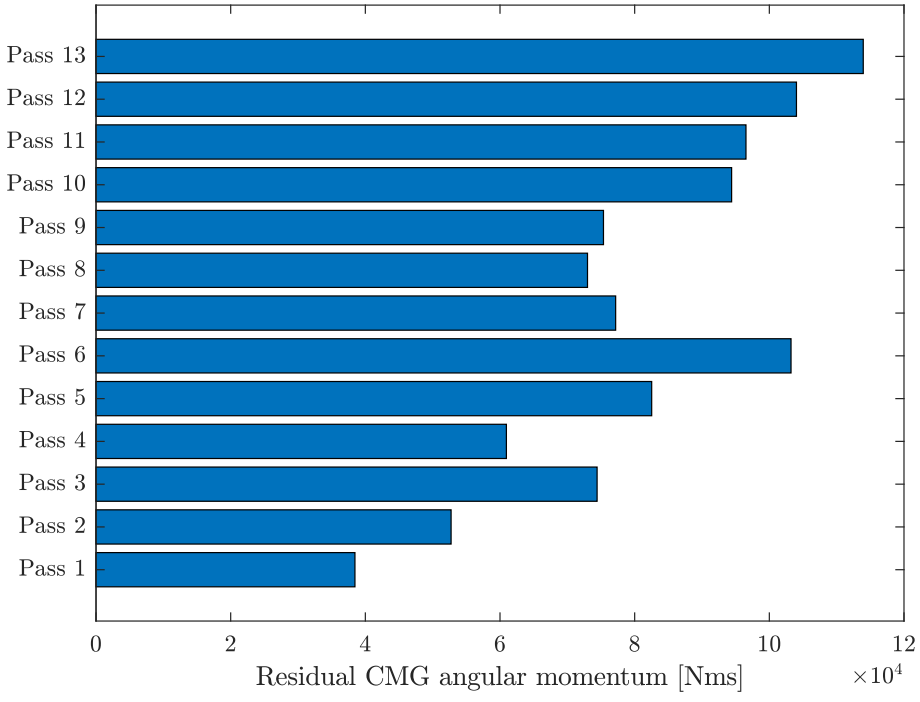

Fig. 24. Residual CMG angular momentum at the end of each pass.

$$T_y = p_{srp}(1+\eta)\cos\left(\frac{\psi}{2}\right)^2 A_{\text{triang}} d_y \tag{74}$$

where d_y is now the distance between the triangle center-of-mass and the reflector y-axis.

To generate a torque about the z axis, a pair of triangular modules at the reflector edge is tilted, as shown in Fig. 26. In this case, the torque generated about the z axis by each tile can be expressed as:

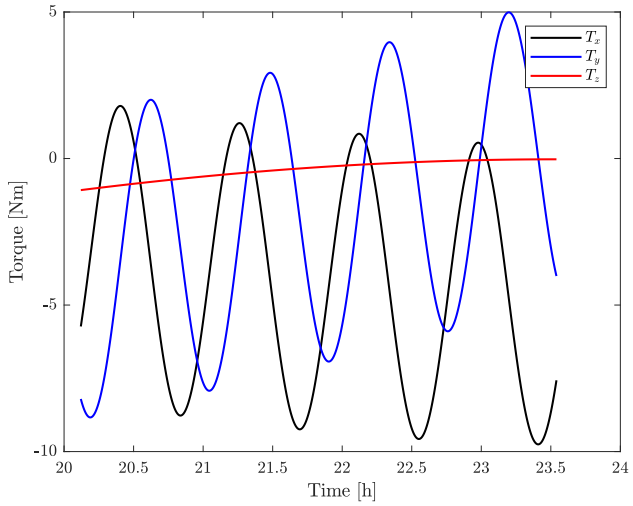

Fig. 25. Combined CMG and gravity gradient torque during desaturation phase.

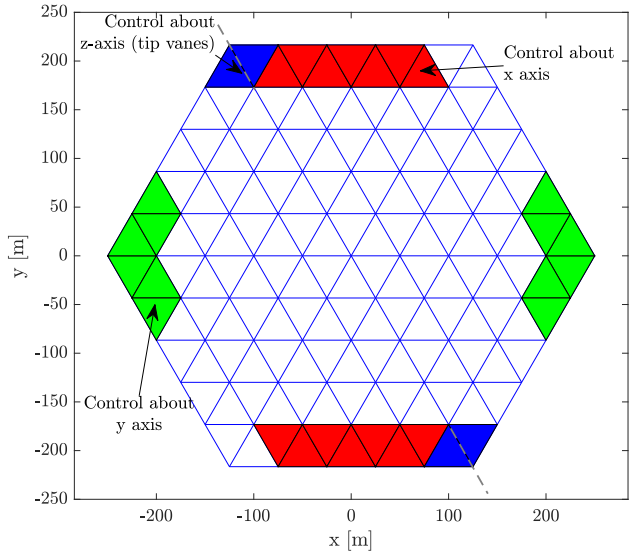

Fig. 26. Reflector tiles with variable reflectivity out-of-plane rotation control for CMG desaturation. The tiles for control about the z axis can be rotates about the dashed axis.

$$T_z = p_{srp}(1+\eta)\cos\left(\frac{\psi}{2}\right)^2 \sin\left(\frac{\psi}{2}\right) A_{\text{triang}} d_0 \tag{75}$$

where d_0 is the distance between the centre of mass of the the triangle with respect to the centre of the reflector. In this case the torque can be varied by changing the rotation angle ψ while keeping the reflectivity constant. The maximum torque T_z that can be generated is associated to the angle $\psi/2$ that maximizes Eq. (75), i.e., for $\psi/2 \approx 35.2$ deg.

Fig. 26 shows the triangles that are needed to generate the minimum required torques discussed in the previous section. In particular, 14 variable reflectivity triangles are required to generate sufficient desaturation torque about the x axis, 12 triangles for torques about the y axis and 4 tiles for torques about the z axis. Note that the tiles with variable reflectivity come in symmetric pairs, to ensure that the torques can be generated in both directions about each axis.

5. Reflector configuration

As discussed earlier, the orbit of the reflector governs the image size of the solar disk on the Earth. The image size is approximately the solar angular diameter at the Earth, which is 0.0093 radians, scaled by the orbit altitude. However, the sharpness of the image depends on the size of reflector in the given orbit (Buckingham and Watson, 1968). The illumination achieved is proportional to the ratio of the reflector size to the image size. To achieve the same illumination as the incident light, the reflector should be of the same size as the reflected image of the Sun on the Earth for the given altitude, which is in the order of kilometers (Buckingham and Watson, 1968). Such a large area can be realized using an assemblage of several small identical areas (Billman et al., 1977). Such an approach of splitting a large area reflector into small reflectors reduces the required size of the individual reflectors. This also facilitates the construction of a reflector of the required size using standardized manufacturing and assembly processes. A reflecting surface is formed by an ultrathin metallic reflective coating on a thin polyimide or polyester substrate film stretched over the structure. The deployable configurations for reflectors of such scale are complicated and must withstand the launch loads, which demands a stiffer structure. However, an on-orbit manufacturing and assembly process facilitates the economically feasible realisation of such a large-scale structure. As the loads experienced in the microgravity environment are much less than the launch loads, the structures produced using on-orbit facilities can be larger and lighter (Hoyt, 2013; Joyce et al., 2017). Also, defects due to transportation and packaging are avoided. The structural design for the proposed reflector is conceived based on these facts. The structural details and strategies to manufacture the proposed reflector are discussed here.

5.1. Structural design

The hexagonal shaped reflector based on triangulation is conceptualised as discussed in earlier studies by the authors (Çelik et al., 2022). The diagonals are the main load carrying components, so they are strengthened and are connected through a central joint. The size of the individual triangles governs the number of levels required for the given size of hexagon, as shown in Fig. 27. The maximum size of the hexagon which can be controlled by the employed CMGs is with a side of 250 m, as suggested in Section 4.4.

The typical reflecting film used in such applications has an areal density in the range of 3–20 gm^{-2} (Trofimov and Ovchinnikov, 2018). Assuming an ideal gossamer structure

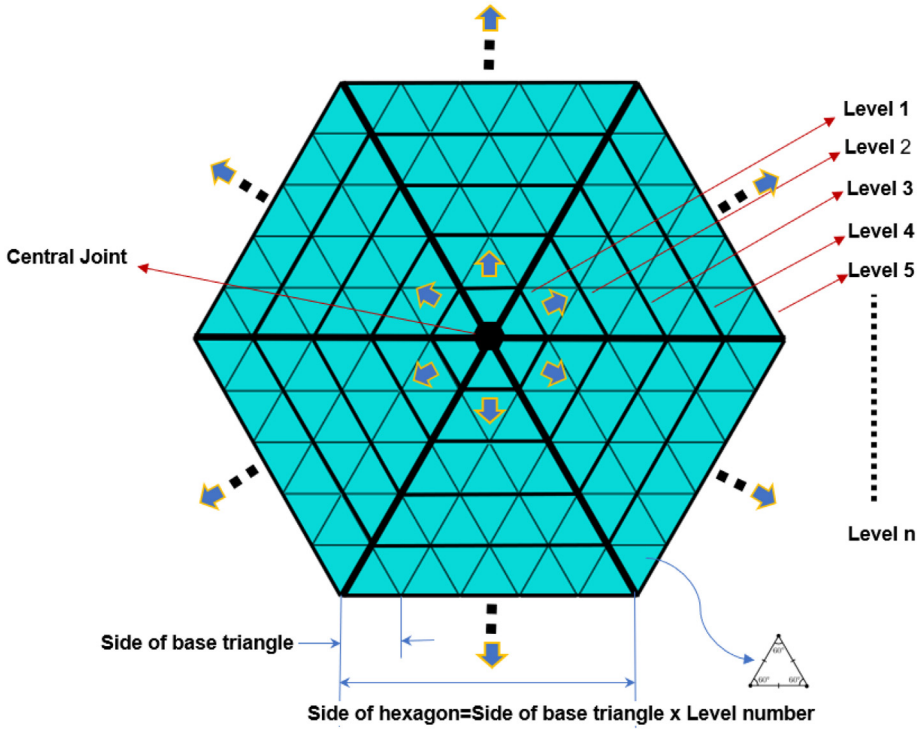

Fig. 27. The conceptual hexagonal reflector constructed using a number of triangular areas (adapted from Çelik et al., 2022).

that has the same areal density as of the member to be carried; the variation of structural mass per unit length required to achieve such a structure is plotted in Fig. 28.

According to the literature, the lowest achievable mass per unit length for a space beam employed in such applications is approximately 70 gm^{-1} (Mikulas et al., 2006). The side of the hexagon should also be divisible by the side of the triangle. All these conditions prompt the selection of the side of the base triangle as 50 m. The selection is based on the lowest mass density achievable for the support structure by the present-day technology.

From the selection of the side of the triangle, a hexagonal structure with level 5 is designed which is shown in Fig. 29. The trusses are employed along the diagonals of the hexagon. The six trusses are connected at the center through a central joint. The cross bars hold the reflector film. The structural details are given in Fig. 30.

Graphite-epoxy material used in similar applications for space trusses is adopted here, for which the material properties are (Mikulas et al., 1977; Mikulas, 1978; Bush et al., 1980):

$$E_{11} = 131\ \text{GPa}, \quad E_{22} = 10.9\ \text{GPa}, \quad G_{12} = 6.41\ \text{GPa},$$
$$\nu_{12} = 0.32, \quad \rho = 1522\ \text{kgm}^{-3}, \kappa = -0.54 \times 10^{-6}\ \text{K}^{-1}$$

where E is the modulus of elasticity, G is the shear modulus, ν is the Poisson's ratio, ρ is the volumetric density and κ is the coefficient of thermal expansion.

The truss structure along the diagonals of the hexagon is shown in Fig. 31. As the length of the half diagonal of the hexagon is 250 m, the length of the truss is half the diagonal length minus the half span of the joint. As the central joint must comply with the cross section of the truss, the truss cross section dictates the joint dimensions. These distances and dimensions can be easily determined using preliminary geometry, as the cross section of the truss is an equilateral triangle. The length of the bay is the length of the unsupported portion of the longeron. The number of bays is chosen in such a way that the length of the bay will be the same as of the batten length. This will assure the 45° angle between the diagonals and the longerons of the truss. The various dimensions used for the graphite-epoxy tubes in the present hexagonal structure are given in Table 7.

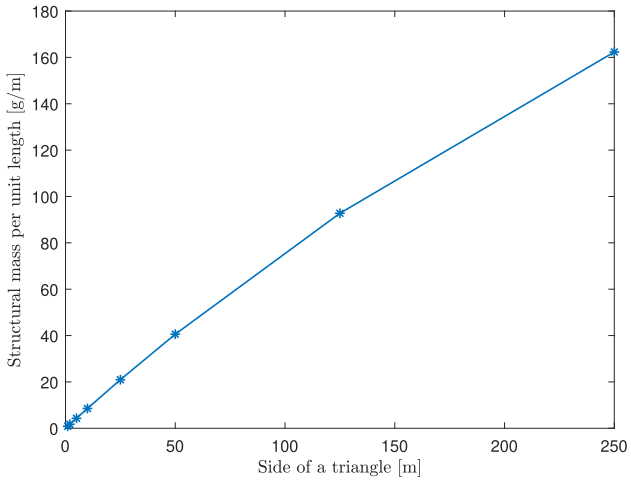

Fig. 28. The structural mass per unit length for the given side of triangle to achieve an ideal structural areal mass density of 3 gm^{-2}.

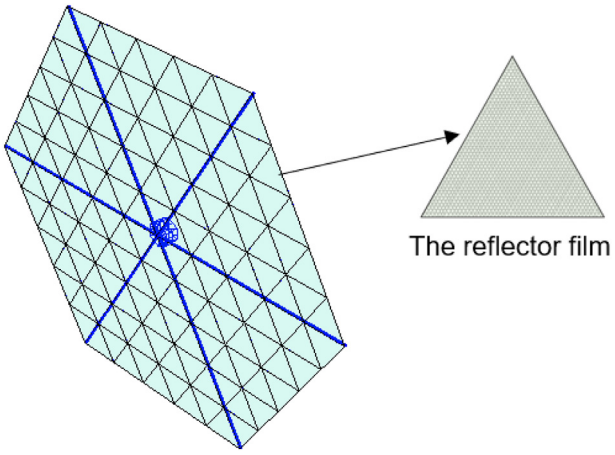

Fig. 29. The proposed design of the reflector.

A 2 μm thick Kapton membrane coated with vapor-deposited aluminum is proposed as a mirror surface. The aluminized Kapton is selected as a reflective material because of its low thermal coefficient of expansion and thermal stability. Kapton also does not show tearing behaviour. Therefore holes in membrane as a result of micrometeoroid impacts will be microscopic in size. Furthermore, Kapton's strength applies to a wide temperature range (−270 °C to + 400 °C) (Ehricke, 1979). Even though films with an areal density as low as 1.53 gm^{-2} are being developed (Gong and Macdonald, 2019; Garner et al., 1999), a much studied aluminized Kapton film with 3 gm^{-2} is used for the present paper.

The triangular film is connected to the structure through connecting ties as shown in Fig. 32. The supporting mesh structure is provided to carry the loads on the film and to keep it in a tensioned state. The tensioning cables are made of 12.5 mm wide and 12.5 μm thick aluminized Kapton HN tape (Fernandez et al., 2018). As the film material and tensioning cables are of the same material, differential thermal expansion will be avoided. The differential expansion arises due to the use of different materials attached together in a temperature field.

A mass table with major contributors is presented in Table 8. Including reasonable masses for other systems,

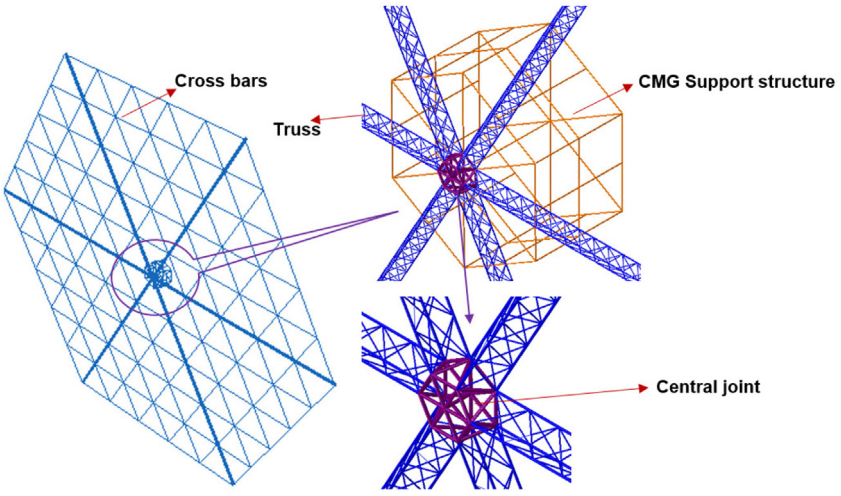

Fig. 30. The reflector structure.

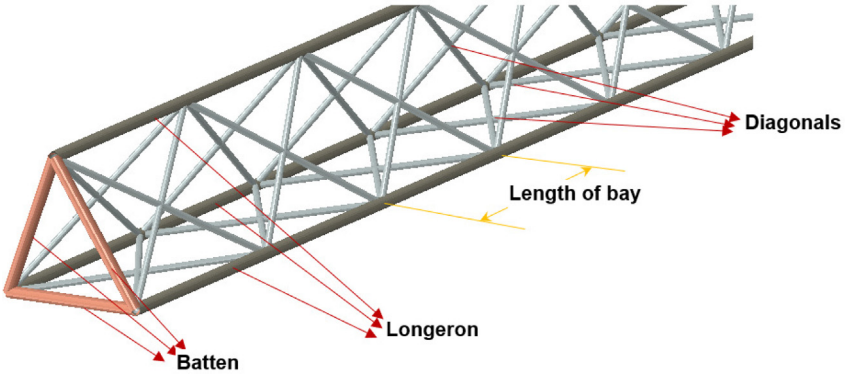

Fig. 31. The members of the truss structure.

Table 7
Structural parameters of the tubes used in the hexagonal reflector.

Member	Length [m]	Diameter [mm]	Thickness [mm]
Batten	2.50	30.48	0.381
Longeron	2.50	30.48	0.381
Diagonals	3.54	10.00	0.381
Central joint	2.50	50.80	1.000
Cross rods	50.00	30.48	0.381
CMG support structure	15.00	50.80	0.500

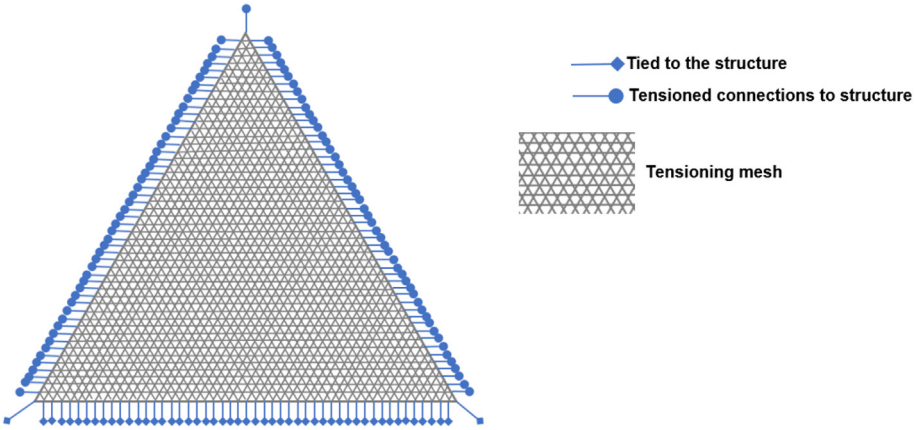

Fig. 32. The triangular reflector film.

Table 8
Mass summary for the solar reflector. Areal density is calculated with the area of a regular hexagon with 250 m side.

Component	Mass [kg]	Areal density [g/m^2]
Structural Components:		
Reflector film	487.14	
Tensioning cables	127.35	
Trusses along diagonals	480.42	
Cross Rods	575.76	
Central Joint	21.00	
CMG Support Structure	54.85	
Total structural mass including reflector film	1746.5	10.8
4 CMGs (including tip vanes torque motors):	1060.00	6.5
Miscellaneous:		
Spring/Joints	50.00	
Communication and data handling system	70.00	
Computers	25.00	
Sensors	50.00	
Batteries and other equipments	50.00	
Total Miscellaneous Mass	245.00	1.5
Total mass of the reflector	3051.5	18.8

the total areal mass density of the reflector is estimated to be 18.8 gm^{-2}. This can in principle be further reduced by using a low mass film with mass density of 1.53 gm^{-2} against the present film with 3 gm^{-2} and new methods of altitude control which will could reduce the CMG mass density to 2 - 4 gm^{-2}, as discussed in Section 7.4.

5.2. Loads on the reflector

Several in-orbit loading conditions are imposed upon the reflector, the most significant of which are discussed here. Stresses developed in the structure due to these loads are evaluated either by analytical solutions or numerical simulations.

5.2.1. Gravity gradient loads

Gravity gradient forces arises because various elements of a structure are at different distances R from the centre of the Earth and hence are subject to forces varying with $1/R^2$. Thus, the net force experienced by the two masses at distance R and $R+\delta R$ is given as Billman et al. (1977):

$$F_{gg} = \frac{dF}{dR}\delta R \tag{76}$$

The stresses due to this force on a rod like structure can be approximated as Billman et al. (1977):

$$\tau_{gg} = \frac{\rho L^2 g_0 R_E^2}{2R^3} \tag{77}$$

where g_0 is the zero altitude acceleration due to gravity, R_E is the Earth's radius, L the length of the structural member, ρ the material density and R the distance between Earth's center and the closest mass element. For the present structure made up of graphite-epoxy material and the longest structural element being 247.835 m in a 884.6 km orbit, the stress in the element is negligible. Also, the permissible yield length for the given altitude to sustain this stress is more than 8 times the dimension of a reflector required for daylight illumination for that orbit, given as solar angular diameter at the Earth (α) multiplied by the orbit altitude (Billman et al., 1977).

5.2.2. Solar radiation pressure loads

Estimation of forces due to the solar radiation pressure plays an important role in the concept of orbiting solar reflectors as these forces can be used for orbit control (see 3.7 for details). In general, these forces will depend on the reflectivity coefficient (η) and absorption coefficient (1-η) of the material, assuming that the total incident light is either reflected or absorbed. The force due to absorption F_{abs} acts along the the direction of the incident radiation, while the force due to reflected radiation F_{ref} acts normal to the surface. These forces are evaluated as Billman et al. (1977):

$$F_{abs} = (1-\eta) I_0 A_r \cos(\psi/2)/c \tag{78}$$

$$F_{ref} = 2\eta I_0 A_r \cos^2(\psi/2)/c \tag{79}$$

where A_r is the irradiated area of the reflector, ψ the angle between irradiation and reflected radiation, I_0 the intensity of irradiation and c is the speed of light. The maximum value of the F_{ref} is experienced by the perfect reflector ($\eta = 1$). The value of the maximum force due to reflection for the present hexagonal reflector with 250 m side, $A_r = 162379.8\ \mathrm{m}^2, \psi$ as 90 deg, $I_0 = 1.4\mathrm{k}\ \mathrm{Wm}^{-2}$ and $c = 3\times10^5\ \mathrm{kms}^{-1}$ is calculated as 0.7578 N. The stresses due to these forces are negligible and does not stress the structure much.

5.2.3. Atmospheric drag loads

This atmospheric drag pressure is estimated using Newtonion flow theory and is given as Hedgepeth et al. (1981):

$$\tau_{ad} = \frac{1}{2}\rho_{\mathrm{atm}} V_o^2 C_N \sin^2 \Upsilon \tag{80}$$

where $\frac{1}{2}\rho_{\mathrm{atm}} V_o^2$ is the dynamic pressure with the orbital velocity V_o and the atmospheric density at that orbit ρ_{atm}, C_N the normal dynamic force coefficient which is taken as 2.5 for the flat surface and Υ the angle of attack taken as $\pi/2$ for normal to the surface. This load increases rapidly with decreasing altitude and is large below 650 km (Hedgepeth et al., 1981). For an altitude of 884.6 km, the estimated value of the pressure due to atmospheric drag is less than $0.8\times10^{-5}\ \mathrm{Nm}^{-2}$ (Hedgepeth et al., 1981). It is noteworthy that the pressure due to atmospheric drag is less than the solar radiation pressure at normal incidence for altitudes greater than 800 km (Hedgepeth et al., 1981).

5.2.4. Orbital motion loads

These forces arise due to the motion of masses which are distant from the centre of gravity of the reflector. This can be thought of as gravity gradient combined with the orbital motion. The maximum value of the stress due to this is given as Hedgepeth et al. (1981):

$$\tau_{om} = 3\omega_o^2 \sigma r \tag{81}$$

where r is the distance from the centre of gravity of structure, ω_o the orbital angular velocity and σ the areal density of the reflector. For the present design with the farthest distance from the centre of gravity being 250 m, orbital angular velocity for 884.6 km orbit being 0.001 rad s^{-1} and areal density of 18.8 gm^{-2}, the value of the computed stress is negligible.

5.2.5. Control loads

The structure is controlled by four CMGs attached to it. These CMGs produce control moments and the stresses exerted on the structure due to them are maximum among all the stresses. As per Section 4.6, the peak values of moments exerted by CMGs along the principal axes are $M_x = 736.6$ Nm, $M_y = 512.8$ Nm and $M_z = 1448.8$ Nm.

As there is no fixed analytical approach, a finite element analysis is carried out to determine the level of stress in the structure subjected to these moments. A numerical model is developed using ABAQUS © finite element package. The submodels of the truss along diagonals, central joint, CMG support structure and cross rods shown in Fig. 30 are developed with line elements of B31 type. The connections between submodels are made with CONN3D2 connector elements. The CMGs are simulated as MASS elements. The model contains a total of 7738 nodes and 13352 elements.

The modelling approach is first verified by comparing the deflection results for a cantilever beam type truss structure with analytical solutions. The truss structure chosen for the validation example is the same truss which runs along the diagonal of the present hexagonal structure. The value of loading chosen is also the maximum of peak moments from the CMG with a factor of safety of 1.5

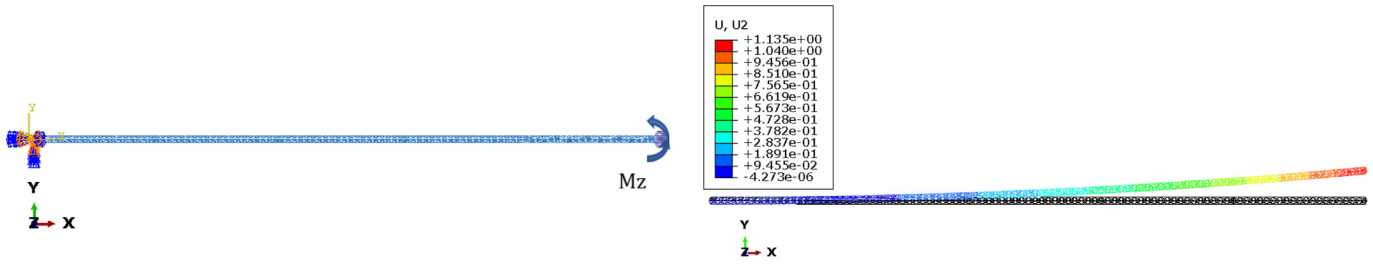

(a) (b)

Fig. 33. The deflection along the y axis (U2) of the cantilever truss in meters, subjected to an end moment $M_z = 545$ Nm.

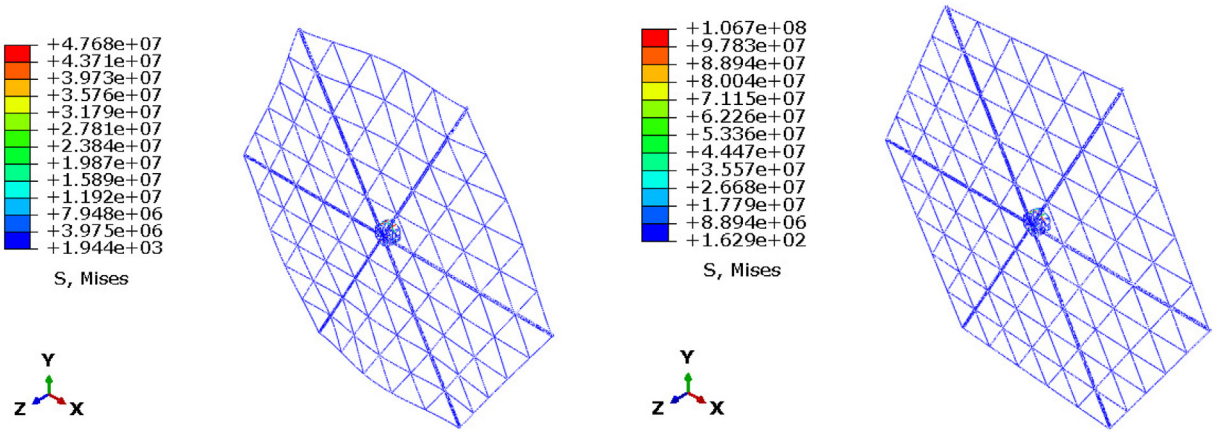

(a) (b)

Fig. 34. Stresses in the reflector structure subjected to a control moment $M_x = 1105$ Nm (a) and $M_z = 2175$ Nm (b).

i.e. $M_z \simeq 545$ Nm. The deflection of cantilever beam subjected to an end moment is given as Popov and Balan (1999):

$$\Delta_y = \frac{M_z L^2}{2E_x I_z} \tag{82}$$

where Δ_y is the deflection along y axis, E_x being the modulus of elasticity along x axis and I_z being the moment of inertia along z axis. The I_z for the truss structure is computed as per the procedure given in Reference (Mikulas, 1978). The analytical solution by Eq. (82) is 1.12 m with the values of E_x and I_z being used as 131 GPa and 1.14×10^{-4} m^4, respectively. The finite element solution shown in Fig. 33b closely matches with the analytical solution. This validates our approach to the finite element modelling.

Now, the reflector is analysed for the subjected maximum in-plane and out-of-plane moments with 1.5 as a factor of safety i.e. $M_x \simeq 1105$ Nm and $M_z \simeq 2175$ Nm. These are the combined moments for the 4 CMGs. So, the moments produced from the CMG are applied at the respective attachment point. The unsupported boundary conditions are applied using "inertia relief".

The finite element results for the von Mises stress are shown in Fig. 34a and Fig. 34b for the applied moments in the x and z directions, respectively. As seen from the results, the stresses are within limits. The maximum values are localized stresses in the vicinity of the load application points, as concentrated moments are applied and stresses are much less than the maximum value in other structural members.

5.2.6. Self-rotation loads

The orientation of the reflector is adjusted by using the CMGs. This rotation about its own axes will exert centrifugal forces on the reflector. A finite element analysis is carried out to estimate the stresses developed due to these centrifugal forces. ABAQUS© facilitates the application of such forces by defining the subjected angular velocity or rotational acceleration about a defined axis. The terminology used for these forces is the "rotational body force". The maximum values of angular velocities $\omega_x, \omega_y, \omega_z$ are given in Section 4.2.2 as 7.89×10^{-3} rad s^{-1}, 5.86×10^{-4} rad s^{-1} and 5.05×10^{-3} rad s^{-1}, respectively. The analysis is carried out for the maximum in-plane and out-of-plane angular velocities i.e. for ω_x and ω_z. The unsupported boundary conditions are simulated using "inertia relief".

Figs. 35a and 35b show the finite element simulation results for the von Mises stress developed due to the

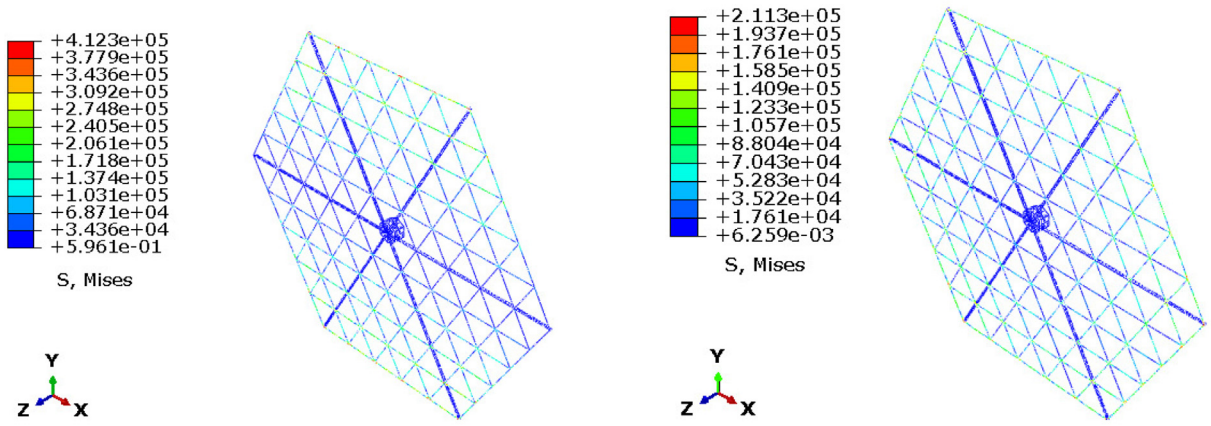

Fig. 35. Stresses in the reflector structure subjected to an angular velocity $\omega_x = 7.89 \times 10^{-3}$ rad s^{-1} (a) and $\omega_z = 5.05 \times 10^{-3}$ rad s^{-1} (b).

applied angular velocities in the x and z directions, respectively. As seen from these plots, the stresses developed are negligible.

5.2.7. Thermal expansion loads

Stresses are developed in the reflector material subjected to a temperature field by virtue of the thermal coefficient of expansion (κ). These stresses are given as Popov and Balan (1999):

$$\tau_{th} = E\kappa\Delta T \tag{83}$$

where ΔT is the temperature difference.

If a structural system is made by joining two or more dissimilar materials, the differential thermal stress will act on the system when subjected to a temperature field. In the reflector designed in this paper, discrete connections through springs are proposed between the reflector film and the structure as shown in Fig. 32. Hence, the differential thermal stress between structure and reflector film will be minimized. The differential thermal stress between the film and its supporting mesh is avoided by using the supporting mesh of the same material as of the reflector film. The studies on the thermal characteristics of 2 μm aluminized Kapton film subjected to a realistic in-orbit temperature difference of 250 °C with the coefficient of thermal expansion of film as 20 $\times 10^{-6}$K^{-1}, showed that the maximum variation in dimension is 0.5% (Hedgepeth et al., 1981). Hence the reflector film can be used in the in-orbit thermal environment with desired functionality.

The reflector structure considered here is made from graphite-epoxy material which has a very low coefficient of thermal expansion. These graphite-epoxy materials can be custom tailored to have desired properties. The present truss structure formed using graphite-epoxy tubes of different sizes at different orientations, will develop a thermal stress when subjected to a thermal environment due to its structural arrangement.

The Earth-orbiting objects are typically subjected to a thermal environment with contributions from the direct solar flux, albedo, i.e., the fraction of the solar energy incident on the Earth that is reflected and Earth's infrared thermal radiation (Birur et al., 2003). The maximum values for these contributions for an object in low Earth orbit are estimated as 1414 Wm^{-2} for direct solar irradiation, 560 Wm^{-2} for albedo and 241 Wm^{-2} for Earth's radiation (Birur et al., 2003). These values are scaled by the projected area of the object. It is noteworthy that the aluminized reflector surface constitutes one of the faces of the reflector. The worst-case scenario for the supporting structure is to face sunlight directly. A temperature difference, assuming all heat generating contributors for the worst-case scenario, is derived as per the procedure given in Ref. (Birur et al., 2003). This temperature difference is approximately 400 K, with the absorption coefficient and emissivity of graphite-epoxy material taken as 0.8 (Dai et al., 2021) and 0.85 (Adibekyan et al., 2019), respectively.

A finite element analysis is carried out to estimate the stresses developed in the reflector subjected to this temperature difference. The unsupported boundary condition is imposed using "inertia relief" and the "Nlgeom" option is activated to capture any nonlinear effects. Fig. 36 shows the stresses developed due to the subjected thermal environment. The developed stresses are well within limits.

The effects of space environment and temperature on the strength of graphite-epoxy materials are studied in Refs. (Fox et al., 1987; Hyer et al., 1983; Milkovich and Herakovich, 1984), respectively to assess the suitability of these materials for space applications.

5.3. Manufacturing strategies

In-space manufacturing offers many advantages over on-ground manufacturing. In principle, structures of very large scale can be manufactured with ease in the weightlessness of space. Oberth in his pioneering early work proposed to manufacture reflectors in space, with the use of leftover aluminium parts from rockets for coating of reflec-

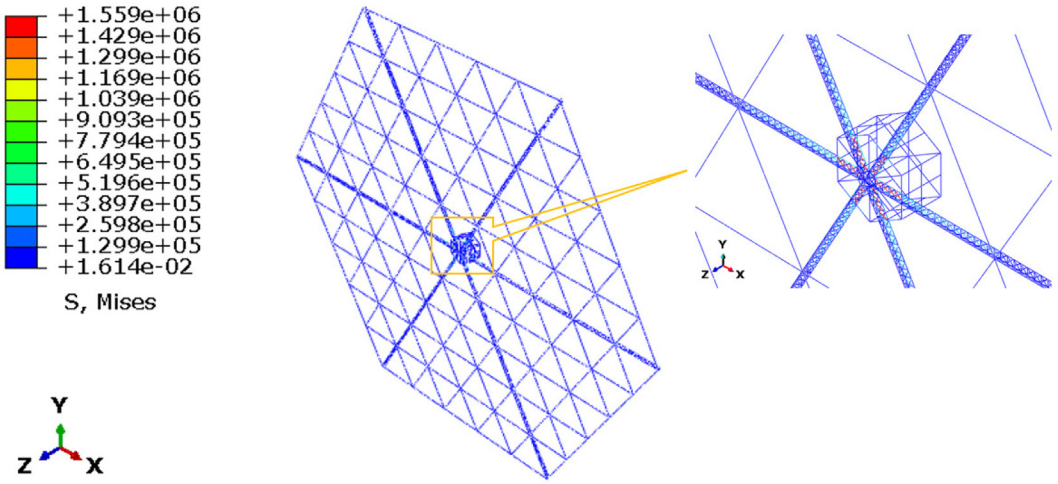

Fig. 36. Stresses in the reflector structure subjected to a temperature difference of 400 K.

tors (Oberth, 1929). Indeed, the requirement of a vacuum for physical vapour deposition process is automatically satisfied in space. The in-orbit manufacturing strategies for the present reflector design are proposed here.

Metalized polymer film manufacturing in space is very well studied and described in the works by Drexler (1979) and Lippman (1972). The proposed reflector has tubular trusses as a structural member supporting the reflecting membrane. General Dynamics-Convair made an initial effort called "Space Construction Automated Fabrication Experiment Definition Study" (SCAFEDS) to develop a design for a "beam builder" machine capable of fabricating a 1.2 m diameter truss (Bodle, 1979). From those studies, many technologies are being developed to facilitate the on-orbit manufacturing of space structures, especially space trusses. An additive manufacturing process has revolutionized the space structure manufacturing. The most complex structure with the desired shape and materials can be manufactured with the help of 3D printing. 3D printing in space is as effective as it on-ground (Prater et al., 2019). One of the concepts based on in-space 3D manufacturing is SpiderFab ™ by Tethers Unlimited, Inc. (Hoyt, 2013). The manufacturing of structural members, their assembly to form a full structure and then integration of functional components like reflector film to structure can be achieved with "SpiderFab Bot". Another such in-space manufacturing concept is the Archinaut™ by Made in Space, Inc. (Joyce et al., 2017). Using such concepts, the reflector proposed in this paper can be manufactured in-space. Fig. 37 shows the important events during in-space manufacturing and assembly of the reflector.

6. Economic analysis

Some of the initial studies of Ehricke (1979), as well as studies of NASA Billman et al. (1977), Billman et al. (1978a), Billman et al. (1978b) carried out on the concept of generating energy using orbiting solar reflectors in the 1970s and 1980s also analysed its economic cost to give a prediction on the economic viability of the concept. In a more recent study of Lior (2013), the authors calculated the internal rate of return and investment payback period (based on net present value) as part of their economic feasibility analysis. These works included the investment cost of SPFs in their economic analysis as they considered that the orbiting reflectors and the SPFs were jointly invested in and built at the same time.

However, the growth witnessed in the SPF industry and the space industry are independent of one another. In the last two decades, there has been a significant growth in global solar power industry with multi-GW sized solar farms currently operational and larger sized SPFs being envisaged for this decade. Similarly, the space industry has witnessed growth in the advancement in space fabrication and manufacturing technologies as well as space transportation technologies which engendered the reusability of launch vehicles ultimately leading to a fall in space launch costs.

For the reference architecture proposed in this paper, an economic analysis conducted and presented in this section investigates how different factors influence the average cost of 1 MWh of additional electricity generated by SPFs using illumination received from orbiting solar reflectors. The reflector configuration is designed to cover an effective area of approximately 1 km diameter. Each reflector has a regular hexagonal shape with a mass density of approximately 18.8 gm^{-2} for CMGs, structure and reflecting surface. The reflector is considered to have a 20-year lifetime, a procurement cost of 375 $/kg and an annual maintenance cost of 5.6 $/kg (this value is adapted from Ref. (Lior, 2013)). It is assumed that advances in technology offset cost increases presented in Ref. (Lior, 2013) and that such procurement costs can be envisaged as a future target for commercial in-orbit fabrication services. It is also worth noting that much of the reflector consists of simple truss-like structures. A sensitivity analysis of procurement costs is also provided later. In view of the advancement in space trans-

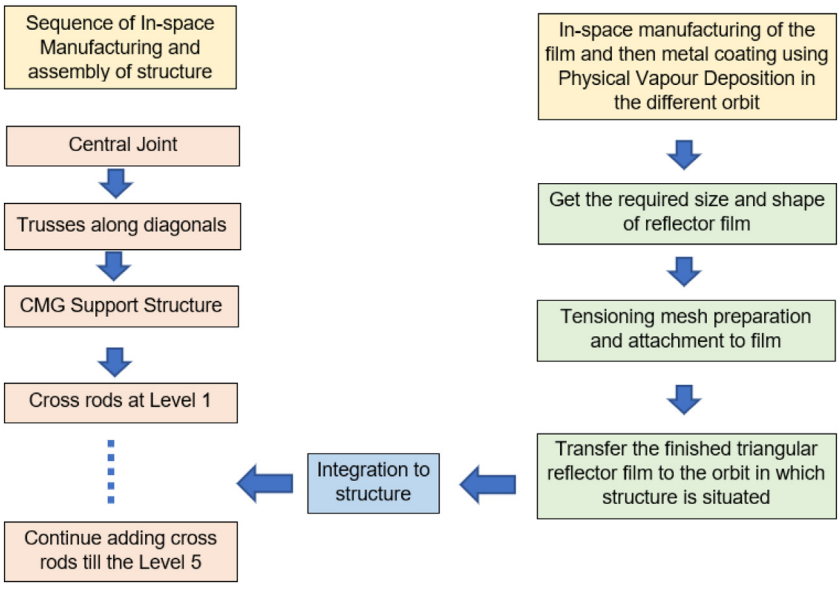

Fig. 37. Sequence for the on-orbit manufacturing of the reflector.

portation technologies for reusability of launch vehicles, it is anticipated that space launch costs could in principle fall to as low as approximately 10 $/kg (Jones, 2018). For this reason, this economic analysis considers a range of values for the reflector launch costs, the highest value being the Falcon Heavy launch cost of 1400 $/kg (Jones, 2018).

As discussed in Section 3.6, the total quantity of energy delivered to the selected farms in a day is 283.84 MWh. It is assumed that the existing SPF panel array has a conversion efficiency of 20% and covers 50% of the land area that receives energy from the orbiting solar reflectors. Consequently, over a period of one year, the additional energy generated by the selected solar farms is 9842.152 MWh as calculated in Appendix B.

The average cost per MWh of the energy generated by the reflector is then analysed for a range of launch costs at a 15% discount rate, given that the risks associated with implementing and operating the reflector is not fully known. The average cost is obtained by dividing the annualized total cost of the orbiting solar reflector system with the calculated annual additional energy generated by the SPFs. The annualized value of the total cost of the orbiting solar reflector system is dependent on the different cost components including the launch cost. The average unit cost represents the average price for which wholesale electricity should be sold to recover costs. Because the reflector enhances electricity generation across different countries and electricity price is not uniform in different locations, this analysis focuses on determining the condition to achieve a target average cost of 70 $/MWh for the generated electricity considering different discount rates, different mass density levels and different procurement costs.

Fig. 38(a) shows the average cost per MWh of additional energy generated for 2 levels of discount rate. In addition to the 15% discount rate, an optimistic 5% discount rate which is more appropriate for a fully understood technology is also considered. While the target average cost of electricity of 70 $/MWh was not realised at the 15% discount rate, under the 5% discount rate, the target cost was achieved at a launch cost of 232 $/kg. This suggests that further reduction in risk through public sector investment is essential for this technology to be feasible. Further analysis only focuses on the 15% discount rate.

Advancement in space technologies can reduce the reflector mass density. For this reason, the effects of the reflector mass density on the average cost of electricity is analysed. Different levels of mass density are considered specifically $15.98\ gm^{-2}, 13.16\ gm^{-2}, 10.34\ gm^{-2}$ which corresponds to a reduction of 15%, 30% and 45% respectively in comparison with the original mass density.

Fig. 38(b) presents the average cost per MWh of additional energy generated at different launch costs and different reflector mass densities. With a reduction in the mass density, the average cost of electricity generated is also reduced; however, the target cost of 70 $/MWh was only achieved with at least a 30% reduction in the mass density. For a mass density of $13.16\ gm^{-2}$, the target cost was achieved at a launch cost of 11 $/kg, while with a mass density of $10.34\ gm^{-2}$, the target cost was achieved at a launch cost of 126 $/kg.

Next, a sensitivity analysis is carried out on the influence of reflector procurement cost on the average cost of electricity generated. A range of procurement costs is considered at 225 $/kg and 300 $/kg, which correspond to a reduction of 20% and 40% to the base procurement cost of 375 $/kg, respectively. The base case procurement cost of 375 $/kg is also included in the analysis. As shown in Fig. 39, the target cost was only achieved at a procurement cost of 225$/kg and launch cost of 34 $/kg.

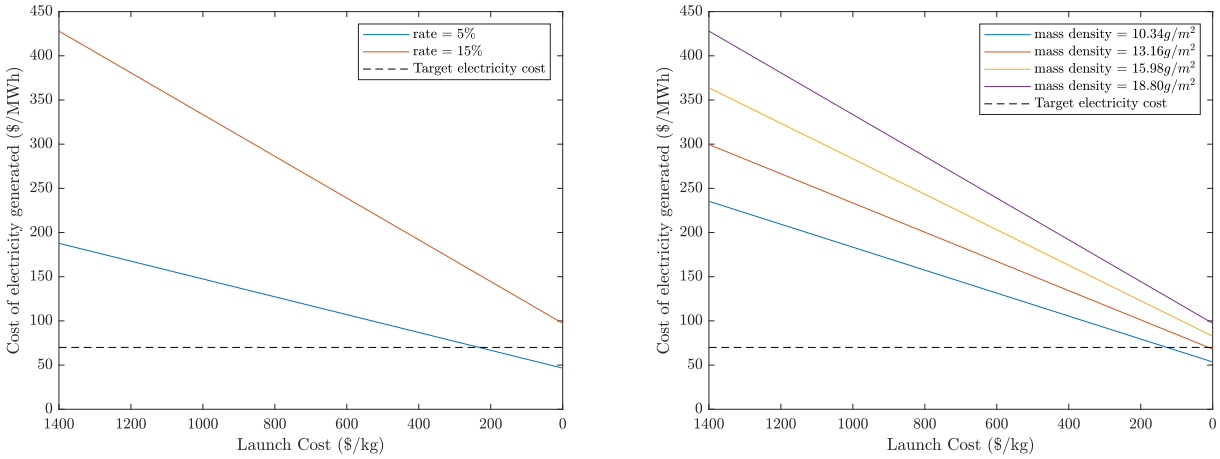

(a) (b)

Fig. 38. Average cost of additional electricity generated at different discount rates for different launch costs (a) and reflector mass densities (b).

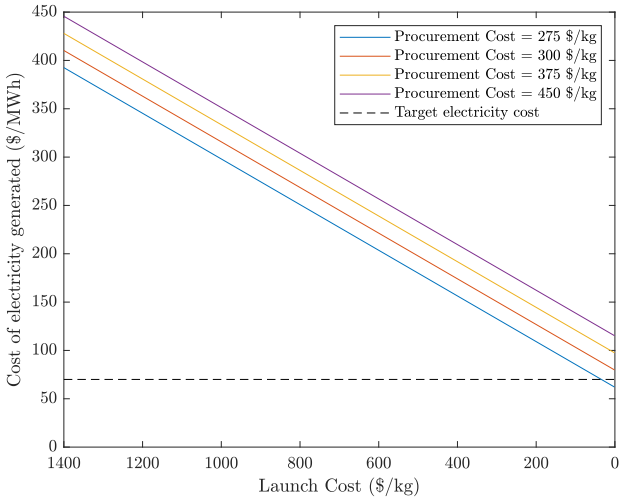

Fig. 39. Average Cost of additional electricity generated at different reflector procurement costs.

7. Discussion

7.1. Locations of new solar power plants enabled by the reflector orbit

The concept of orbiting solar reflectors has the advantage of being decoupled from terrestrial assets, i.e., the orbits can be selected based on the existing infrastructure to deliver solar energy. The orbit of the reference architecture here is selected from virtually infinite possible orbits and constrained through ensuring orbital passes over a selected SPF. This is an example of ground infrastructure informing the choice of the orbit. As discussed in Section 3.7, the selected orbits can be modified for more favourable orbital passes through passive means by SRP or actively through other propulsive methods.

It is also possible that selected orbits could inform new SPF locations. The ground track of an orbit may trace locations on the Earth that receive high solar radiation that may be suitable for a SPF or other infrastructure that uses solar energy. Appropriately built infrastructures would then allow one or two passes a day by the reflectors, enhancing their utility and global clean energy generation. Fig. 40 shows the ground track of the orbit discussed in this paper overlaid on a global mean yearly insolation map for the years 1990–2004.

As observed in Fig. 40, some of the existing SPF are already located in the regions of high insolation. Fig. 40 also shows that the ground track traces regions where there is currently no large-scale solar power infrastructure. One example of this is north Africa, where the orbit potentially allows four passes in a day in central and western parts of north Africa. This is one of the regions that receive the highest insolation on the Earth. Similarly, there are also passes in the eastern and southwestern Africa, the coasts of Brazil and Chile, the central regions of the USA, parts of Australia and the western China and in Pacific Ocean. New solar power infrastructures can be built in these regions for both daytime solar energy utilisation directly from the Sun and nighttime utilisation by using orbiting solar reflectors. It appears clear that some of these regions require offshore infrastructures, for which floating SPF may be considered (Bonetti and McInnes, 2019). The duty cycle, hence the profitability, of the reflector system would also be increased while enhancing global clean energy generation. It is important to reiterate here that many other orbital configurations are also possible to maximise the solar energy delivery other than the one presented in this paper.

Over the year, each double overhead pass of the reflectors would enable the generation of 2288.55 MWh of energy, in addition to the 9842.152 MWh generated by the selected SPF using reflector illumination as discussed in Section 6. In Fig. 41, the average cost of electricity generated is presented considering additional energy delivery by the reflector in 1, 2 and 3 double overhead passes. As

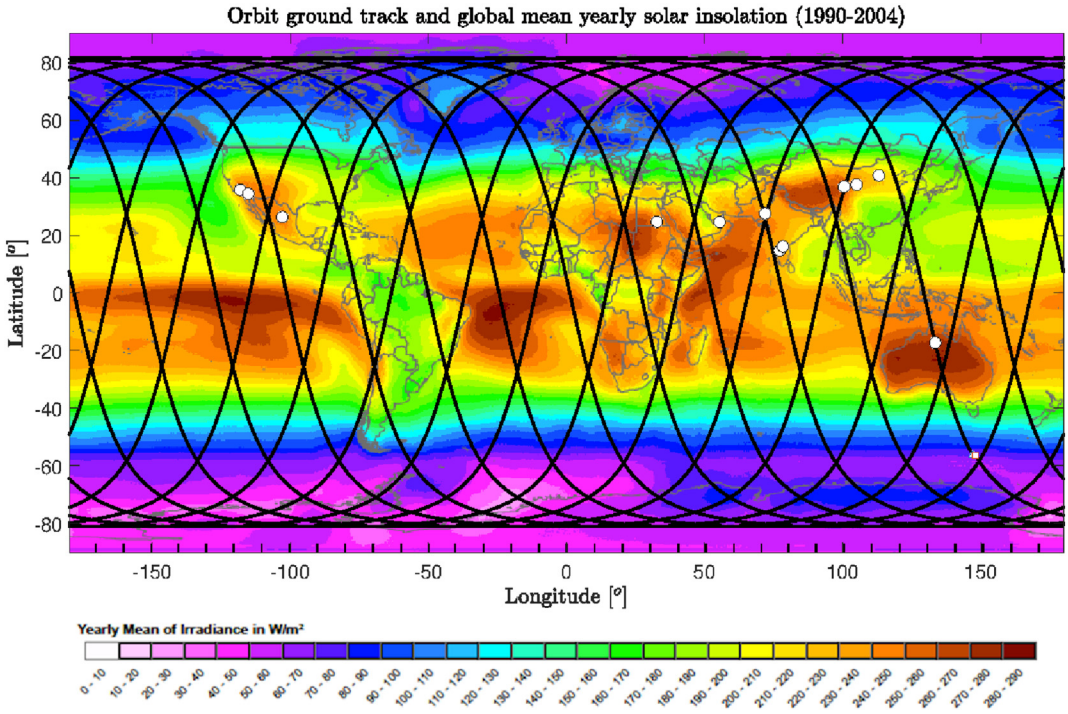

Fig. 40. Orbit ground track overlaid on a global mean yearly insolation map between years 1990–2004 (The insolation map is freely available at https://www.soda-pro.com/maps/maps-for-free (Accessed March 3, 2022). Used with permission.).

expected, the average electricity cost per MWh reduces with utilization of more orbit passes for energy delivery. Despite this reduction, the target cost of 70 $/MWh could only be realised with 2 additional double passes and 3 double passes at 126 $/kg and 11 $/kg respectively.

Finally, it is instructive to estimate the maximum number of SPFs that could be serviced per orbit taking into account attitude control constraints and assuming that the SPFs are equally spaced in longitude. This scenario represents an ideal case where the duty cycle is maximised, under the assumption that the actuators are designed to deliver the peak angular momentum and torque during the tracking phase. Then, taking a pass time of 17 min and a reorientation time of 6 min (see Table 6), a maximum of 3 SPFs per orbit can be serviced, with a total of 42 passes per cycle (note that this result is consistent with the analytical results presented in Ref. (Viale and McInnes, 2023)). Assuming an average of 21.83 MWh per pass (this is the average of the delivered energy values in Table 5 passes in a day cycle, the energy generated by the SPF over the period of one year would be 31937.76 MWh, which is more than one order of magnitude larger than the nominal 9842.152 MWh discussed in Section 6. Note that, in principle, this number can be even larger if the actuator is designed to deliver larger torques during the reorientation phase. As discussed in Ref. (Viale and McInnes, 2023), the maximum number of SPFs that can be visited per orbit with reorientation-driven actuator sizing is 6, thus doubling the energy figures discussed above.

7.2. Illumination levels on ground, stray light and the appearance of reflectors in the night sky

One of the potential regulatory issues with the utilisation of orbiting solar reflectors is the illumination levels on ground. As discussed earlier, the projected image of the solar disk is large, with stretched ellipses at low elevations which become smaller as the reflector approaches to its zenith point. As the intercepted solar energy is the same throughout the pass due to the fixed size of the reflectors,

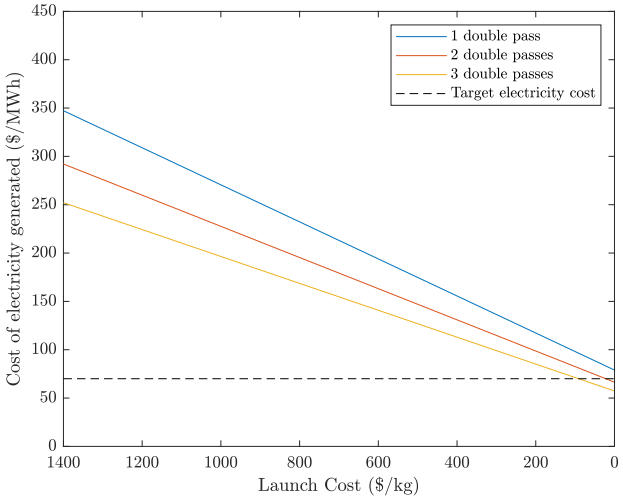

Fig. 41. Average Cost of electricity with additional passes utilised for different Launch Cost.

the solar power density on ground varies with the size of the solar image on ground. The solar power density is effectively the illumination level on ground, which can be expressed in the units of lux for a comparison with terrestrial reference levels, as in Çelik and McInnes (2022):

$$\varsigma = I_{lx}\frac{A_M}{A_{im}}\cos\left(\frac{\psi}{2}\right) \tag{84}$$

where σ_{lx} and I_{lx} denote solar power density and solar flux in lux. Eq. 12 is the same as Eq. 84, but here the analysis is performed with the solar flux value in lux and without the area of the SPF. Here, I_{lx} is calculated as 128000 lux on top of the atmosphere, and approximately 100000 lux on the ground after atmospheric losses (IES Calculation Procedures Committee, 1984). The latter value is taken as the base value on ground and the value of ψ during the Sun Cable pass is considered for the reference orbit altitude. In J_2-perturbed motion, this orbit altitude varies over the course of an orbit, but the variation is not considered here, and the orbit is assumed at a fixed altitude. The illumination on ground for different hexagonal side lengths of reflectors between 10 to 500 m can then be seen in Fig. 42. The illumination profiles show very low values at the beginning and end of a pass, and higher values at near zenith point with a peak at the zenith point, as expected from the evolution of the projected solar image. For the smallest reflector of $l = 10$ m, the illumination levels only slightly exceed the full-moon illumination level (0.14 lux (Canady and Allen, 1982)) for about 3 min. For a 50 m side length reflector, the illumination level is above the full-moon level most of the pass but does not reach the living-room level (50 lux (Pears et al., 1998)). This level is surpassed by a 250 m side length reflector for 5 to 6 min during a pass and the peak illumination is level is approximately equivalent to the illumination levels at sunrise and sunset, i.e. ~400 lux[3]. The highest illumination level occurs for a 500-m side length hexagonal reflector, where there is a time period of 3 min with illumination levels higher than the sunrise/sunset level which reaches the overcast-day levels (~1000 lux) at its peak. It is worth noting that full daylight levels (~17500 lux) is never reached with the reflector sizes considered for this reference architecture study, and other high levels of illumination (e.g. overcast day and sunrise/-sunset) are only for relatively short duration during an orbital pass. It is also important to know whether there is a minimum level of illumination required for solar photovoltaic systems to generate electricity. However, analysis has shown that silicon heterojunction solar cells, with an efficiency of order 20%, show only a modest fall off in efficiency at low light intensities at elevated temperatures (Tress et al., 2019). Indeed, efficiency improves at lower temperatures, which may be expected at dawn and dusk. Relevant to this point, experiments under moonlight concentration at a solar tower plant may also be noted (Guo et al., 2020). Enhanced illumination can in any case be delivered by scaling up number of reflectors simultaneously illuminating the SPF. Fig. 42 for example shows the illumination profile of 500-m side length single hexagonal reflector, whose area is equivalent to the area of four 250-m side length hexagons, one less than considered in this paper. It can then be understood that another same-sized reflector will take to illumination slightly beyond the overcast-day levels. As another example, twenty 250-m side-length hexagonal reflectors would result in a peak illumination level of approximately 5000 lux, which is still less than half of full daylight levels shown in Fig. 42. It is worth reiterating that the highest illumination occurs only for a few minutes where most of the solar energy is delivered. Moreover, the impact of this illumination on biodiversity, especially in the diurnal cycle of the plants and animals will be a subject for future studies, but relatively low levels of illumination for the majority of a pass suggest that the impact may be relatively minor. One of the other potential regulatory issues is the appearance of reflectors in the sky. It has been debated that large scale constellations could be detrimental for ground-based astronomy (Smith, 1982; McDowell, 2020), especially with the plans for tens of thousands of Starlink satellites to be deployed [4]. It can be argued for orbiting solar reflectors that, as the reflectors are primarily considered for dawn/dusk hours, limited overlap is expected between orbiting solar reflectors and astronomical observations, as those hours are still relatively bright for astronomical observations. Moreover, as previously noted

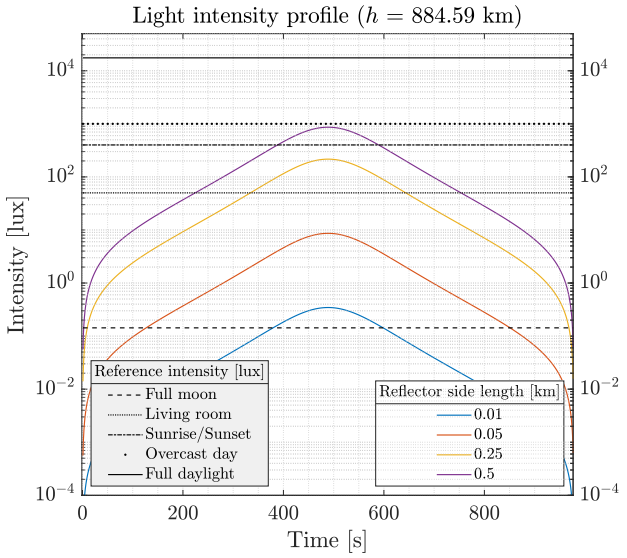

Fig. 42. Illumination levels on ground for the Sun Cable pass for different hexagonal reflector sizes. Each curve shows a single reflector scenario. The area of the 500-m side length reflector corresponds to the area of approximately four 250-m side length reflectors.

[3] The reference illumination values for sunrise/sunset, overcast day and full daylight are obtained from "Radiometry on photometry on astronomy" at http://stjarnhimlen.se/comp/radfaq.html#10. Accessed on March 9, 2022.

[4] C. Henry, SpaceX submits paperwork for 30000 more Starlink satellites, 15 October 2019, https://spacenews.com/spacex-submits-paperwork-for-30000-more-starlink-satellites/ (Accessed 10 September 2021)

in Ref. (Çelik et al., 2022), high elevation locations preferred for telescopes are not necessarily the best locations for SPFs due to the considerations of accessibility and insolation, therefore, again, limited overlap is expected in terms of locations. Nevertheless, the idle-mode control strategy outlined earlier for the non-operational phases of the reflectors mean that, the reflectors will not be illuminated, hence not reflect sunlight back to the Earth in principle. In any case, here, a simple analysis is presented to estimate the angular diameter of hexagonal reflectors in sky with different side lengths when illuminated during the Sun Cable pass. For a ground-based observer that is considered to be a point on the Earth, the angular diameter of the reflector can be found as follows

$$\alpha_r = 2\arctan\frac{l\sin(\pi/3)\cos(\psi/2)}{h} \tag{85}$$

where the angle α_r denotes the angular diameter of the reflector to a ground-based observer, l denotes the reflector sidelength, ψ denotes the angle of incident of incoming and outgoing sunlight and h is the orbit altitude. Here, as the reflector is pitched at an angle $\psi/2$, the term $l\sin(\pi/3)\cos(\psi/2)$ denotes the projected side-to-side length that is seen by a ground observer. As discussed earlier, the ψ angle is variable during a pass. This variation is calculated between 86 deg and 94 deg degrees for the Sun Cable pass. For a simple estimation, $\psi = 90$ deg is taken such that the reflector is in the zenith point. For a 884.59 km altitude orbit and a range of reflectors diameters between 20 m to 1 km, the α_r angle is calculated by Eq. 85 and the results are given in Table 9.

According to Ref. (Yanoff and Duker, 2008), the naked human eye can resolve an object that has an angular diameter of down to 0.0003 rad, which is approximately equivalent to Venus as a disk. Then, only the reflector with the side length of 0.5 km in Table 9 would be resolvable to a naked eye when they are operational. It was also previously noted for the failed Znamya-2 experiment that the light shone from the reflectors would not cause damage to human eyes, unless one looks through binoculars or a telescope for a long duration (Laframboise and Chou, 2000). In an orbital pass such as that of Znamya-2, the reflector would appear and disappear from view within one second. Note that the orbital speed of the reflectors at 884.59 km altitude is 7.41 km/s and the orbital pass lasts only ~17 min, after which the reflector attitude is taken into its idle mode where in principle no light is reflected back to the Earth.

Table 9
Angular diameter of the reflectors at 884.59 km orbit during the Sun Cable pass.

Hexagon side length [km]	Angular diameter [rad]
0.01	7.9936×10^{-6}
0.05	3.9968×10^{-5}
0.25	1.9984×10^{-4}
0.5	3.9968×10^{-4}

Finally, stray light during the operations should be taken into account. As noted earlier, the solar image will take the shape of a stretched ellipse at low elevations, gradually shrinking in both semi-major and -minor axes until the zenith point, before stretching again. As the size of a SPF is fixed, the areas outside of the plant will inevitably be illuminated for a short duration. For example, at a 10 deg elevation, semi-major and -minor axes of the solar image are 68 km and 11.8 km, respectively, in the Sun Cable pass. Both of these dimensions are larger than the considered radius of SPFs (i.e., 5 km). The SPF will only use an area of 78 km^2 of the illuminated 802.4 km^2. The utilisation of the illuminated area will gradually improve as the solar image shrinks, which also means an increase in solar power density, and the solar image will eventually illuminate only the area of the SPF, i.e. no stray light. Here, the percentage ratio of stray light area to solar image area is calculated for both Sun Cable passes, which exemplifies both an overhead and an offset pass. The result is presented in Fig. 43. As expected, initially most of the illumination is outside of the SPF boundaries, but it shrinks rapidly as the elevation increases. For the overhead pass, the stray light area percentage decreases from 95% to 15% in approximately 3 min. Shortly after this, it is contained within the SPF boundaries. The occurrence is similar for the offset pass as well, but this time the image stays relatively stretched even at its highest elevation, which is approximately at 60°. As a result, the lowest percentage of stray light is approximately 15%. While the stray light area looks large in low elevations, it is important to note that large image areas will mean low solar power density, and hence low illumination, as it can be seen in Fig. 42, therefore its impact will be minimal.

SPFs are typically built in remote locations but it appears that some stray light may reach cities and even exceed country boundaries, especially at low elevations.

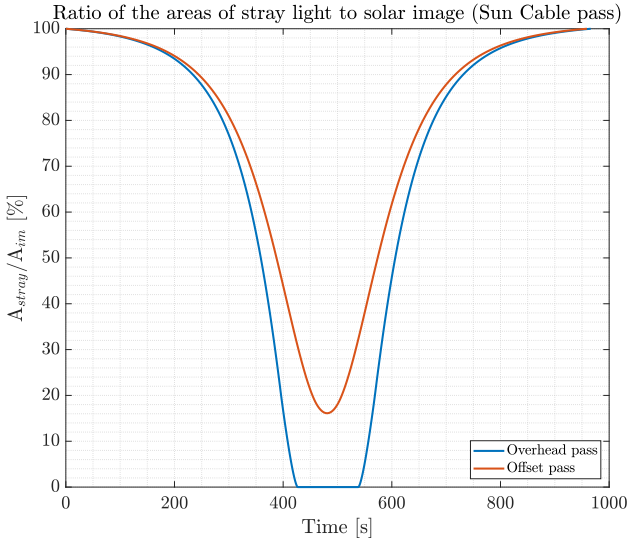

Fig. 43. Percentage of stray light area in total solar image area during an overhead and offset pass for the Sun Cable visit.

Similarly, the impact of this daily illumination, albeit short duration, on the surrounding biodiversity will need to be taken into account. However, it is worth iterating that the illumination levels will be low for the majority of an orbital pass.

7.3. Applications other than electricity generation

There are also other applications that orbiting solar reflectors may be used for in addition to delivering sunlight to SPFs. The studies as early as in 1920s suggested the use of the reflectors for illumination of airports or high latitude regions (Oberth, 1929). This idea was also considered in later studies (Ehricke, 1979; Canady and Allen, 1982; Fraas, 2019). While street illumination is a rather straightforward utility of the reflectors, the orbit altitude considered here does not offer long duration illumination of large areas. Street lighting type applications would either require higher altitudes for a longer pass duration or lower altitudes with a train of reflectors for longer duration. Nevertheless, they can still be considered for on-demand illumination for disaster relief or other similar illumination applications.

Nevertheless, there are several other applications in which orbiting solar reflectors can be used. Another application of night-time illumination is enhancing the photosynthesis of plants, whereby also using them as carbon sinks (Gao et al., 2022), but the long-term effects of this should be further studied. Alternatively, there is a growing interest in low to zero carbon energy solutions other than solar energy or in technologies for carbon-capturing to keep carbon emissions within the net-zero targets to mitigate the effects of climate change. One such solution is biofuel production through photosynthetic marine algae (Stephenson et al., 2011). Such organisms do not require high quality agricultural land, has higher sunlight-to-biomass conversion ratio than plants and also captures CO_2 from the atmosphere (Stephenson et al., 2011). They are used for generating biofuel in different forms (Stephenson et al., 2011). One can then imagine large ponds of algae near water sources to enhance the production of biofuel at night through the sunlight provided by orbiting solar reflectors.

Furthermore, orbiting solar reflectors may also be considered for long-term speculative applications of climate engineering (Salazar et al., 2016) or for non-terrestrial applications around the Moon and Mars to supply solar energy or illumination for future endeavours in space (Bewick et al., 2011; Gillespie et al., 2020; Çelik and McInnes, 2022), but those are out of scope of this study.

7.4. Filamentary CMGs

The dimension of the reflector was here selected by constraining the CMG size, as discussed in Section 4.4. As dictated by Eq. (59), by increasing the size of the CMG a larger angular momentum can be produced or, equivalently, the CMG mass can be reduced to produce the same angular momentum. In principle, this can be done using deployable filamentary "isotensoid" wheels, as first proposed in a NASA study (Hedgepeth et al., 1981). These wheels are made of a mesh of small filaments with particular fiber patterns such that the tension of the fiber is constant at all location. The main advantage is that the wheels can be stored in a smaller volume at launch and then deployed in orbit. For example, assuming that a 10 m radius deployable CMGs is used with the same nominal angular momentum as the rigid wheel used in this study, the total mass per CMGs can be reduced to 44 kg (this can be calculated using Eq. 29 in Ref. (Hedgepeth et al., 1981)), almost three times smaller than the rigid CMG mass calculated here. However, it is apparent that additional issues related to the deformation of the wheel during gimballing may emerge, which should be further investigated.

On the other side, a large CMG could be replaced by a set of multiple CMGs with the same total angular momentum, in an attempt to reduce their size. However, it can be easily shown that if mass is conserved, the required dimension of the rotor does not change. In fact, from Eq. (59), let $H_0 = km_0r_0$ be the angular momentum of single CMGs (it is noted that Eq. (59) takes into account the effect of the angular velocity based on the stress constraint (58)) where $k = \sqrt{2/(3+\nu)(\tau_{\text{cmg}}/\rho_{\text{cmg}})}$ only depends on the CMG material and assume that this is split into two CMGs with equal mass m_1 and radius r_1 such that $2m_1 = m_0$. Then the sum of the angular momentum of the CMGs would be $H_1 = 2cm_1r_1$. Imposing $H_1 = H_0$, it is apparent that $r_1 = r_0$, i.e., the radius of the smaller CMGs need to be equal to the original radius, implying that the rotor thickness must be reduced.

Although further studies will be required to investigate the interaction between the CMGs and a more realistic non-rigid reflector, it appears (as noted in Ref. (Viale and McInnes, 2023)) that "large" CMGs are an inevitable choice for this application.

8. Conclusions

This paper has presented a single reference architecture for orbiting solar reflectors to enhance the output of terrestrial solar power farms (SPF). The analysis has covered orbital dynamics, attitude dynamics, structural and economic aspects.

In order to maximise the daily solar energy delivery to large SPFs of fixed 10 km diameters, a circular Sun-synchronous, repeating ground track orbit at an altitude of 884.59 km has been selected as the reference orbit. The orbit groundtrack is anchored at the Sun Cable SPF in Australia. The reflectors in this orbit can service 9 large

SPFs over one sidereal day, delivering a total quantity of 283.8 M W h solar energy. Attitude control requirements were then derived to track these SPFs and reorient the reflectors between passes. The minimum reorientation times were calculated, assuming that the control actuator of the reflectors is designed to deliver the peak angular momentum and torque during the tracking phase. Based on a trade-off study on actuators for large planar structures, a set of four carbon fibre control moment gyros (CMGs) in a pyramid configuration have been selected as the main control actuator. The rotor radius of the CMGs is 6.5 m, which has been selected for wheels to be stored inside a SpaceX Starship fairing. Moreover, variable reflectivity coatings and tip vanes have been considered to generate torques for actuator desaturation around in-plane and out-of-plane axes. A hexagonal reflector has been considered for its versatility for in-orbit manufacturing and assembly, where it is assumed that the shape would be assembled from the equilateral triangular elements with 50 m side length. A combination of the shape requirement and actuator constraints eventually leads to an overall hexagon side of 250 m. The reflector assembly has a mass density of 18.8 gm^{-2} with structural support and other spacecraft subsystem elements. To have a total reflective area equivalent to (at least) a 1 km diameter disk, a minimum of five reflectors are required.

A cost analysis then reveals that assuming a 20-year operational lifetime, a target average cost of additional electricity of $70/ M W h can be achieved at a 5% discount rate, and a launch cost of $232/ kg. If a more realistic discount rate of 15% is used, then the same target price can be achieved by reducing the reflector mass density to approximately 13.2 gm^{-2}. Even though this value is smaller than that found in this paper, it is expected that future advancements in space technology may lead to a reduction in the mass density, with the additional advantage that smaller actuators can be used for the same reflector size.

In summary, the paper has demonstrated that orbiting solar reflectors can deliver new space-based energy infrastructure to support terrestrial solar power plants. It has been shown that key technologies are necessary, for example, large control moment gyros, while there is also a timely convergence of falling launch costs, growing global demand for clean energy and new technologies for in-space manufacturing of large space structures. While the launch costs required for breakeven are below present-day costs, future fully reusable launch vehicles able to lift significant mass to Earth orbit, and with a rapid launch cadence, can in principle enable this and other opportunities to deliver new ways of using space.

Declaration of Competing Interest

The authors declare that they have no known competing financial interests or personal relationships that could have appeared to influence the work reported in this paper.

Acknowledgements

This project has received funding from the European Research Council (ERC) under the European Union's Horizon 2020 research and innovation programme (grant agreement No. 883730). CRM is also supported by the Royal Academy of Engineering under the Chair in Emerging Technologies scheme. We also thank Sun Cable for sharing information on their solar power farm.

Appendix A. Light staring point

Let $\mathbf{r}_l$ be the position vector representing the centre of the reflected light cone on Earth. Given the direction of the reflected light $\hat{\mathbf{u}}_r$, this can be written as the sum

$$\mathbf{r}_l = \mathbf{r}_r + \xi\hat{\mathbf{u}}_r \tag{A.1}$$

where ξ is a parameter to be determined. Assuming spherical Earth and imposing $|\mathbf{r}_l| = R_E$, Eq. (A.1) can be rewritten as:

$$|\mathbf{r}_r^2| + \xi^2 + 2\mathbf{r}_r \cdot \xi\hat{\mathbf{u}}_r = R_E^2 \tag{A.2}$$

which will then lead to the two solutions:

$$\xi_{1,2} = -\mathbf{r}_r \cdot \hat{\mathbf{u}}_r \pm \sqrt{(\mathbf{r}_r \cdot \hat{\mathbf{u}}_r)^2 + R_E^2 - |\mathbf{r}_r|^2} \tag{A.3}$$

Eq. (A.1) represents the actual intersection of reflected sunlight with Earth if the parameter ξ is real and positive. Furthermore, the smallest solution must be selected, as it represents the only physical intersection between the light beam and the Earth (the other solution represents the other intersection on the opposite side of Earth, which has no physical meaning). Therefore, the reflected light position vector is:

$$\mathbf{r}_l = \mathbf{r}_r - \left(\mathbf{r}_r \cdot \hat{\mathbf{u}}_r + \sqrt{(\mathbf{r}_r \cdot \hat{\mathbf{u}}_r)^2 + R_E^2 - |\mathbf{r}_r|^2}\right)\hat{\mathbf{u}}_r \tag{A.4}$$

under the conditions:

$$(\mathbf{r}_r \cdot \hat{\mathbf{u}}_r)^2 + R_E^2 - |\mathbf{r}_r|^2 \geqslant 0 \tag{A.5}$$

$$-\mathbf{r}_r \cdot \hat{\mathbf{u}}_r \pm \sqrt{(\mathbf{r}_r \cdot \hat{\mathbf{u}}_r)^2 + R_E^2 - |\mathbf{r}_r|^2} > 0 \tag{A.6}$$

Appendix B. Calculations for reflector mass and additional energy generation by solar farms

- The reflector illumination is assumed to cover an effective circular diameter of approximately 1 km with an area of 785,400 square metre.
- To achieve the required reflector illumination, five hexagonal shaped reflectors with side length of 250 m and area of 169379.76 m^2 will be required.
- Each reflector has a mass of 3051.5 kg (Table 8), so the total mass of the reflectors is 15257.5 kg.
- The selected SPF are assumed to have a panel to area coverage ratio of 50% and a conversion efficiency of 20%.

- The reflector delivers a daily additional energy of 283.84 MWh to selected SPFs and has an annual capacity factor of 95%.
- The annual additional energy generated by the selected SPFs can be calculated as $283.84 \times 0.5 \times 0.2 \times 365 \times 0.95 = 9842.152$ MWh.

References

Adibekyan, A., Kononogova, E., Monte, C., Hollandt, J., 2019. Review of ptb measurements on emissivity, reflectivity and transmissivity of semitransparent fiber-reinforced plastic composites. Int. J. Thermophys. 40 (4), 1–14. https://doi.org/10.1007/s10765-019-2498-0.

Battin, R.H., 1999. An Introduction to the Mathematics and Methods of Astrodynamics. Springer. https://doi.org/10.2514/4.861543.

Bewick, R., Sanchez, J.P., McInnes, C.R., 2011. Use of orbiting reflectors to decrease the technological challenges of surviving the lunar night. In: 62nd International Astronautical Congress (IAC 2011), Vol. 2, IAF, Cape Town, South Africa, 2011, pp. 1597–1609, paper no. IAC-11-A5.1.11.

Billman, K.W., Gilbreath, W.P., Bowen, S.W., 1977. Introductory assessment of orbiting reflections for terrestrial power generation. Tech. Rep. NASA-TM-73230, NASA.

Billman, K., Gilbreath, W., Bowen, S., 1978a. Orbiting mirrors for terrestrial energy supply. Prog. Astronaut. Aeronaut. 61, 61–80. https://doi.org/10.2514/5.9781600865350.0061.0080.

Billman, K., Gilbreath, W., Bowen, S., 1978b. Solares-a new hope for solar energy. Alternat. Energy Sourc. 1 (1), 233–255.

Birur, G., Siebes, G., Swanson, T., 2003. Spacecraft Thermal Control, 485–505. https://doi.org/10.1016/B0-12-227410-5/00900-5.

Bodle, J., 1979. Development of a beam builder for automatic fabrication of large composite space structures. In: NASA. Johnson Space Center The 13th Aerospace Mech. Symp.

Bonetti, F., McInnes, C., 2019. Space-enhanced terrestrial solar power for equatorial regions. J. Spacecraft Rock. 56 (1), 33–43. https://doi.org/10.2514/1.A34032.

Borggrafe, A., Heiligers, J., Ceriotti, M., McInnes, C., 2014. Attitude control of large gossamer spacecraft using surface reflectivity modulation. In: 65th International Astronautical Congress (IAC 2014), pp. IAC–14.

Buckingham, A.G., Watson, H.M., 1968. Basic concepts of orbiting reflectors. J. Spacecraft Rock. 5 (7), 851–854. https://doi.org/10.2514/3.29370.

Bush, H.G., Heard Jr, W.L., Walz, J.E., Rehder, J.J., 1980. Deployable and erectable concepts for large spacecraft. In: Ann. Conf. of the Soc. of Allied Weight Engr. Inc, no. NASA-TM-81904.

Canady, J.E., Allen, J.L., 1982. Illumination from space with orbiting solar-reflector spacecraft. Tech. Rep. NASA-TP-2065, NASA.

Çelik, O., McInnes, C.R., 2022. Families of displaced non-keplerian polar orbits for space-based solar energy applications. In: 73rd International Astronautical Congress (IAC 2022), IAF, Paris, France, 2022, paper no. IAC-22-C1.IP.37.x69012.

Çelik, O., McInnes, C.R., 2022. An analytical model for solar energy reflected from space with selected applications. Adv. Space Res. 69 (1), 647–663. https://doi.org/10.1016/j.asr.2021.10.033.

Çelik, O., Viale, A., Oderinwale, T., Sulbhewar, L., McInnes, C.R., 2022. Enhancing terrestrial solar power using orbiting solar reflectors. Acta Astronautica 195, 276–286. https://doi.org/10.1016/j.actaastro.2022.03.015.

Chen, X., Yuan, R., Zhu, J., Liu, C., Li, J., Li, Q., 2023. Conceptual design and orbit-attitude coupled analyses of free-drift solar power satellite. Adv. Space Res. https://doi.org/10.1016/j.asr.2023.02.039.

Chobotov, V.A., 2002. Orbital Mechanics. Springer. https://doi.org/10.2514/4.862250.

Dai, Y., Bai, Y., Cai, Z., 2021. Thermal and mechanical evaluation on integration of gfrp and thin-film flexible pv cells for building applications. J. Clean. Prod. 289, 125809. https://doi.org/10.1016/j.jclepro.2021.125809.

Drexler, K.E., 1979. Design of a High Performance Solar Sail System. Massachusetts Institute of Technology, Ph.D. thesis.

Ehricke, K.A., 1979. Space light: space industrial enhancement of the solar option. Acta Astronaut. 6 (12), 1515–1633. https://doi.org/10.1016/0094-5765(79)90003-1.

Fernandez, J.M., Rose, G., Stohlman, O.R., Younger, C.J., Dean, G.D., Warren, J.E., Kang, J.H., Bryant, R.G., Wilkie, K.W., 2018. An advanced composites-based solar sail system for interplanetary small satellite missions. In: 2018 AIAA Spacecraft Structures Conference, p. 1437. https://doi.org/10.2514/6.2018-1437.

Fox, D.J., Sykes Jr, G.F., Herakovich, C.T., 1987. Space environmental effects on graphite-epoxy compressive properties and epoxy tensile properties. Tech. Rep. NASA-TM-89297.

Fraas, L., 2019. Space mirror orbit for municipal street lighting. In: 70st International Astronautical Congress (IAC 2019), IAF, Washington, DC, USA, 2019, paper no. IAC-19,C3,1,5,x49543.

Gao, X., Liang, S., Wang, D., Li, Y., He, B., Jia, A., 2022. Exploration of a novel geoengineering solution: lighting up tropical forests at night. Earth Syst. Dyn. 13 (1), 219–230. https://doi.org/10.5194/esd-13-219-2022.

Garner, C., Diedrich, B., Leipold, M., 1999. A summary of solar sail technology developments and proposed demonstration missions. Tech. Rep. JPC-99-2697.

Gillespie, D., Wilson, A.R., Martin, D., Mitchell, G., Filippi, G., Vasile, M., 2020. Comparative analysis of solar power satellite systems to support a moon base. In: 71st International Astronautical Congress (IAC 2020), IAF, Online, 2020, paper no. IAC-20, C3,4,2, x59999.

Glaser, P.E., 1992. An overview of the solar power satellite option. IEEE Trans. Microw. Theory Tech. 40 (6), 1230–1238. https://doi.org/10.1109/22.141356.

Gong, S., Macdonald, M., 2019. Review on solar sail technology. Astrodynamics 3 (2), 93–125. https://doi.org/10.1007/s42064-019-0038-x.

Guo, M., Wang, X., Wang, N., Sun, F., Zhang, X., Wang, Z., 2020. Moonlight concentration experiments of badaling solar tower power plant in beijing. AIP Conference Proceedings, vol. 2303. AIP Publishing LLC, p. 050001. https://doi.org/10.1063/5.0028526.

Haegel, N.M., Margolis, R., Buonassisi, T., Feldman, D., Froitzheim, A., Garabedian, R., Green, M., Glunz, S., Henning, H.-M., Holder, B., et al., 2017. Terawatt-scale photovoltaics: Trajectories and challenges. Science 356 (6334), 141–143. https://doi.org/10.1126/science.aal1288.

Hedgepeth, J.M., MacNeal, R.H., Knapp, K., MacGillivray, C.S., 1981. Considerations in the design of large space structures. Tech. Rep.

Hedgepeth, J.M., Miller, R.K., Knapp, K., 1981. Conceptual design studies for large free-flying solar-reflector spacecraft. Tech. Rep. NASA-CR-3438, NASA. URL https://ntrs.nasa.gov/citations/19810016602.

Hottel, H.C., 1976. A simple model for estimating the transmittance of direct solar radiation through clear atmospheres. Sol. Energy 18 (2), 129–134. https://doi.org/10.1016/0038-092X(76)90045-1.

Hoyt, R.P., 2013. Spiderfab: An architecture for self-fabricating space systems. In: AIAA Space 2013 Conference and Exposition, p. 5509. https://doi.org/10.2514/6.2013-5509.

Hyer, M., Herakovich, C., Milkovich, S., Short Jr, J., 1983. Temperature dependence of mechanical and thermal expansion properties of t300/5208 graphite/epoxy. Composites 14 (3), 276–280. https://doi.org/10.1016/0010-4361(83)90016-2.

IES Calculation Procedures Committee. 1984. Recommended practice for the calculation of daylight availability. J. Illuminat. Eng. Soc. 13(4), 381–392. https://doi.org/10.1080/00994480.1984.10748791.

Jia, Y., Xu, S., 2005. Spacecraft attitude tracking and energy storage using flywheels. Chin. J. Aeronaut. 18 (1), 1–7. https://doi.org/10.1016/S1000-9361(11)60274-4.

Jones, H., 2018. The recent large reduction in space launch cost. In: 48th International Conference on Environmental Systems.

Joyce, E.R., Fagin, M., Shestople, P., Snyder, M.P., Patane, S., 2017. Made in space archinaut: Key enabler for asteroid belt colonization. In: AIAA SPACE and Astronautics Forum and Exposition, p. 5364. https://doi.org/10.2514/6.2017-5364.

Laframboise, J.G., Chou, B.R., 2000. Space mirror experiment: A potential threat to human eyes. J. Roy. Astron. Soc. Can. 94, 237.

Laracy, J., Bador, D., Adams, D., Weigel, A., Chambers, R., Kwon, D., Proudfoot, D., Qu, S., Shoepe, T., 2007. Solar power satellites: Historical perspectives with a look to the future. In: AIAA SPACE 2007 Conference & Exposition, p. 6057. https://doi.org/10.2514/6.2007-6057.

Leipold, M.E., Wagner, O., 1996. Mercury sun-synchronous polar orbits using solar sail propulsion. J. Guidance Control Dyn. 19 (6), 1337–1341. https://doi.org/10.2514/3.21791.

Lior, N., 2013. Mirrors in the sky: Status, sustainability, and some supporting materials experiments. Renew. Sustain. Energy Rev. 18, 401–415. https://doi.org/10.1016/j.rser.2012.09.008.

Lippman, M., 1972. In-space fabrication of thin-film structures, Tech. Rep. ARC-R-410, NASA-CR-1969.

Long, Z., Zhiping, Q., 2009. Review of flywheel energy storage system. In: Goswami, D.Y., Zhao, Y. (Eds.), Proceedings of ISES World Congress 2007, Vol. I – Vol. V, Springer, Berlin Heidelberg, Berlin, Heidelberg, pp. 2815–2819. https://doi.org/10.1007/978-3-540-75997-3_568.

McDowell, J.C., 2020. The low earth orbit satellite population and impacts of the spacex starlink constellation. Astrophys. J. Lett. 892 (2), L36. https://doi.org/10.3847/2041-8213/ab8016.

McInnes, C.R., 2004. Solar Sailing: Technology, Dynamics and Mission Applications. Springer Science & Business Media. https://doi.org/10.1007/978-1-4471-3992-8.

Mengali, G., Quarta, A.A., 2005. Near-optimal solar-sail orbit-raising from low earth orbit. J. Spacecraft Rock. 42 (5), 954–958. https://doi.org/10.2514/1.14184.

Mikulas Jr, M.M., 1978. Structural efficiency of long lightly loaded truss and isogrid columns for space applications. Tech. Rep. NASA-TM-78687, NASA.

Mikulas Jr, M.M., Bush, H.G., Card, M.F., 1977. Structural stiffness, strength and dynamic characteristics of large tetrahedral space truss structures. Tech. Rep. NASA-TM-X-74001, NASA.

Mikulas, M.M., Collins, T.J., Doggett, W., Dorsey, J., Watson, J., 2006. Truss performance and packaging metrics. AIP Conference Proceedings, vol. 813. American Institute of Physics, pp. 1000–1009. https://doi.org/10.1063/1.2169281.

Milkovich, S.M., Herakovich, C.T., 1984. Temperature dependence of elastic and strength properties of t300/5208 graphite-epoxy. Tech. Rep.

Oberth, H., 1929. Methods of space travel, Munich, Oldenburg 494.

Oderinwale, T., McInnes, C.R., 2022. Enhancing solar energy generation and usage: Orbiting solar reflectors as alternative to energy storage. Appl. Energy 317, 119154. https://doi.org/10.1016/j.apenergy.2022.119154.

Oderinwale, T., McInnes, C.R., 2022. Economic feasibility of alternative technological concepts to harness renewable energy from space. IET Conf. Proc., 130–134 https://doi.org/10.1049/icp.2022.1687.

Pears, A., 1998. Chapter 7: Appliance technologies and scope for emission reduction, Strategic Study of Household Energy and Greenhouse Issues. Australian Greenhouse Office. 61.

Popov, E., Balan, T., 1999. Engineering Mechanics of Solids. Prentice-Hall.

Potter, S., Davis, D., 2009. Orbital reflectors for space solar power demonstration and use in the near term. AIAA SPACE 2009 Conference & Exposition, AIAA, Pasadena, CA. https://doi.org/10.2514/6.2009-6675.

Prater, T., Werkheiser, N., Ledbetter, F., Timucin, D., Wheeler, K., Snyder, M., 2019. 3d printing in zero g technology demonstration mission: complete experimental results and summary of related material modeling efforts. Int. J. Adv. Manuf. Technol. 101 (1), 391–417. https://doi.org/10.1007/s00170-018-2827-7.

Rawer, K., 1982. Short description of solar power satellites. Adv. Space Res. 2 (3), 93. https://doi.org/10.1016/0273-1177(82)90023-0.

Salazar, F., McInnes, C., Winter, O., 2016. Intervening in earth's climate system through space-based solar reflectors. Adv. Space Res. 58 (1), 17–29. https://doi.org/10.1016/j.asr.2016.04.007.

Schaub, H., Junkins, J.L., 2009. Analytical mechanics of space systems. Ame. Inst. Aeronaut. Astronaut. https://doi.org/10.2514/4.105210.

Schwab, A.L., 2002. Quaternions, Finite Rotation and Euler Parameters. Cornell University Notes, Ithaca NY, p. 28.

Smith, F., 1982. Effect on optical astronomy of sunlight reflected from spacecraft. Adv. Space Res. 2 (3), 7–8. https://doi.org/10.1016/0273-1177(82)90003-5.

Stephenson, P.G., Moore, C.M., Terry, M.J., Zubkov, M.V., Bibby, T.S., 2011. Improving photosynthesis for algal biofuels: toward a green revolution. Trends Biotechnol. 29 (12), 615–623. https://doi.org/10.1016/j.tibtech.2011.06.005.

Tress, W., Domanski, K., Carlsen, B., Agarwalla, A., Alharbi, E.A., Graetzel, M., Hagfeldt, A., 2019. Performance of perovskite solar cells under simulated temperature-illumination real-world operating conditions. Nat. Energy 4 (7), 568–574. https://doi.org/10.1038/s41560-019-0400-8.

Trofimov, S.P., Ovchinnikov, M.Y., 2018. Performance scalability of square solar sails. J. Spacecraft Rock. 55 (1), 242–246. https://doi.org/10.2514/1.A33894.

Venugopal, R., Manjunath, H., Anjanpura, V.R., Singh, P.K., 2022. Overview of space based solar power. Mater. Sci. Res. India 19, 58–62. https://doi.org/10.13005/msri/190203.

Viale, A., McInnes, C.R., 2023. Attitude control actuator scaling laws for orbiting solar reflectors. Adv. Space Res. 71 (1), 604–623. https://doi.org/10.1016/j.asr.2022.10.015.

Viale, A., Çelik, O., Oderinwale, T., Sulbhewar, L., Bailet, G., McInnes, C.R., 2022. Towards the commercial development of orbiting reflectors: a technology demonstration roadmap. In: 73rd International Astronautical Congress (IAC 2022), IAF, Paris, France, paper no. IAC-22-C3.2.x70070.

Wertz, J.R., 2012. Spacecraft Attitude Determination and Control, vol. 73. Springer Science & Business Media. https://doi.org/10.1007/978-94-009-9907-7.

Wie, B., Bailey, D., Heiberg, C., 2002. Rapid multitarget acquisition and pointing control of agile spacecraft. J. Guidance Control Dyn. 25 (1), 96–104. https://doi.org/10.2514/2.4854.

Yanoff, M., Duker, J.S., 2008. Ophthalmology, 3rd ed. Elsevier Health Sciences.